Density Matrix Renormalization Group and Quantum Information applied to Quantum Critical Phenomena in One-Dimensional Systems

Philipps Universität Marburg

Dissertation

zur Erlangung des
Doktorgrades der Naturwissenschaften
(Dr. rer. nat.)
dem Fachbereich Physik
der Philipps-Universität Marburg
vorgelegt

von

Leonildo Tincani

aus Scandiano (Italien)

Marburg an der Lahn, April 2008

A mia madre e mio padre.

Zusammenfassung

In der vorliegenden Arbeit werden drei verschiedene Quantenphasenübergänge in quasi-eindimensionalen Systemen mit Hilfe analytischer und numerischer Methoden untersucht.

Im ersten Teil widmen wir uns dem Übergang von einem Band- in einen Mott-Isolator. Solche Übergänge treten in Ladungs-Transfer-Systemen auf, für die das halb gefüllte ionische Hubbardmodell einen Prototypen darstellt. In unserer Untersuchung wird zunächst ein effektives 'Spin-Eins Modell' abgeleitet, das wir dann mit Hilfe der Dichtematrix-Renormierungsgruppe numerisch untersuchen. Insbesondere führen wir eine sorgfältige 'finite-size' Skalenanalyse der Massenlücke, des Ordnungsparameters und der zugehörigen Suszeptibilität durch. Hierbei wird die Existenz zweier quantenkritischer Punkte bestätigt. Die Analyse der kritischen Exponenten zeigt, dass der gefundene Übergang vom Band-Isolator in die spontan dimerisierte Phase zur 2D Ising-Klasse gehört. Der zweite Übergang von der dimerisierten Phase in den Mott-Isolator ist von unendlicher Ordnung.

Gegenstand des zweiten Teils der Arbeit ist der Mott-Metall-Isolator Übergang in einem halb gefüllten Hubbardmodell mit nächstem und übernächstem Nachbarhüpfen. Wir verwenden hierbei die Methode der Bosonisierung sowie die Dichtematrix-Renormierungsgruppe. Mit Hilfe der Bosonisierungsmethode leiten wir einen effektiven Niedrigenergie-Hamiltonoperator ab, der den Mott-Metall-Isolator Übergang beschreibt. Desweiteren werden DMRG Ergebnisse zur Ladungs-und Spin- Verteilung in verschiedenen Bereichen des Phasendiagramms vorgestellt. Die numerischen Resultate stützen das Szenario des effektiven Modells, wonach die Übergänge im Spin- und im Ladungssektor voneinander unabhängig sind.

Abschließend werden im dritten Teil der Arbeit Übergänge zwischen räumlich homogenen und inhomogenen Phasen in niedrigdimensionalen Fermionen- und Spinsystemen untersucht. Bei den inhomogenen Phasen handelt es sich um dimerisierte, trimerisierte und inkommensurable Zustände. In diesem Zusammenhang schlagen wir einen neuen Zugang vor, in dem die Längenabhängigkeit der 'von Neumann Entropie' sowie das zugehörige Fourier-Spektrum ausgewertet werden. Bei endlichen Wellenvektoren weisen Maxima im Spektrum auf ein oszillatorisches Verhalten von Korrelationsfunktionen hin und liefern darüber hinaus wichtige Informationen zu den Eigenschaften des Anregungsspektrums. Insbesondere erlauben sie die Bestimmung von 'weichen' Moden kritischer Modelle.

Abstract

We investigate three different types of quantum phase transition occurring in quasi one-dimensional systems theoretically and numerically.

First, we study the band-insulator to Mott-insulator transition occurring in charge-transfer complexes, for which the half-filled one-dimensional ionic Hubbard model is considered to be the prototype model. The study is carried out by first deriving an effective spin-one model, and then studying the model numerically using the density matrix renormalization group. We perform a careful finite-size scaling analysis of the mass gaps, order-parameters, and relative susceptibility. We confirm the existence of two quantum critical points. Analysis of the critical exponents confirms that the band-insulator-to-spontaneously-dimerized phase transition belong to the 2D Ising class. The spontaneously dimerized phase undergoes a phase transition to the Mott-insulator which is an infinite-order.

Second, we investigate the Mott metal-insulator transition for the half-filled Hubbard model with both nearest-neighbor t and next-nearest-neighbor t' hopping terms. We study the model using the bosonization approach and density matrix renormalization group simulations. An effective low-energy Hamiltonian that describes the insulator-metal transition is derived. We present results of density matrix renormalization group calculations of spin and charge distribution in various sectors of the phase diagram. The numerical results support the picture derived from the effective theory and give evidence for the complete separation of the transitions involving the spin and the charge degrees of freedom.

Finally, we investigate quantum phase transitions phases in low-dimensional fermionic and spin models that go from uniform to spatially inhomogeneous, i.e., dimerized, trimerized, or incommensurate, phases. We propose a new approach based on studying the length dependence of the von Neumann entropy and its corresponding Fourier spectrum for finite segments in the ground state of finite chains. Peaks at a nonzero wave vector are indicators of oscillatory behavior in decaying correlation functions and also provide significant information about certain relevant features of the excitation spectrum; in particular, they can identify the wave vector of soft modes in critical models.

Contents

List of Tables

List of Figures

List of Figures

Introduction

In condensed matter physics, the equations of non-relativistic quantum mechanics describe all phenomena and play the role of a *theory of everything*[1] [1, 2]. To find solutions of the Schrödinger equation for many particles ($N \sim 10^{23}$) is an extremely difficult problem and is the essence of condensed matter theory [3]. The Schrödinger equation has the form of a wave equation

$$i\hbar \frac{\partial}{\partial t}|\Psi\rangle = \mathcal{H}|\Psi\rangle$$

where, for a general condensed matter system,

$$\mathcal{H} = -\sum_{j}^{N_e} \frac{\hbar}{2m}\boldsymbol{\nabla}_j^2 - \sum_{\alpha}^{N_i} \frac{\hbar}{2M_\alpha}\boldsymbol{\nabla}_\alpha^2$$
$$-\sum_{j}^{N_e}\sum_{\alpha}^{N_i} \frac{Z_\alpha e^2}{|\boldsymbol{r}_j - \boldsymbol{R}_\alpha|} + \sum_{j<k}^{N_e} \frac{e^2}{|\boldsymbol{r}_j - \boldsymbol{r}_k|} + \sum_{\alpha<\beta}^{N_i} \frac{Z_\alpha Z_\beta e^2}{|\boldsymbol{R}_\alpha - \boldsymbol{R}_\beta|} \, ,$$

in first quantization. This description is parameterized by the atomic number Z_α, the mass M_α, and the position $\boldsymbol{R}_\alpha$ of nucleus α and the mass m, the charge e, and the position $\boldsymbol{r}_j$ of electron j in a system with N_e electrons and N_i nuclei.

The problem is challenging because there is no analytical or numerical method known that can solve this equation for such a large number of particles. We know that only a small collection of successful recipes work in particular cases. Nevertheless, at certain energy scales, simpler effective theories emerge from the original one, allowing us to explain phenomena such as the nature of metals, semiconductors, superconductors, superfluids, and the quantum Hall effect without solving the full Schrödinger equation.

In solid state physics, the electrons move orders of magnitude faster than the ions, which can be treated as being localized on the vertices of a lattice [4, 5]. As a consequence, the electronic and ionic degrees of freedom can be decoupled, and the Schrödinger equation reduces, to zeroth order, to an electron-electron problem. This approach is called the Born-Oppenheimer approximation or adiabatic

---

[1]Relativistic effects are important in some systems, but can usually be treated as additional interactions in a non-relativistic picture, e.g., the spin-orbit interaction.

approximation [6], and the Hamiltonian can be simplified to

$$\hat{H}_{\mathrm{e}} = \hat{T}_{\mathrm{e}} + \hat{V}_{\mathrm{ee}} + \hat{V}_{\mathrm{ext}} \,,$$

where $\hat{T}_{\mathrm{e}}$ is the kinetic part of the electrons, $\hat{V}_{\mathrm{ee}}$ the electron-electron interaction and $\hat{V}_{\mathrm{ext}}$ is the potential acting on the electrons that is produced by the ions in their equilibrium positions. The motion of ions can be included in the next order as phonons.

Unfortunately, the equations obtained within the Born-Oppenheimer approximation are still quite difficult to solve. More insight into the ground-state properties is provided by the Hohenberg-Kohn theorem [7], which is the key to understanding the electronic structure of most materials. It states that the external potential acting on electrons is uniquely determined by the electronic density $\tilde{\rho}(\mathbf{r})$. A corollary of the theorem says that the ground state wave function that would be obtained by solving the full Schrödinger equation is also uniquely determined by the electron density. In addition, the theorem states that the ground-state energy E of a many-electron system is a functional of the electron density, i.e.,

$$E_v[\tilde{\rho}] = F[\tilde{\rho}] + \int \tilde{\rho}(\mathbf{r}) v_{\mathrm{ext}}(\mathbf{r}) d\mathbf{r} \,,$$

where $F[\tilde{\rho}]$ is unknown functional and $E_v[\tilde{\rho}]$ is minimized by the ground state. In principle, this method is exact, but in practice, the correct functional is unknown [8]. Today, density-functional theory (DFT) with the local density approximation (LDA) successfully describes the overall electronic properties of most solids and molecules [9]. However, no known functional can correctly describe low-dimensional systems in which the electrons are strongly correlated; for such systems the local density approximation fails [10].

Strong correlation effects are particularly pronounced in low dimensional or strongly anisotropic materials. The constraint on the motion of electrons and the reduction of screening lead to a larger effective electron-electron interaction and to a larger influence of the quantum fluctuations [11–13]. Such materials manifest collective quantum phenomena which are interesting theoretically [14–16], experimentally [17], and technologically [18]. One important aspect of the effects of strong correlations is that a small change in a relevant parameter can induce large changes in the properties of a material. Examples include the rich phase diagrams of a number of organic materials [19], such as the Bechgaard salts [20], polyacetylene [21], and the chloranil compounds [22]. Another example is the phenomenon of colossal magnetoresistance (CMR) [23,24]. In certain manganites, a small change in the applied magnetic field can induce an enormous change in the resistance. While this phenomenon is not yet well understood theoretically, it could potentially have a large impact on hard disk storage technology. Another important

class of strongly correlated materials is that of the high-temperature superconducting cuprates [15, 25, 26]. Small changes in doping induce a transition from an antiferromagnetic insulator to a high-temperature superconductor. Despite many years of work, the mechanism is not yet completely understood theoretically [27].

Recently, properties of strongly correlated systems have been used engineer quantum devices. For example, spintronic devices use strong interaction effects to manipulate the spin degrees of freedom of electrons [28]. In order to construct a quantum computer [29], it is essential to control the necessarily strong interaction between qubits [30].

Since first-principles methods either involve such rough approximations that strongly correlation effects cannot adequately be described or lead to problems that cannot be solved, it is useful to formulate simpler effective models that contain the essential physics [10, 31–37]. The prototypical model for strongly correlated itinerant electrons is the Hubbard model, which describes electrons hopping on a lattice under the influence of a localized Coulomb interaction. The Hubbard Hamiltonian is

$$\hat{H} = -\sum_{i,j;\sigma} t_{i,j} \hat{c}_{i,\sigma} \hat{c}_{j,\sigma}^{\dagger} + \frac{U}{2} \sum_{i;\sigma} \hat{n}_{i,\sigma} \hat{n}_{i,\overline{\sigma}} \,,$$

where $\hat{c}_{\sigma}$ and $\hat{c}_{\sigma}^{\dagger}$ operators destroy and create an electron of spin σ, respectively, and $\hat{n}$ is the particle number operator. The model can be extended by adding a number of different interactions, such as longer-range Coulomb terms, modified hopping terms, spin interactions, or an alternating potential. Much of the rest of this thesis is concerned with such extended Hubbard models in one dimension. The physics of the Hubbard model includes concepts such as the Tomonaga-Luttinger liquid (in one dimension) [38–40], the Mott metal-insulator transition [41], antiferromagnetism, ferromagnetism, and superconductivity [32, 42].

In many cases, it is useful to treat the spin degrees of freedom as being localized. This can be done using a quantum spin model. The prototypical model is the Heisenberg model with Hamiltonian [43]

$$\hat{H} = \sum_{i,j} J_{i,j} \hat{S}_i \cdot \hat{S}_j \,,$$

where $\hat{S}_i$ is the spin operator on lattice site i. In general the local spin can take on any value that is a multiple of a half integer. In the spin-one-half case, the Heisenberg model is the strong-coupling limit of the Hubbard model at half filling. It is also useful to consider higher values of the spin, in particular, spin one. This can occur either when two or more electrons are localized on a site or, as we shall see in chapter 3, when three local degrees of freedom are incorporated in an effective model. Anisotropy or additional exchange interaction, such as a biquadratic exchange, can also be introduced to generalize the Heisenberg model. The physics

of the antiferromagnetic Heisenberg model, which will primarily be considered in this thesis, has been studied extensively and a number of results are known [42,44]. In two or more dimensions, the behavior on simple unfrustrated lattices is that of a renormalized classical antiferromagnet. More interesting behavior occurs on non-Bravais lattices and on frustrated lattices. In one dimension, the Haldane picture describes completely the possible behavior of spin chains. Half-integer spin chains are gapless and critical, whereas integer spin chains have a gap to spin excitations.

In this thesis, we address some interesting current issues in one-dimensional quantum systems. One-dimensional systems are particularly well-suited to investigate some fundamental aspects of interacting quantum systems for two reasons [10]. First, since quantum fluctuations are strongest in one dimension, non-classical phenomena such as quantum phase transitions, critical phases, and collective quantum effects are numerous. Second, there are a number of techniques, both analytical and numerical, which make it possible to study these systems in an accurate and well-controlled way. Analytic techniques include exact solutions such as the Bethe ansatz and well-controlled field theoretical techniques such as the renormalization group, bosonization, and conformal field theory [45]. Numerical techniques include exact diagonalization, quantum Monte Carlo, and the density matrix renormalization group (DMRG). Here we make use of results from these field-theoretical techniques, and carry out numerical calculations with the DMRG [46, 47], currently the most effective numerical technique to calculate the ground-state properties of one-dimensional interacting quantum systems.

The issues that we will study can be grouped into two main topics. The first topic is the characterization of quantum phase transitions, i.e., phase transitions occurring at zero temperature as the parameters of a system are changed. These transitions have been of interest recently because their experimental signatures have become more accessible and because the theoretical understanding has increased [48]. The second, related topic is the relationship between the properties of ground states, especially those with strong quantum effects, and the properties of quantum phase transitions and quantum information. While the connection between quantum mechanical entanglement and quantum entropy has been known for a long time, the relationship between the properties of strongly correlated states and quantum information has only recently been elucidated [49].

In particular, we study three particular types of quantum phase transition: the band insulator–Mott insulator transition, the Mott metal-insulator transition, and homogeneous-inhomogeneous phase transitions. The ionic Hubbard model is the simplest fundamental model for the band insulator–Mott insulator transition because it contains two competing terms, the alternating ionic potential, which induces a band insulator, and the local Coulomb repulsion, which induces a Mott insulator. In order to study the detailed behavior of the transition, we derive

an effective strong-coupling Hamiltonian, which contains the essential physics of the transition. We analyze the critical behavior of this effective model using the DMRG in conjunction with extensive finite-size scaling. We are able to verify the presence of two phase transitions and a spontaneously dimerized phase between the band- and Mott-insulating phases and can extract more detailed information on the critical exponents than previously possible.

A purely interaction-induced Mott metal-insulator transition occurs in the Hubbard chain with next-nearest-neighbor hopping. We relate the Mott transition to the commensurate-incommensurate transition associated with the change from a two-point to a four-point Fermi surface. We confirm a theoretical picture based on bosonization by carrying out detailed DMRG calculations of the relevant charge and spin gaps, the momentum-space structure of the charge and spin oscillations, and the momentum distribution. We thus obtain a full and intuitive picture of origin of the phase diagram.

Homogeneous-inhomogeneous phases transitions occur in various models. We study such transitions in three different models: the frustrated spin-1/2 Heisenberg chain, the bilinear-biquadratic spin-one chain, and the Hubbard chain with next-nearest-neighbor hopping also treated previously. In this case, we make use of quantum information entropies, in particular, the block, single-site and two-site entropies, to characterize the momentum-space structure of the phases. We show that these quantities contain the full information needed to classify the various phases and to extract universal parameters characterizing critical phases.

Structure of the Thesis

The thesis is structured in two parts. The first part, contained in chapters 1 and 2, focuses on the methods and tools used. The second part, consisting of chapters 3, 4 and 5, describes our results.

In chapter 1, we introduce the analytical methods to study quantum critical phenomena in one dimension. The basic concepts of the Luttinger liquid, spin-charge separation, and central charge are discussed. In chapter 2, we describe the density matrix renormalization group method, which is our main numerical tool, and its connection with quantum information.

In chapter 3, we derive an effective model for the band-to-Mott insulator transition that correctly describes the physics of the problem, allowing us to address some outstanding questions. We supplement the analytical derivation with an extensive numerical investigation using the DMRG and finite-size scaling aimed to characterize the transition. In chapter 4, we study the Mott insulator-metal transition occurring into the $t-t'$ Hubbard model with nearest-, t, and next-nearest-neighbor, t', hopping terms. We propose a mechanism, based on bosonization and including the commensurate-incommensurate transition, to explain the full phase diagram.

We then check our conjecture using density matrix renormalization group calculations. In chapter 5, we use the von Neumann entropy to characterize different phases and critical points. We test our method on the well understood spin-one-half Heisenberg model and on the spin-one bilinear-biquadratic model, and, finally, we apply it the $t - t'$ Hubbard model of chapter 4.

When appropriate, chapters conclude with a brief discussion or summary. In the conclusion, we summarize the work and give an outlook.

Publications

Parts of this thesis have been already published or have been prepared for publication. Since other people were also involved in this process, I have taken care to point out my contributions to each project at end of each chapter. In order, the chapters related to each publication are:

Chapter 3

> *Effective model for the band-insulator-to-Mott-insulator transition in the ionic Hubbard model*
> L. Tincani, R. M. Noack and D. Baeriswyl,
> *in preparation.*

Chapter 4

> *Phases and phase transitions in the half-filled $t - t'$ Hubbard chain*
> G. I. Japaridze, R. M. Noack, D. Baeriswyl and L. Tincani,
> Physical Review B **76**, 115118 (2007).

Chapter 5

> *Entropic analysis of quantum phase transitions from uniform to spatially inhomogeneous phases*
> Ö. Legeza, J. Sólyom, L. Tincani and R. M. Noack,
> Physical Review Letters **99**, 087203 (2007).

> *Applications of Quantum Information in the Density-Matrix Renormalization Group*
> Ö. Legeza, R. M. Noack, J. Sólyom and L. Tincani,
> in *Computational Many-Particle Physics*, Lecture Notes in Physics, Vol. 739, Fehske, H.; Schneider, R.; Weie, A. editors, Springer (2008).

1 Analytical Approach to Quantum Phase Transitions

1.1 Theory of critical phenomena

The first theory of critical phenomena was proposed by Landau [50]. The Landau theory unified all mean-field theories in a general framework and introduced the concept of the order parameter. The order parameter m is a thermodynamic quantity, which can be a scalar, a vector, or a tensor, that vanishes in one phase and takes on a nonzero value on another one. The basis of the Landau theory is that the effective free energy is an analytic function of the order parameter, consistent with the symmetry of the problem [51–54]. Therefore, the value of the order parameter is the one that minimizes the free energy and its vanishing delineates the phase transition. The character of the transition, first or second order, the exponents of the transition, and the explanation of the relation between the soft modes and the fluctuations of the order parameter, are possible within the theory. However, the exact solution of Onsager [55] and of the two dimensional Ising model [56, 57] showed that the Landau theory is not quantitatively correct because it does not correctly treat the fluctuations of the order parameter near criticality. In fact, according to the Ginzburg criterion, which states that there must exist a dimensionality d_c such that for $d > d_c$ fluctuations are unimportant, the Landau theory is valid only for systems of dimension larger than d_c [52].

In the 1960's, critical phenomena were reinterpreted in terms of the new concepts of scaling and universality [58–60]. The discovery of the scaling relations, called scaling laws, that relate the different critical exponents and explain the observation of the universal collapse of data, has become central in the classification of the critical phenomena. However, a more complete understanding of the problem was achieved only after scaling ideas were expressed in terms of the renormalization group (RG) by Wilson [61]. First, one generalizes the Landau functional by expressing the partition function $Z = e^{-F/T}$ as a functional integral

$$Z = e^{-F/T} = \int \mathcal{D}[\phi] e^{-S[\phi]},$$

where $S[\phi]$ is the action of a field ϕ that fluctuates around the average $\langle \phi \rangle = m$.

The next step is to study the Landau-Ginzburg-Wilson functional using the renormalization group method [52, 53, 62, 63]. In the lowest order (saddle point) approximation one recovers Landau theory. The central concept in the Wilson RG approach to the critical point is the divergence of the correlation length ξ, which is assumed to be the only important length scale and which dominates the long wavelength physics. Therefore, all the smaller length scales can be integrated out. The most important result is a complete and consistent derivation of the critical exponents and scaling laws in term of the renormalization group transformation. Concepts originating from the RG, such as fixed points of the RG flow and relevant, marginal, and irrelevant parameters, now belong to the standard methods of investigating critical phenomena [52, 53, 63, 64].

In addition to the diverging correlation length scale ξ, there is also a diverging time scale τ [65]. The two scales are related by the dynamical exponent z as $\tau \sim \xi^z$. This gives rise to critical slowing down: a system relaxes towards equilibrium very slowly near a critical point. In classical systems, the dynamic and static part of the partition function can be decoupled. In the quantum case, the kinetic part and the potential part of the Hamiltonian do not commute. Thus, the dynamic and static contributions to the partition function cannot be decoupled and z must be taken into account in the scaling of the free energy [48, 66].

The Landau-Ginzburg-Wilson approach is an extremely powerful way of describing and classifying any critical phenomenon [67]. Nevertheless, there are some quantum phase transitions that cannot be described by considering only the long wavelength fluctuations of a local order parameter. Some mechanisms that can invalidate the Landau-Ginzburg-Wilson approach are generic scale invariance [68], deconfined quantum criticality [69], heavy fermion quantum criticality [70], and impurity quantum phase transitions [71].

1.1.1 Finite-size scaling

Finite-size effects in critical phenomena have been investigated extensively in theoretical studies [53, 72] and have recently begun to be studied experimentally in thin films [73–78]. Finite-size scaling analysis is important in numerical work where the linear dimension of the system has a finite value L.

The inverse of the system size acts as an additional parameter that moves the system away from the critical point. Indeed, finite-size systems can not be critical and they have to be gapped [79]. However, renormalization group theory applied to such a system shows that the RG equations are not modified, restricting the system to a finite one [64]. The difference appears in the solution of the equations because correlation functions depend now on the system size [53, 63]. Thus, knowing this dependence, critical parameters of a system at the thermodynamic limit can be obtained by the system-size scaling analysis of the corresponding thermodynamic

quantities in finite-size systems [72].

When we study finite systems, there are two aspects to consider: the geometry of the system and the boundary conditions [53, 72]. There are three particular interesting geometries. First, a completely finite system of volume V in d dimensions. Second, a d-dimensional layer system of infinite extended dimension in $d-1$ dimensions, but of finite thickness in the remaining one. Third, a system infinite in one dimension, but finite in the other ones. Though they do not differ in one-dimensional systems, in systems of dimensionality $d > 2$, different geometries can give rise to the crossover scaling effect [72]: the exponents first take on one value, than cross over to another when the system size reaches a particular value. Whatever the geometry, restricting the domain of a system to a finite region involves the introduction of boundaries and the imposition of boundary conditions. Different boundary conditions lead to different surface critical behaviors. The system can be separated into bulk and surface components, each with different critical exponents. In the thermodynamic limit, the critical character of the bulk is dominant. In addition, for a system away from criticality with open boundary conditions, thermodynamic arguments suggest that the free energy contribution to the total free energy is proportional to the surface volume. Such a contribution would vanish identically for periodic or anti-periodic boundary conditions [53, 72].

Now we formulate finite-size scaling and derive its consequences for transitions obtained varying some non-thermal parameter ε. In a quantum system in the neighborhood of a critical point, there are only two scales that matter, the correlation length in space ξ, and the analogous time τ_c scale.

These two quantities diverge close to a critical point ε_c

$$\xi \sim |\varepsilon - \varepsilon_c|^{-\nu}, \qquad \tau_c \sim |\varepsilon - \varepsilon_c|^{-\nu z}, \qquad (1.1)$$

where ν is the correlation length critical exponent and z is the dynamical critical exponent [65]. As a consequence, at the critical point all observables diverge as power laws. For example, the susceptibility diverges as

$$\chi \sim |\varepsilon - \varepsilon_c|^{-\gamma} \sim \xi^{\gamma/\nu}. \qquad (1.2)$$

All critical exponents are related by the simple scaling relations,

$$\alpha + 2\beta + \gamma = 2, \qquad 2 - \alpha = \nu d, \qquad (1.3)$$

where α and β are the specific heat and order parameter exponents respectively for a system of dimensionality d. The set of their values defines the universality class of the transition [67].

The behavior of a critical system at zero temperature is characterized by the absence of an energy gap between the ground state and first excited state [48].

This gap corresponds to the mass gap [80]

$$\Delta_m \sim 1/\xi^z \,, \tag{1.4}$$

where the smallest value of the energy gap $E_1 - E_0$ is Δ_m.

For a finite system of size L, the correlation length cannot be larger than the size of the system. Thus we expect that, at the critical point,

$$\xi \sim L \tag{1.5}$$

as $L \to \infty$ or, equivalently, massive soft modes appear and scale as $\Delta_m \sim L^{-z}$. In other words, as the critical point is approached, the effective theory will become closer and closer to that of free massless particles with a spectrum $\Delta_m \sim k^z$ for $k \to 0$. Since the lattice is discrete, the smallest nonzero momentum must be $2\pi/L$, leading to the $1/L^z$ behavior of the gap [81]. We define the pseudo-critical point $\varepsilon^*(L)$ by the condition $\xi[\varepsilon^*(L)] \sim L$.

Due to the scaling hypothesis, all the other quantities have definite scaling behavior with system size: the susceptibility $\chi(\varepsilon_c, L) \sim L^{\gamma/\nu}$, the order parameter, $D(\varepsilon_c, L) \sim L^{-\beta/\nu}$, and the specific heat, $c(\varepsilon_c, L) \sim L^{\alpha/\nu}$. In addition, the position of the pseudo-critical point relative to the true critical point scales as $L^{-1/\nu}$, allowing us to extract the correct critical exponents from the scaling behavior of pseudo-critical points [72].

Correlation functions can be calculated as well and can be used to extract the exponent η, i.e.,

$$G(\varepsilon_c, r \to \infty) \sim |r|^{-(d+z)+2-\eta}.$$

However, one must be careful in the choice of which specific correlation function is measured because it is difficult, *a priori*, to distinguish which one is dominant in the thermodynamic limit. In addition, sufficiently large systems are necessary to extract information about the $r \to \infty$ behavior [82, 83].

The above scaling analysis is applicable to second-order phase transitions, but in nature a system can also undergo a transition that scales faster than any power law, i.e., with an infinite exponent. Therefore an extension of finite-size scaling to these transitions is necessary, but is not trivial [84, 85]. One reason is that the theory contains irrelevant variables which are difficult to deal with, leading to logarithmic terms [53]. In addition, such transitions typically involve topological order [86], i.e., no local order parameter can be used to discriminate between the phases [87–90]. Technically, the two phases can be distinguished only using their global properties [66].

The prototypical universality class for infinite-order transitions is that of the 2D XY model, which is characterized by the Kosterlitz-Thouless (KT) critical behavior [67, 91–93]. According to the KT scenario, which is obtained using perturbation

theory, the free energy has an essential singularity at ε_c, and the correlation length diverges exponentially as

$$\xi(t \to 0^+) \sim e^{b/t^\sigma} ,$$

where $t = \varepsilon/\varepsilon_c - 1$, $\sigma = 1/2$, and b is a positive non-universal constant. This implies that the mass gap closes very quickly,

$$\Delta_m \sim 1/\xi \sim e^{-b/t^\sigma} , \tag{1.6}$$

and that correlation functions decay exponentially

$$G(t \to 0^+, r) \sim e^{-r/\xi}$$

very close to the critical point. At the critical point, the asymptotic behavior of the two-point correlation function for $r \to \infty$ is

$$G(\varepsilon_c, r) \sim \frac{(\ln r)^{2\theta}}{r^{\eta_c}} ,$$

where $\eta_c = 1/4$ and $\theta = 1/16$, and the exponent θ takes into account the logarithmic corrections. An interesting approach that suppresses the logarithmic corrections is achieved by a conformal rescaling of the correlation functions [94].

Assuming that the system is finite, we can still argue that the only relevant spatial length scale is $\xi(L)$, rounding off the transition at $\xi(\varepsilon_c) \sim L$. Therefore, the growth of the susceptibility is given by

$$\chi(\varepsilon, L) \sim L^{2-\eta_c} (\ln L)^{-2\theta} ,$$

where the logarithmic correction is explicitly included. Beyond the critical point, the phase is completely critical, and one expects the scaling

$$\chi(\varepsilon > \varepsilon_c, L) \sim L^{2-\eta(\varepsilon)}$$

for $L \to \infty$. As a consequence, the susceptibility does not exhibit a maximum in the vicinity of the critical point, so that it cannot be used to extract the critical coupling. The singular behavior of the specific heat is also known; it exhibits a weak singularity [92] $c \sim \xi^{-2}$. Such behavior is very difficult to observe as it behaves regularly in ε_c.

Therefore, a regular behavior of the ground state energy as function of ε, associated with a divergent correlation length or susceptibility as L increases, is a good indicator that there is a KT transition.

In two dimensional classical systems or in $(1+1)$-dimensional quantum systems, a number of nontrivial models can be solved exactly [40, 95–97], and, moreover, conformal field theory gives exact predictions for the critical exponents and critical behavior [53, 98]. In fact, the critical phases can be classified on the basis of the central charge. For instance, the 2D Ising universality class and the 2D XY universality class correspond to CFTs with central charges $c = 1/2$ and $c = 1$, respectively [99, 100].

1.2 The Luttinger liquid and bosonization

The properties of one-dimensional systems of electrons moving on a lattice are governed by the quantum nature of the particles, the interaction between particles, and the coupling with an external potential [39, 80, 101]. Quantum systems in three dimensions are successfully described by the Landau Fermi-liquid theory [34, 97, 102–107]. However, in one dimension, the (perturbative) renormalization group [108, 109] indicates different behavior [34, 38] that of the Luttinger liquid [110–115]. The Fermi surface consists of two discrete points $(\pm k_F)$, the quasiparticle weight vanishes, there is no well-defined quasiparticle (peak), and spin-charge separation occurs [108, 116–119]. The perturbation theory approach can be extended to stronger coupling by going to higher order in perturbation theory [120], but it fails in the strong-coupling limit. The Luttinger liquid picture, in contrast to its weak-coupling basis [108, 121], sometimes survives in the strong-coupling limit, as described within the bosonization approach [111, 121–124]. In fact, in one dimension the Pauli exclusion principle reduces to a boundary condition. From this it follows that, for any interacting fermion problem, there is a corresponding interacting boson problem. Therefore, we utilize the possibility of mapping a strong-coupling problem to a weak-coupling one with different statistics [125–128]. The new problem can then be treated by the (perturbative) renormalization group [129, 130] approach, or by the more powerful functional renormalization group method [131, 132]. H. J. Schultz's application of the bosonization method to the Hubbard model provides a detailed description of the crossover between weak and strong interaction as well as of the metal-insulator transition at half filling [133, 134]. An important result achieved using the bosonization approach is to show that the exponents of the correlation functions and the weight of the Drude peak obtained for the Hubbard model, close to half filling, are generic features of any Luttinger liquid [135].

1.2.1 Interacting electrons in one dimension

The starting point is the non-interacting Hamiltonian

$$\hat{H}_0 = \sum_{k,\sigma} \varepsilon(k)\hat{c}^\dagger_{k,\sigma}\hat{c}_{k,\sigma} \,,$$

where $\hat{c}^\dagger_{k,\sigma}(\hat{c}_{k,\sigma})$ is the creation(annihilation) operator for an electron with momentum k and spin σ [109]. The kinetic energy of an electron with respect to the Fermi energy is given by the dispersion $\varepsilon(k)$. The effective low-energy theory is defined in terms of creation and annihilation operators linearizing the energy dispersion

in the vicinity of the Fermi points

$$\hat{H}_0 = \sum_{k,\sigma} \left[v_F \left(k - k_F \right) \hat{c}^{L}_{k,\sigma}{}^{\dagger} \hat{c}^{L}_{k,\sigma} + v_F \left(-k - k_F \right) \hat{c}^{R}_{k,\sigma}{}^{\dagger} \hat{c}^{R}_{k,\sigma} \right] ,$$

where $\hat{c}^L(\hat{c}^{L\,\dagger})$ and $\hat{c}^R(\hat{c}^{R\,\dagger})$ denote the electron annihilation(creation) operators belonging to the left and right Fermi points, respectively. The Fermi velocity is given by $v_F = \partial(\varepsilon_k/\partial k)$, calculated at the Fermi points.

The general two-body interaction for a translationally invariant fermion system can be written as

$$\hat{H}_{\text{int}} = \frac{1}{2} \sum_{\sigma\sigma'} \sum_{k,k',q} \Gamma_{\sigma\sigma'}(q) \hat{c}^{\dagger}_{k+q\ \sigma} \hat{c}^{\dagger}_{k'-q\ \sigma'} \hat{c}_{k\sigma} \hat{c}_{k'\sigma'} .$$

In the low-energy limit, the interaction can be classified into the four different types shown in Fig.1.1.
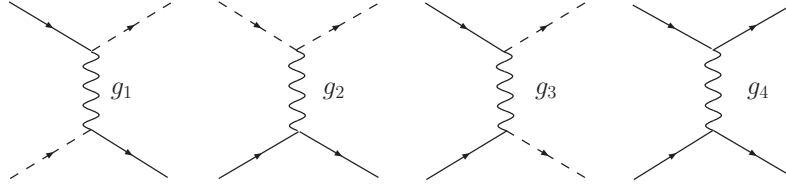
Figure 1.1: The four low-energy scattering process for right-moving (continuous line) and left-moving (dashed lines) electrons in one dimension. The coupling constants are g_1 for backward scattering, g_2 for forward dispersion scattering, g_3 for umklapp scattering (g_3 processes are possible only at half filling) and g_4 for forward scattering.

The scattering process with coupling constant g_1 corresponds to backward scattering of the electrons, with momentum transfer $q = 2k_F$. The process with coupling g_2 and g_4 are forward scattering terms, and are associated with small momentum transfer q. In the g_2 process, the left and right branches are connected, while they are decoupled in the g_4 processes. The umklapp process g_3 contribution occurs only at half filling because of the conservation of crystal momentum. The study of the evolution of the g coupling constants under the (perturbative) renormalization group and the corresponding behavior of the response functions is termed the g-ology technique [109, 118, 119, 136–138].

Linearization of the spectrum. We can generalize to all cases where the linearization of the spectrum in the neighborhood of the Fermi points is reasonable for a momentum cut-off Λ. Thus the effective Hamiltonian is then

$$\hat{H}_F = \sum_{k=k_F-\Lambda}^{k_F+\Lambda} \varepsilon(k)\hat{c}_k^\dagger \hat{c}_k + \sum_{k=-k_F-\Lambda}^{-k_F+\Lambda} \varepsilon(k)\hat{c}_k^\dagger \hat{c}_k \,,$$

and the energy dispersion can be expanded as

$$\varepsilon(k)_{\mathrm{R,L}} = \varepsilon(\pm k_F) + (k \mp k_F) \left.\frac{\partial \varepsilon_k}{\partial k}\right|_{k=\pm k_F} + O\left[(k \mp k_F)^2\right] \quad \text{for} \quad k \approx \pm k_F \,.$$

We work at zero temperature and can thus take $\varepsilon(\pm k_F) = 0$. In addition, we define the Fermi velocity as $v_F = \pm\, \partial \varepsilon_k/\partial k|_{k=\pm k_F}$ and separate the operators into left and right movers

$$\hat{c}_k^R = \hat{c}_{k_F+k} \qquad \hat{c}_k^L = \hat{c}_{-k_F+k} \,.$$

The effective Hamiltonian then becomes

$$H = \sum_{k=-\Lambda}^{\Lambda} v_F k \left(\hat{c}_k^{R\dagger}\hat{c}_k^R - \hat{c}_k^{L\dagger}\hat{c}_k^L \right) \,,$$

where v_F is the only remaining physical parameter and the energy cut-off is fixed by $v_F\Lambda$. One introduces slowly varying fields $\psi_L(x)$ and $\psi_R(x)$ for the left and right movers, so that

$$\psi(x) = \psi_R(x)e^{ik_F x} + \psi_L(x)e^{-ik_F x} \,.$$

In the continuum, the chain has length $\ell = aN$, the Fourier transform of the left and right fields are

$$\hat{c}_k^{L/R} = \frac{1}{\sqrt{\ell}} \int_0^\ell e^{-ikx}\psi_{L/R}(x) \,.$$

Bosonic operators. We now introduce the Fourier-transformed particle-density operator for the right and left movers

$$\hat{\rho}_q^\alpha = \sum_k \hat{c}_{k+q}^{\alpha\dagger}\hat{c}_k^\alpha \,,$$

where the α index can indicate either left (L) or right (R). Thus, the Hamiltonian can be written in a simplified form in terms of these operators. In fact, the density operators $\hat{\rho}^\alpha$ are bosonic operators, i.e.,

$$\left[\hat{\rho}_{-q}^\alpha,\, \hat{\rho}_{q'}^{\alpha'}\right] = \delta_{\alpha\alpha'}\delta_{qq'}\frac{\mathrm{sgn}\,(\alpha)\,Lq}{2\pi} \,.$$

where $\text{sgn}(R) = +1$ and $\text{sgn}(L) = -1$. Their commutator with the noninteracting Hamiltonian is

$$\left[\hat{H}_0,\, \hat{\rho}_q^\alpha\right] = \text{sgn}(\alpha)\, v_F q \hat{\rho}^\alpha(q)\,.$$

Thus, the bosonic algebra is complete. Defining the harmonic-oscillator-type raising operator

$$\hat{b}_k^{\alpha\dagger} = i\sqrt{\frac{2\pi}{kN}}\hat{\rho}_k^\alpha\,,$$

the Hamiltonian can be rewritten

$$\hat{H}_0 = v_F \sum_{k>0} \left(\hat{b}_k^{R\dagger}\hat{b}_k^R + \hat{b}_k^{L\dagger}\hat{b}_k^L\right) + \frac{\pi v_F}{N}\left(n_R^2 + n_L^2\right)\,.$$

This is the original Hamiltonian rewritten in terms of bosonic operators.

Left- and right-moving fermion densities. Defining the real-space fermion density as $\hat{\rho}^\alpha(x) = \psi_\alpha^\dagger(x)\psi_\alpha(x)$ gives rise to divergences [110, 111]. To overcome this, we consider instead its normal ordering [39, 139]

$$:\hat{\rho}^\alpha(x) := \psi_\alpha^\dagger(x)\psi_\alpha(x) - \langle \rho^\alpha(x)\rangle\,.$$

After some calculation, the right moving term becomes

$$\hat{\rho}_k^R = \int_0^\ell dx\, e^{ikx} :\hat{\rho}^R(x): = \sum_{k'} :\left(\hat{c}_{k'+k}^R\right)^\dagger \hat{c}_{k'}^R := \begin{cases} -i\sqrt{\frac{kN}{2\pi}}\hat{b}_k^{R\dagger} & \text{for} \quad k > 0 \\ n_R & \text{for} \quad k = 0 \\ +i\sqrt{\frac{kN}{2\pi}}\hat{b}_k^R & \text{for} \quad k < 0\,. \end{cases}$$

Performing the Fourier transformation of the preceding equation, we obtain the expression for the normal-ordered right-moving density

$$\begin{aligned} :\hat{\rho}^R(x): \quad &= \quad \frac{1}{\ell}\sum_{k>0}\sqrt{\frac{kN}{2\pi}}\left[i\hat{b}_k^R e^{ikx} - i\left(\hat{b}_k^R\right)^\dagger e^{-ikx}\right] + \frac{n_R}{\ell} \\ &= \quad \frac{1}{\ell}\sum_{n=1}^\infty \sqrt{n}\left[i\hat{b}_n^R e^{i\frac{2\pi}{n}x} - i\left(\hat{b}_n^R\right)^\dagger e^{-i\frac{2\pi}{n}x}\right] + \frac{n_R}{\ell}\,, \end{aligned}$$

where we set $k = 2\pi n/N$. Similarly, the expression for the left moving density is

$$\begin{aligned} :\hat{\rho}^L(x): \quad &= \quad \frac{1}{\ell}\sum_{k>0}\sqrt{\frac{kN}{2\pi}}\left[i\left(\hat{b}_k^L\right)^\dagger e^{ikx} - i\hat{b}_k^L e^{-ikx}\right] + \frac{n_L}{\ell} \\ &= \quad \frac{1}{\ell}\sum_{n=1}^\infty \sqrt{n}\left[i\left(\hat{b}_n^L\right)^\dagger e^{i\frac{2\pi}{n}x} - i\hat{b}_n^L e^{-i\frac{2\pi}{n}x}\right] + \frac{n_L}{\ell}\,. \end{aligned} \quad (1.7)$$

Boson field operator. In order to express our Hamiltonian as the standard bosonic field theory, we define the bosonic operators

$$\phi_R(x) = \phi_0^R + \Pi_R \frac{x}{\ell} + \sum_{n=1}^{\infty} \frac{1}{\sqrt{4\pi n}} \left[e^{i\frac{2\pi}{n}x} \hat{b}_n^R + e^{-i\frac{2\pi}{n}x} \left(\hat{b}^R\right)_n^\dagger \right]$$

$$\phi_L(x) = \phi_0^L + \Pi_L \frac{x}{\ell} + \sum_{n=1}^{\infty} \frac{1}{\sqrt{4\pi n}} \left[e^{-i\frac{2\pi}{n}x} \left(\hat{b}^L\right)_n^\dagger + e^{i\frac{2\pi}{n}x} \hat{b}_n^{L\dagger} \right], \qquad (1.8)$$

where, for period boundary conditions, $\Pi_R = \sqrt{\pi} n_R$ and $\Pi_L = \sqrt{\pi} n_L$ represent the conjugate momentum operator of ϕ_R and ϕ_L, respectively. Using these equations, we can directly write the fermion densities as spatial derivatives of the new boson fields

$$: \hat{\rho}^R(x) : \;\; = \;\; \frac{1}{\sqrt{\pi}} \partial_x \phi_R(x)$$

$$: \hat{\rho}^L(x) : \;\; = \;\; \frac{1}{\sqrt{\pi}} \partial_x \phi_L(x) \,,$$

and the Hamiltonian maps to

$$\hat{H} = v_F \int_0^\ell dx \left\{ [\partial_x \phi_R(x)]^2 + [\partial_x \phi_L(x)]^2 \right\} \,.$$

which is a massless bosonic field theory. Thus, we have succeeded in mapping the free fermionic theory to a massless bosonic field theory.

Fermion field. In order to calculate the correlation functions, we need to introduce well-defined fermion operators, expressed in terms of the bosonic fields [123]. The relations

$$\psi_R(x) \propto \exp\left[i\sqrt{4\pi}\phi_R(x)\right], \quad \psi_L(x) \propto \exp\left[-i\sqrt{4\pi}\phi_L(x)\right] \qquad (1.9)$$

satisfy the anti-commutation relations between fermion fields and the commutation relation with the fermion densities [124, 139]. Using these expressions for the fermionic fields, we can express order-parameter operators as well as their correlation functions and spectral functions in the bosonic language [39, 124].

Correlation functions. Within the linearized approximation, the important correlations are $\langle \psi_\alpha \psi_\alpha \rangle$; the left and right movers are uncorrelated, i.e., $\langle \psi_R \psi_L \rangle = 0$. The correlations in real space are given by

$$\langle \psi^\dagger(x)\psi(y) \rangle = \frac{\sin k_F (x-y)}{N \sin \frac{\pi}{2} (x-y)} \,,$$

as expected for a free fermion system.

Spin-charge separation. In order to explore spin-charge separation, we must explicitly differentiate between the two spin species $\sigma = \uparrow, \downarrow$. The spin-dependent fermion densities are

$$: \hat{\rho}^\sigma_{R/L} := \frac{1}{\sqrt{\pi}} \partial_x \phi^\sigma_{R/L}(x) \qquad \sigma = \uparrow, \downarrow \,,$$

and the natural variables of the problem are the total charge density

$$: \hat{\rho}^c_{R/L} := \, : \hat{\rho}^\uparrow_{R/L} : + \, : \hat{\rho}^\downarrow_{R/L} :$$

and the total spin density

$$: \hat{\rho}^s_{R/L} := \, : \hat{\rho}^\uparrow_{R/L} : - \, : \hat{\rho}^\downarrow_{R/L} : \,.$$

Therefore, we can define bosonic fields that correspond to the charge and spin degrees of freedom:

$$\phi^c_{R/L} = \frac{1}{\sqrt{2}} \left[\phi^\uparrow_{R/L}(x) + \phi^\downarrow_{R/L}(x) \right] \,, \qquad \phi^s_{R/L} = \frac{1}{\sqrt{2}} \left[\phi^\uparrow_{R/L}(x) - \phi^\downarrow_{R/L}(x) \right] \,.$$

This definition leads to expressions for the fermion fields that can be factorized into charge and spin parts. However, due to the symmetries of the noninteracting case, the resulting expressions are the same (aside from the spin index).

Dual field. It is customary to define the so-called dual boson field $\theta(x)$, which absorbs the chirality of the field,

$$\phi_\sigma(x) = \phi^R_\sigma(x) + \phi^L_\sigma(x) \,, \qquad \theta_\sigma(x) = \phi^R_\sigma(x) - \phi^L_\sigma(x) \,.$$

As for the chiral fields, we can use the dual fields to define the corresponding charge fields

$$\varphi_c = \phi_\uparrow + \phi_\downarrow \,, \qquad \vartheta_c = \theta_\uparrow + \theta_\downarrow$$

and spin fields

$$\varphi_s = \phi_\uparrow - \phi_\downarrow \,, \qquad \vartheta_s = \theta_\uparrow - \theta_\downarrow \,.$$

The dual field can only be expressed in terms of the conjugate momentum operator as a nonlocal integral because $\partial_x \vartheta = -\Pi$ [124, 140].

Electron-electron interactions. The introduction of an interaction changes the picture, primarily influencing the effective value of the g coupling constants. We consider the general case where we have separated the spin and charge sectors,

and denote the two sectors with the index $\mu = c, s$. Let us rewrite the free part as well,

$$\hat{H}_0 = \sum_\mu \frac{v_F}{2} \int dx \left[(\partial_x \vartheta_\mu)^2 + (\partial_x \varphi_\mu)^2 \right] .$$

The forward scattering processes bosonize to the two forms

$$\hat{H}_{g_2} = \sum_\mu -\frac{v_F g_1^\mu}{2} \int dx \left[(\partial_x \vartheta_\mu)^2 - (\partial_x \varphi_\mu)^2 \right]$$

and

$$\hat{H}_{g_4} = \sum_\mu \frac{v_F g_4^\mu}{2} \int dx \left[(\partial_x \vartheta_\mu)^2 + (\partial_x \varphi_\mu)^2 \right] .$$

The sum of the previous three terms is the bosonized form of the exactly solvable Tomonaga-Luttinger model. In addition, we can combine these quadratic expressions, and, after performing a Boguliobov transformation, find that

$$\hat{H}_{TL} = \sum_\mu \int dx \frac{v_\mu}{2} \left[K_\mu (\partial_x \vartheta_\mu)^2 + \frac{1}{K_\mu} (\partial_x \varphi_\mu)^2 \right] ,$$

where

$$K_\mu = \sqrt{\frac{\pi - g_2^\mu + g_4^\mu}{\pi + g_2^\mu + g_4^\mu}} , \qquad v_\mu = v_F \sqrt{\left(1 + \frac{g_4^\mu}{\pi} \right)^2 - \left(\frac{g_2^\mu}{\pi} \right)^2} .$$

The parameter K_μ is the Luttinger-liquid parameter obtained from the Boguliobov rotation angles. Rescaling the fields by

$$\varphi'_\mu = \varphi_\mu / \sqrt{K_\mu} , \qquad \Pi'_\mu = \sqrt{K_\mu} \Pi_\mu ,$$

we obtain the noninteracting Hamiltonian. The spin and charge sectors are completely disconnected, and v_s, v_c are the excitation velocities, which can now differ. The value of K_μ depends on the strength and type of the interaction terms. For the noninteracting case, $K_\mu = 1$, which corresponds to a critical model.

The backward scattering bosonizes as

$$\hat{H}_{g_1} = \frac{v_F g_1}{2\pi^2} \int dx \cos \left(\sqrt{8\pi} \varphi_s \right)$$

and depends only on the spin field. The umklapp scattering term, which is present only at half filling, bosonizes to a similar expression

$$\hat{H}_{g_3} = \frac{v_F g_3}{2\pi^2} \int dx \cos \left(\sqrt{8\pi} \varphi_c \right) ,$$

which depends only on the charge field.

Gaps. The spin gap and charge gap are related to the presence of the mass term in the renormalized Hamiltonian. The simplest way to understand the behavior of the gaps is to look at the Dirac Hamiltonian $H_F = -iv \int \left(\psi^R \partial_x \psi^R - \psi^L \partial_x \psi^L \right)$ for free fermions. We bosonize this term and add a mass term of the form $m \left(\psi^R \psi^R - \psi^L \psi^L \right)$. Adding such a term induces the system to open a gap in the excitation spectrum around the Fermi energy of size $2m$.

sine-Gordon model. The mass term can only be generated by the cosine term of backward or umklapp scattering processes. The massive forward scattering term is just renormalized. Let us consider the backward scattering term associated with the spin part; the effective model is a bosonic Hamiltonian for $K_s \neq 1$, thus

$$\hat{H}_{sG} = \frac{v}{2} \int dx \left[(\partial_x \vartheta'_s)^2 + (\partial_x \varphi'_s)^2 \right] + \frac{g_1^s}{2\pi^2} \cos \left(\sqrt{8\pi K_s} \varphi'_c \right).$$

The situation is quite complicated: there is a line of fixed points parameterized by K_s [91, 124] rather than a single fixed point. Therefore, K_s is determined by the renormalization flow equations coupling g_1^s and K_s,

$$\frac{dK_s}{d\ell} = -\frac{1}{2\pi^2} K_s^2 g_1^s, \qquad \frac{dg_1^s}{d\ell} = -2g_1^s (K_s - 1) .$$

At weak coupling, the system flows towards strong coupling if $|g_1^s| > 2\pi(K_s - 1)$ (g_1^s is then marginally relevant), while it flows to $g_1^s = 0$ if $|g_1^s| < 2\pi(K_s - 1)$ (g_1^s is marginally irrelevant). Thus, we expect a spin gap for infinitesimal g_1^s and $K_s < 1$ [109]. This expectation is fullfilled for $K_s = 1/2$: the massive Dirac term bosonizes to massive spinons. For a particular coupling of the sine-Gordon model, $K_s = 1$, we can refermionize the system and solve it exactly [141]. The resulting theory is called the Luther-Emery model and is a free theory for spinons [142].

The above analysis can be repeated for the umklapp term, simply replacing g_1^s with g_3^c and K_s with K_c. Thus the charge gap develops if $K_c < 1$ or if $|g_3^c| > 2\pi(K_c - 1)$. As before, massive holons occur when $K_c = 1/2$ [109, 143]. For $K_c = 1/2$, we can invert the transformation and write the Hamiltonian

$$\hat{H}_c = v_F \sum_k \left[(k - k_F) \, \hat{c}_k^{\dagger L} \hat{c}_k^L + (-k - k_F) \, \hat{c}_k^{\dagger R} \hat{c}_k^R \right] + \frac{g_3}{2\pi} \sum_k \left(\hat{c}_k^{\dagger L} \hat{c}_{k-2k_F}^{\dagger R} + \hat{c}_k^{\dagger R} \hat{c}_{k+2k_F}^{\dagger L} \right).$$

This form can be diagonalized in order to obtain the exact expression for the energy dispersion,

$$E_k = \pm \sqrt{v_F^2 \left(k \pm \pi/2 \right)^2 + \Delta^2} ,$$

where $\Delta = g_3/2\pi$ is the gap, and noting that $k_F = \pi/2$ at half-filling [144]. At $K_c \neq 1/2$ the scenario is not changed qualitatively, and we still have an insulator. However, the dependence of the gap changes from linear to $\Delta \sim g_3^\nu$, with $\nu = 1/(2 - 2K_c)$. This should clarify our interpretation of the charge gap.

Momentum distribution. We have expressed the correlation functions in terms of the Boguliobov transformation obtained for the forward scattering in the simplified case where $K_s = 1$ and $K_c \neq 1$. Thus, the generic expression for the momentum distribution is

$$n(k) = n(k_F) - \text{const.}\,\text{sgn}(k - k_F)|k - k_F|^{\alpha_c}\,,$$

where $\alpha_c = (K + K^{-1} - 2)/4$. Therefore, the one-particle density of states diverges with the same exponent, $\rho(\omega) \sim |\omega|^{\alpha_c}$. Thus, the momentum distribution function and the density of states have power-law singularities at the Fermi level, with a vanishing single-particle density of states at the Fermi energy. The absence of a step at k_F in the momentum distribution function implies the absence of a quasiparticle peak, and thus a behavior that differs from a Fermi liquid. Note that the exponents of the bosonized version of the correlation functions associated with the relevant order parameters are determined by other combinations of the Boguliobov parameter K_μ [39]. These correlation functions with their power-law variations are experimentally [38,39,124] and numerically [145–147] accessible quantities. However, since the precise expression of K_μ depends on the details of the model [39,124], we cannot extract information from its value unless we already know what happens [38,147–149]. The remarkable fact is that there is only one coefficient, K_μ, which determines all the asymptotic power laws [144].

Generalizations. We have discussed only the Abelian formulation of bosonization, applicable because a single compact boson φ has $U(1)$ symmetry. The extension to non-Abelian bosonization can be particularly useful in the context of the Wess-Zumino-Witten (WZW) models [98, 124, 140], and is relevant for high spin models. More about bosonization can be found in the review articles [139, 140, 150–153]. Applications to ladder models can be found in Refs. [34, 39, 154, 155]. The extension to higher dimension was originally obtained by Luther [156], but was later formulated as the modern multidimensional scheme [152] by Haldane [157]. An extension of his approach based on functional integrals has also been derived [158–160].

We can conclude that any one-dimensional system dominated by the forward scattering process is a Luttinger liquid. Nevertheless, spontaneous symmetry breaking and dynamical gap generation can lead to different phases, and, due to the spin-charge separation, these mechanism can take place differently in each sector. The spin and charge sectors are almost always uncoupled in one dimension, except that they can be coupled by an external field for particular filling [144,161].

New studies of exact solvable models, in connection with the random matrix theory [162], have recently pointed out that highly non-homogeneous states have to be related to a non-linear spectrum near the Fermi energy [163]. Any curvature of the

spectrum mixes charge and spin degrees of freedom, making bosonization impracticable. To overcome the bosonization of non-linear theory, we push forward the Luttinger-liquid paradigm and argue that a quantum system should be described by collective modes and the non-linear effects are encoded in the hydrodynamic equations [164].

1.3 Conformal field theory

In conformal field theory, the fields have particular space-time symmetries which can be derived by conformal transformations. A conformal map or transformation is a function which preserves angles [165]. As we have seen at the begin of the chapter, critical models are fixed points of the renormalization group, and therefore they are scale invariant. Conformal invariance is a subgroup of scale invariance, allowing us to apply conformal field theory to critical phenomena. In two dimensions, conformal mapping is particular useful. In fact, the set of conformal transformations is equivalent to the set of analytical functions on the complex plane [166].

In the following, we briefly summarize the result obtained from applying conformal field theory [167] to statistical mechanical models that are conformally invariant on large scale at a critical point. More material can be find in a large collection of lectures notes and review articles [168–173], and books [53, 98, 100, 174].

The capabilities of conformal field theory include the classification of universality classes, the calculation of the critical exponents, the calculation of other universal amplitudes, including finite-size effects at criticality and ratios of thermodynamic quantities away from criticality, and the calculation of correlation functions, both at and away from criticality [98, 100].

Conformal transformation and correlation functions

Let us consider a field Φ which depends on the space-time variable $\mathbf{x}$. The dynamics is determined by the action

$$S[\Phi] = \int dx^{\mu} \mathcal{L} \left(\Phi, \partial_{\mu} \Phi \right) .$$

All physical quantities can be expressed by the path integral formalism as correlation functions

$$\langle \Phi_1(\mathbf{x}_1) \dots \Phi_n(\mathbf{x}_n) \rangle = \frac{1}{Z} \int [d\Phi] \Phi_1(\mathbf{x}_1) \dots \Phi_n(\mathbf{x}_n) e^{-S[\Phi]} ,$$

where $Z = \int [d\Phi] e^{-S[\Phi]}$ is the partition function. Any symmetry transformation changes position, $\mathbf{x} \rightarrow \mathbf{x}'$, and field, $\Phi(\mathbf{x}) \rightarrow \Phi'(\mathbf{x}') = \mathcal{F}[\Phi(\mathbf{x})]$, so that the action

is unchanged: $S[\Phi'] = S[\Phi]$; i.e., the Jacobian is trivial. Therefore, correlation functions transform as

$$\langle \Phi_1(\mathbf{x}'_1) \dots \Phi_n(\mathbf{x}'_n) \rangle = \langle \mathcal{F}[\Phi_1(\mathbf{x}_1)] \dots \mathcal{F}[\Phi_n(\mathbf{x}_n)] \rangle .$$

In $1+1$ dimensions, $\mathbf{x}$ represents a point in a real two-dimensional space, which maps to complex variables $z = x^0 + ix^1$ and $\overline{z} = x^0 - ix^1$. In the complex representation, rotation through an angle θ becomes

$$z' = e^{i\theta} z \qquad \overline{z}' = e^{-i\theta} \overline{z} ,$$

and the correlation functions can be easily written

$$\langle \Phi_1(e^{i\theta} z_1, e^{-i\theta} \overline{z}_1) \dots \Phi_n(e^{i\theta} z_n, e^{-i\theta} \overline{z}_n) \rangle = e^{i(s_1 + \dots + s_n)} \langle \Phi_1(z_1, \overline{z}_1) \dots \Phi_n(z_n, \overline{z}_n) \rangle ,$$

where s is the spin. In presence of scale invariance, the coordinates and the field change as

$$\mathbf{x}' = \lambda \mathbf{x} \qquad \Phi'(\lambda \mathbf{x}) = \lambda^{-\Delta} \Phi(\mathbf{x}) ,$$

where Δ is the scale dimension of the field Φ. Thus, correlation functions transform as

$$\langle \Phi(\lambda \mathbf{x}_1) \dots \Phi(\lambda \mathbf{x}_n) \rangle = \lambda^{-(\Delta_1 + \dots + \Delta_n)} \langle \Phi(\mathbf{x}_1) \dots \Phi(\mathbf{x}_n) \rangle .$$

We combine the dilatation and the rotation and thus define the conformal weights $(h, \overline{h})$ as

$$h = \frac{1}{2} (\Delta + s) \qquad \overline{h} = \frac{1}{2} (\Delta - s) .$$

During a conformal transformation, fields change via a local dilatation, $\lambda(x)$, rather than a uniform one. In two dimensions, the field that transforms as

$$\Phi'(w, \overline{w}) = \left(\frac{dw}{dz} \right)^{-h} \left(\frac{d\overline{w}}{d\overline{z}} \right)^{-\overline{h}} \Phi'(z, \overline{z})$$

under all conformal transformations is called the primary field.

The two-point correlation function $\langle \phi_1 \phi_2 \rangle$ of a conformal field theory in two dimensions reduces to

$$\langle \phi(z, \overline{z}) \phi(0, 0) \rangle = \left(\frac{1}{z^2} \right)^{h} \left(\frac{1}{\overline{z}^2} \right)^{\overline{h}} \times \text{const.}$$

It therefore follows that conformal field theories are critical, characterized by power-law correlation functions, and that the conformal weights determine the physics.

A conformal field theory has to be covariant with respect to a conformal transformation. Thus, we use an analytical transformation to map the plane to a finite region, i.e., a cylinder of circumference L,

$$w = \frac{L}{2\pi} \ln z \qquad z = \exp \frac{2\pi w}{L} \,.$$

The two-point correlation function on a cylinder is obtained by the simple transformation

$$\langle \phi(w_1, \overline{w}_1) \phi(w_2, \overline{w}_2) \rangle_{\text{cyl.}} = \left(\frac{2\pi}{L} \right)^{2\left(h+\overline{h}\right)} \left[2 \sinh \frac{\pi \left(w_1 - w_2 \right)}{L} \right]^{-2h} \left[2 \sinh \frac{\pi \left(\overline{w}_1 - \overline{w}_2 \right)}{L} \right]^{-2\overline{h}} \,.$$

Substituting in the result real coordinates $w_1 - w_2 = u + iv$, and considering the case with $u >> L$, we obtain

$$\langle \phi(u, v) \phi(0, 0) \rangle_{\text{cyl.}} \sim \exp \left(-\frac{2\pi \Delta u}{L} \right) \,,$$

where the exponential decay term sets the correlation length of the system to $\xi_L = L/(2\pi\Delta)$. The cylindrical space-time represents an infinitely long system at finite temperature ($L = \beta = 1/T$) or a finite system at $T = 0$ with periodic boundary conditions. In the last case, the coordinate u is the imaginary time τ. In general, the two-point correlation function, $\langle \phi(x, 0) \phi(x, \tau) \rangle$, can be expanded in eigenstates of the Hamiltonian [80],

$$\langle \phi(x, 0) \phi(x, \tau) \rangle = \sum_n e^{-(E_n - E_0)\tau} |\langle 0|\phi(x, 0)|n\rangle|^2 \,.$$

In the limit $\tau \to \infty$, the gaps between the ground state and the lowest exited states are the dominant contributions. It follows that $\langle \phi(x, 0) \phi(x, \tau) \rangle \sim \exp\left(E_1 - E_0 \right) \tau$ for $\tau \to \infty$, and we can write

$$E_1 - E_0 = \frac{2\pi \Delta}{L} \,.$$

Thus, in finite-size systems in a critical regime, the *mass gap* has to scale to zero linearly with the system size. However, the correct expression includes the velocity of the excitation v_e. In fact, the gap then scales as $E_1 - E_0 = (2\pi v_e \Delta)/L$.

Central charge

Any quantum field theory must be translationally and rotationally invariant. Translation invariance leads to, via Noether's theorem, the energy-momentum conservation law [175–177]

$$\partial^\mu T_{\mu\nu} = 0 \,.$$

where $T_{\mu\nu}$ is the stress energy tensor [45]. This operator is not a primary operator, see Ref. [98, 169, 178]. In fact, its two-point function has form

$$\langle T(z)T(0)\rangle = \frac{c/2}{z^4} \,.$$

This expression defines the conformal anomaly number or conformal charge c. It is an universal constant and depends on which particular fixed-point theory we are considering. The extra conformal-charge term results from the mapping to a finite system [165, 179] and is a manifestation of the Casimir effect [180].

The central charge is additive. In fact, two field theories added together without coupling have their energy-momentum tensor added. Thus, the central charge adds. In a sense, the central charge measures the number of gapless modes which a system has, weighting them differently because the central charge for fermions differs from that for bosons.

In the following, we present a summary of the results obtained by conformal field theory applied to several critical models. Many analogies arise interpreting the central charge as number of "basic" modes. In fact, critical models with the same central charge can always be mapped to each other.

Free boson. The action for the massless free boson CFT is

$$S[\phi] = \frac{g}{2} \int d\mathbf{x}\, \partial_\mu \varphi \partial^\mu \varphi \,.$$

The two-point correlation function is then

$$\langle \varphi(z,\overline{z})\varphi(w,\overline{w})\rangle = -\frac{1}{4\pi g} \ln|z-w|^2 \,,$$

and the central charge for the massless free boson is $c=1$.

Massless free fermion. An important example of CFT is the massless free Majorana-Weyl fermion, for which the action is

$$S[\chi] = f \int d\mathbf{x} \left(\overline{\chi}\partial\overline{\chi} + \chi\overline{\partial}\chi \right) \,,$$

and the two-point correlation function

$$\langle \chi(z)\chi(w)\rangle = \frac{1}{2\pi f}\frac{1}{z-w} \,.$$

The central charge for a Majorana fermion is $c=1/2$. Any Dirac fermion can be defined as a combination of two Majorana fermions

$$\psi(z) = \frac{1}{\sqrt{2}} \left(\chi_1(z) + i\chi_2(z) \right) \,,$$

and the central charge of a Dirac fermion is $c = 1$, and can be expressed as the sum of two Majorana fermions or as one free boson.

Generalized free fermion. A generalization of the free-fermion system to include two types of anti-commuting fermions, b and c, with weight j and $1-j$, is called the bc-model. This model has central charge $c = -2(6j^2 - 6j + 1)$ [98, 173]. A variation of the model is the $\beta\gamma$-model with two commuting fields β and γ of weight j and $1 - j$, respectively. In this case the central charge is given by $c = 2(6j^2 - 6j + 1)$.

Boson with background charge. A variant of the free boson theory can be obtained which includes a coupling between the boson and the scalar curvature $(\sqrt{\tilde{g}})$,

$$S[\phi] = \frac{g}{4\pi} \int\int d^2z \partial\phi\overline{\partial}\phi + \frac{ie_0}{4\pi} \int\int d^2z \sqrt{\tilde{g}}\mathrm{R}\phi \,.$$

The constant e_0 is the background charge, and the expression for the central charge is now $c = 1 - \frac{6}{g}e_0^2$.

Minimal models. An important class of CFT is that of the Minimal Models. Minimal models corresponding to unitary CFTs identify many statistical models as Ising and Potts model variants. The central charge is $c = 1 - \frac{6}{r(r+1)}$ for $r = 3, 4, 5, \ldots$, and the models are called Unitary Minimal models (UMM) [98, 169, 170, 173].

Wess-Zumino-Witten models. The Wess-Zumino-Witten (WZW) models are conformally invariant theories that have supplementary symmetries, e.g., $\mathrm{SU}(n)$. The WZW field G is a matrix that represents a particular Lie group and the action is

$$
\begin{aligned}
S[G] \;&=\; \frac{k}{8\pi} \int d^2x \mathrm{Tr}\left(\partial^\mu G^{-1}\partial_\mu G\right) \\
&+\; -\frac{ik}{12\pi} \int_{\mathcal{B}} d^2x \varepsilon_{\mu\nu\lambda} \mathrm{Tr}\left(G^{-1}\partial^\mu G G^{-1}\partial^\nu G G^{-1}\partial^\lambda G\right) ,
\end{aligned}
$$

where k is an integer representing the level of the model. The second term of the action is a topological term and the central charge for these models is given by

$$c = \frac{3k}{k+2} \,.$$

Therefore, this result combines with the bosonization idea. Abelian bosonization establishes a correspondence between the Dirac field ψ and the free massless boson both with central charge one. Non-Abelian bosonization instead establishes a correspondence between multiplets of fermions and different WZW models.

Entropy

Recently, conformal field theory has been applied in the context of the holographic principle [181]. Several predictions of the entanglement entropy have been derived in models of black holes and quantum gravitation [182–184]. The field theories used in condensed matter theory have been also explored [185–187].

As a system, we can consider an arbitrary lattice model or a quantum field theory including conformal field theory. We start from the expression of the reduced density matrix ρ_A to calculate the entanglement entropy S_A. First, we evaluate $\text{Tr}_A \rho_A^n$, then differentiate it with respect to n, and finally take the limit $n \to 1$. Recalling that ρ_A is normalized so that $\text{Tr}_A \rho_A = 1$, we calculate

$$
\begin{aligned}
S_A &= -\text{Tr}_A \rho_A \ln \rho_A \\
&= \lim_{n \to 1} \frac{\text{Tr}_A \rho_A^n - 1}{1 - n} \\
&= -\frac{\partial}{\partial n} \text{Tr}_A \rho_A^n \bigg|_{n=1}
\end{aligned}
\tag{1.10}
$$

This is called the replica trick. The expression $S_n = \frac{\text{Tr}_A \rho_A^n - 1}{1-n}$ is called the Tsallis entropy [188]. Therefore, we have to evaluate $\text{Tr}_A \rho_A^n$, which is given in terms of path integral on the n-sheeted replica surface as

$$
\text{Tr}_A \rho_A^n = \frac{Z(n)}{[Z(1)]^n} \, .
$$

Thus, this entropy is related to the product of correlation functions with the corresponding boundary conditions [186, 189].

1.4 Summary

In this chapter, we have described how to characterize quantum critical phenomena. The notion of the renormalization group and the finite-size analysis, which we have introduced at the begin of the chapter, represents the set of knowledge used to interpret our numerical data. Numerical simulations are performed on finite systems, which behave in a way which can be far from the thermodynamic limit. However, finite-size scaling analysis guarantees correct evaluation of the critical point and the critical exponents without involving the thermodynamic limit directly. Thus, we combine finite-size scaling analysis and the density matrix renormalization group method, which we introduce in the next chapter, to characterize phase transitions with high accuracy.

Bosonization and conformal field theory, introduced in the second part of the chapter, represent the basis of our understanding of strongly correlated systems.

Spin-charge separation, the opening of a charge gap or a spin gap, and the Luttinger liquid concept, are all results derived using bosonization. Correlation functions are also obtained by bosonization, and can then used to characterize particular phases. However, the success of the bosonization technique relies on the correctness of the model to describe particular physical phenomena, and on the correct use and interpretation of the bosonization recipes. Two of our projects focus on testing the results obtained by bosonization.

Some of the results obtained in conformal field theory have been summarized to make them more accessible to the reader. In the following chapters, the central charge, the calculation of the critical exponents, the interpretation of finite-size scaling, and the classification of the universality class are frequently used. Conformal field theory can be seen as the theory of the critical region, where all numerical methods have limitations. An understanding of CFT can help to retain control of the simulation and can be used to extract valuable information.

In the next chapter, we introduce the density matrix renormalization group starting from basic notions, and discuss relevant extensions. In particular, we discuss its close relation to exact diagonalization methods and its deep connection with quantum information theory.

2 Density Matrix Renormalization Group

There are numerous numerical methods that can be used to study quantum-mechanical many-body systems [190–192]. In the last years, due to the increasing interest in strongly correlated systems, much effort has been invested to develop new numerical techniques [193]. The main goal is to solve the Schrödinger equation for a large system of interacting particles

$$\mathcal{H}|\Psi\rangle = E|\Psi\rangle.$$

In principle, after mapping the problem onto a lattice and taking into account all possible symmetries, a complete diagonalization can be carried out. However, this is possible only for very small systems because it becomes extremely expensive in terms of memory and computational effort as the system size increases. More efficient methods use the concept of invariant subspaces and represent the Hamiltonian as a sparse matrix. The diagonalization is performed iteratively, building a subspace of the Hilbert space, the Krylov space, from powers of the Hamiltonian operator. The Lanczos algorithm belongs to this class, and it can be used to obtain the low-energy spectrum of a finite system numerically exactly. Nevertheless, iterative diagonalization imposes limits on the maximum size of the system that can be studied. The Density Matrix Renormalization Group (DMRG) overcomes some of these limitations by combining the concept of renormalization group and quantum information theory. The algorithm uses techniques from iterative exact diagonalization, but the system basis is not obtained exactly, but rather by performing a basis truncation at each step of an iterative process in which the chain is built up a site at a time. This algorithm can be considered to be exact only in a variational way.

In the first section of this chapter, we briefly discuss the exact diagonalization method and the numerical representation of the quantum mechanics basis, both of which are also relevent to the DMRG. The second section introduces some basic ideas and results from quantum information theory. In particular, we make a connection between the property of criticality of a finite system and its description in terms of a finite system basis. The last section describes the DMRG method: the density matrix projection, the algorithm, the measurements, and concludes with an analysis in terms of the von Neumann entropy [194].

2.1 Exact diagonalization

In this section we introduce exact diagonalization as an iterative method, i.e., the Lanczos and the Davidson algorithms. However, a short digression on the numerical representation of many-body states on a lattice is necessary, which also serves to introduce the concept of a lattice and of a local basis for different systems.

The numerical study of a quantum Hamiltonian requires its definition on a finite lattice, in contrast to the quantum field theory approaches that are defined in the continuum and in the thermodynamic limit. The finite size L of a chain determines the infrared cutoff. The momentum space is discrete with steps $\Delta k = 2\pi/L$. In contrast, the lattice spacing a fixes the maximum momentum to $2\pi/a$, defining the ultraviolet cutoff. However, the low-energy properties of a continuum model should not differ from those of the corresponding lattice model. If differences occur, they occur at short distances, high energies, and short times [195, 196]. Insight can be gained from comparison with exact methods such as the Bethe Ansatz or matrix product states, both of which are defined on a lattice [95, 197–200].

The main idea is to diagonalize the Hamiltonian in a particular basis. For example, we consider the Hubbard model expanded in Bloch states

$$H = \sum_{k,\sigma} \varepsilon(k) \hat{c}_{k,\sigma}^\dagger \hat{c}_{k,\sigma} + \frac{U}{L} \sum_{k_1,k_2,k_3} \hat{c}_{k_1,\uparrow}^\dagger \hat{c}_{k_2,\downarrow}^\dagger \hat{c}_{k_3,\downarrow} \hat{c}_{k_1+k_2-k_3,\uparrow} \,,$$

and expanded in Wannier states

$$H = -t \sum_{i,\sigma} \hat{c}_{i,\sigma}^\dagger \hat{c}_{i+1,\sigma} + U \sum_i \hat{n}_{i,\uparrow} \hat{n}_{i,\downarrow} \,.$$

The Bloch states diagonalize the kinetic term, but not the interaction term; the latter term is difficult to reduce to any local short-range form [201, 202]. Thus, Bloch states are optimal only for weak interactions. In contrast, the Wannier states diagonalize the interaction term and are therefore preferred for numerical calculation because it is possible to simulate local quantum and thermal fluctuations on finite-size systems. Unless we explicitly include nonlocal terms, the matrix representation is sparse, i.e., only a small portion of the matrix elements are nonzero. This sparseness can be used to advantage in efficiently storing the matrix and in calculating its product with vectors.

2.1.1 Numerical representation

In order to be able to represent all the states in a compact and efficient way and take full advantage of the sparse matrix form of the Hamiltonian, we need to

choose our local basis optimally. In fact, the wave function of the system can be represented in the space spanned by the tensor product of local basis states like

$$|\phi_k\rangle = |s_1, \ldots, s_L\rangle = |s_1\rangle \otimes \cdots \otimes |s_L\rangle \,.$$

The local basis should be easy to generate and to perform operations on, should require a modest amount of memory and should provide fast access. The use of symmetries is also important. The description for spin and electronic systems follows.

Spin-$1/2$ **systems.** The single-site basis consists of two states: spin up $|\uparrow\rangle$, and spin down $|\downarrow\rangle$. Instead of the spin value $s_i^z = \pm 1/2$, it is useful to use the occupation number of one of the spin types, $n_i = s_i^z + 1/2$, as a basis. Starting from the single-site basis, we can form a complete basis of a chain of length L by forming the direct product of single-site states. The Hilbert space has size $\mathcal{N} = 2^L$. A convenient way of representing a state is to map it to an integer

$$I = \sum_{i=1}^{L} n_i 2^{i-1} \,.$$

This allows us to save storage and speed up the calculation by doing bitwise operations [203]. For example

$$|\phi_1\rangle = |\uparrow_1 \downarrow_2 \downarrow_3 \downarrow_4\rangle \rightarrow |1000\rangle \rightarrow I = 1 \,,$$

$$|\phi_3\rangle = |\uparrow_1 \uparrow_2 \downarrow_3 \downarrow_4\rangle \rightarrow |1100\rangle \rightarrow I = 3 \,,$$

and

$$s_{i=3}^+ |\phi_3\rangle = |\uparrow_1 \uparrow_2 \uparrow_3 \downarrow_4\rangle \rightarrow |1110\rangle \rightarrow I = 7 \rightarrow |\phi_7\rangle \,.$$

Any state in the Hilbert space is a linear combination of such basis states

$$|\Psi\rangle = \sum_I c(I) |\phi_I\rangle \,.$$

Since, in many physical cases, the z-component of the total spin, $S^z = \sum_i^L s_i^z$, commutes with the Hamiltonian, the matrix Hamiltonian is block-diagonal, and the dimension of each sector reduces to

$$\mathcal{N}(s^z) = \binom{L}{s^z + L/2} \,.$$

Other symmetries, such as translation, reflection, discrete rotation symmetries, can also be taken into account to decompose the Hamiltonian into smaller block-diagonal matrices.

Spin-1 **systems.** The approach is similar to the spin-1/2 system, but there are three states per site: $S_i^z = -1, 0, 1$. The complete Hilbert space grows as 3^L. The generalization to higher spin value holds as well; for a spin S system we have $2S + 1$ states each site, with $S_i^z = -S, -S + 1, ..., S$, and $(2S + 1)^L$ states in total.

Electron systems. Usually we use the Hubbard basis. For each site there are four basis states:

$$
\begin{aligned}
&|0\rangle_i, \\
&| \uparrow \rangle_i = && \hat{c}_{i,\uparrow}^\dagger |0\rangle_i \\
&| \downarrow \rangle_i = && \hat{c}_{i,\downarrow}^\dagger |0\rangle_i \\
&| \uparrow\downarrow \rangle_i = && \hat{c}_{i,\uparrow}^\dagger \hat{c}_{i,\downarrow}^\dagger |0\rangle_i &,
\end{aligned}
\tag{2.1}
$$

where $\hat{c}_{i,\sigma}^\dagger$ creates a spin σ electron in the Wannier orbital centered on the site i. The total Hilbert space of the lattice is the direct product of the single-site Hilbert spaces. Therefore, the Hilbert space grows with the system size as 4^L. Generalizing the spin-1/2 encoding case, two integers are now required to index the basis states:

$$
I^\uparrow = \sum_i^L n_i^\uparrow 2^{i-1}, \quad I^\downarrow = \sum_i^L n_i^\downarrow 2^{i-1},
$$

where $n_i^\uparrow$ and $n_i^\downarrow$ are the occupation numbers of spin up and spin down on site-i, respectively. Therefore, a generic state is described by

$$
|\Psi\rangle = \sum_{I^\uparrow, I^\downarrow} C(I^\uparrow, I^\downarrow)|\phi_{I^\uparrow}, \phi_{I^\downarrow}\rangle .
$$

In systems where the spin and electron numbers are conserved, the total number of electrons with spin up, $N^\uparrow$, and spin down, $N^\downarrow$, are good quantum numbers. Therefore, the number of states in a specific sector with given $N^\uparrow$ and $N^\downarrow$ is

$$
\mathcal{N}(N^\uparrow, N^\downarrow) = \begin{pmatrix} L \\ N^\uparrow \end{pmatrix} \begin{pmatrix} L \\ N^\downarrow \end{pmatrix} .
$$

Eliminating the possibility of having double occupancy reduces this number even further to

$$
\mathcal{N}(N^\uparrow, N^\downarrow, N^{\uparrow\downarrow} = 0) = \frac{L!}{N^\downarrow! N^\uparrow! (L - N^\downarrow - N^\uparrow)!} .
$$

The use of translational invariance or other symmetries can further reduce the dimension of the relevant sectors of the Hilbert space.

We are now able to represent a basis of different finite systems and to apply any operator. We now proceed by describing iterative diagonalization. The first method is the Lanczos algorithm, then the Davidson algorithm is also treated.

2.1.2 Lanczos method

Using the Lanczos algorithm [204], we iteratively construct a special basis in which the Hamiltonian has tridiagonal form. The starting point is an arbitrary and normalized wave function, $|\varphi_1\rangle$ that can be expanded in the basis $\{\phi_k\}$ as

$$|\varphi_1\rangle = \sum_k^{\mathcal{N}} a_k |\phi_k\rangle. \tag{2.2}$$

We apply the Hamiltonian to $|\varphi_1\rangle$ and construct a normalized vector $|\varphi_2\rangle$, which is orthogonal to the previous one

$$\beta_2 |\varphi_2\rangle = \hat{H} |\varphi_1\rangle - \alpha_1 |\varphi_1\rangle. \tag{2.3}$$

From the orthogonality condition $\langle\varphi_2|\varphi_1\rangle = 0$, we obtain $\alpha_1 = \langle\varphi_1|\hat{H}|\varphi_1\rangle$. From the scalar product of $\langle\varphi_2|$ and $\langle\varphi_2|\beta_2$ with Eq.(2.3) and, requiring that $\langle\varphi_2|\varphi_2\rangle = 1$, we obtain $\beta_2 = \langle\varphi_2|\hat{H}|\varphi_1\rangle$ and $\beta_2^2 = \langle\varphi_2|\hat{H}^2|\varphi_2\rangle - \alpha_1^2$, respectively.

We continue applying the Hamiltonian and construct a third state which is orthogonal to the previous two,

$$\beta_3 |\varphi_3\rangle = \hat{H} |\varphi_2\rangle - \alpha_2 |\varphi_2\rangle - \gamma_a |\varphi_1\rangle, \tag{2.4}$$

where the conditions of orthogonality $\langle\varphi_2|\varphi_3\rangle$ and $\langle\varphi_1|\varphi_3\rangle$ require that $\alpha_2 = \langle\varphi_2|\hat{H}|\varphi_2\rangle$ and $\gamma_a = \beta_2$. The normalization of $|\varphi_3\rangle$ demands that $\beta_3 = \langle\varphi_3|\hat{H}|\varphi_2\rangle$.

In the next step, an important property of the Lanczos procedure emerges. Applying the Hamiltonian and projecting out the previous states, the expression for the fourth state becomes

$$\beta_4 |\varphi_4\rangle = \hat{H} |\varphi_3\rangle - \alpha_3 |\varphi_3\rangle - \gamma_c |\varphi_2\rangle - \gamma_b |\varphi_1\rangle, \tag{2.5}$$

The conditions of orthogonality, $\langle\varphi_3|\varphi_4\rangle$, $\langle\varphi_2|\varphi_4\rangle$, and $\langle\varphi_1|\varphi_4\rangle$ require that $\alpha_3 = \langle\varphi_3|\hat{H}|\varphi_3\rangle$, $\gamma_c = \beta_3$ and $\gamma_b = 0$. Therefore, constructing $|\varphi_4\rangle$ to be orthogonal to $|\varphi_3\rangle$ and $|\varphi_2\rangle$ makes it automatically orthogonal to $|\varphi_1\rangle$, and $|\varphi_1\rangle$ need not appear explicitly in the equation.

The final form of the algorithm can be obtained by recursion, assuming that the equation

$$\beta_{n+1} |\varphi_{n+1}\rangle = \hat{H} |\varphi_n\rangle - \alpha_n |\varphi_n\rangle - \beta_n |\varphi_{n-1}\rangle \tag{2.6}$$

holds for $|\varphi_{n+1}\rangle$ and showing that it is valid for $|\varphi_{n+2}\rangle$, where $\beta_{n+1} = \langle\varphi_{n+1}|\hat{H}|\varphi_n\rangle$, $\beta_n = \langle\varphi_n|\hat{H}|\varphi_{n-1}\rangle$, and $\alpha_n = \langle\varphi_n|\hat{H}|\varphi_n\rangle$.

Altogether, at each Lanczos step, we have to orthogonalize the state vector with respect to the previous two vectors. The implementation of the Lanczos algorithm, which builds a orthonormal basis $\{|\varphi_1\rangle, \ldots, |\varphi_M\rangle\}$ for the Krylov subspace [205] is summarized here:

1. We set $\beta_1 = 0$, $|\varphi_0\rangle = 0$,

2. from $i = 1$ to M:

   a) Evaluate the coefficient α_i at step i

   $$\alpha_i = \langle \varphi_i | \hat{H} | \varphi_i \rangle .$$

   b) Calculate the unnormalized state vector (rounded ket)

   $$|\varphi_{i+1}) = \hat{H} |\varphi_i\rangle - \alpha_i |\varphi_i\rangle - \beta_i |\varphi_{i-1}\rangle .$$

   c) Calculate the β_{i+1} coefficient

   $$\beta_{i+1}^2 = (\varphi_{i+1} | \varphi_{i+1}) .$$

   d) If $\beta_{i+1} = 0$, stop.

   e) Normalize the vector

   $$|\varphi_{i+1}\rangle = \frac{|\varphi_{i+1})}{\beta_{n+1}} .$$

   f) Continue from (a).

Some of these quantities have direct physical meaning, such as the average energy of $|\varphi_n\rangle$, $\alpha_n = \langle \varphi_n | \hat{H} | \varphi_n \rangle$, and its mean square energy deviation, $\langle \varphi_n | \hat{H}^2 | \varphi_n \rangle - \alpha_n^2 = \beta_{n+1}^2 + \beta_n^2$. Rewriting Eq.(2.6) as

$$\hat{H} |\varphi_n\rangle = \beta_{n+1} |\varphi_{n+1}\rangle + \alpha_n |\varphi_n\rangle + \beta_n |\varphi_{n-1}\rangle$$

shows directly how, in this basis, the Hamiltonian becomes

$$\mathbf{H} = \begin{pmatrix} \alpha_1 & \beta_2 & 0 & \dots & 0 \\ \beta_2 & \alpha_2 & \beta_3 & \ddots & 0 \\ 0 & \beta_3 & \alpha_3 & \ddots & 0 \\ \vdots & \vdots & \ddots & \ddots & \beta_M \\ 0 & 0 & 0 & \beta_M & \alpha_M \end{pmatrix} . \tag{2.7}$$

Thus it is tridiagonal and can be easily diagonalized using standard routines [203, 205–208]. The eigenvalues of (2.7) converge to the extremal eigenvalues of the original Hamiltonian $\hat{H}$, and its eigenstates can be expressed in the Lanczos basis,

$$|\Psi_0\rangle = \sum_i \gamma_i |\varphi_i\rangle . \tag{2.8}$$

Since it is usually not convenient to store all of the Lanczos vectors $|\varphi_i\rangle$, we calculate the γ_i coefficients, storing only two vectors at the time. Subsequently, we can reconstruct the eigenvectors by running a second Lanczos procedure in order to build up $|\varphi_0\rangle$ in the original $\{|\phi_k\rangle\}$ basis. In practice, we can reduce the original matrix eigenvalue problem to a more tractable problem, because $n << \mathcal{N}$ and $n \sim 10^2$ steps are typically sufficient to converge to the ground state and only few vectors must be stored.

Although the method is exact in theory, successive Lanczos vectors in fact lose their orthogonality due to numerical round-off errors after many iterations. This problem can also manifest itself as the appearance of ghost states in the spectrum. The simplest cure is a full orthogonalization, where the new vectors have to be explicitly orthogonalized with respect to all the previous ones. The cure is robust, but the vectors need to be kept in memory and the cost of orthogonalization is high. A more efficient solution originates from the Paige's analysis [209–211], which shows that the Lanczos vectors start to lose orthogonality as soon as an eigenvalue of the **H** stabilizes and concludes that, until this situation occurs, no full orthogonalization is required. A clever technique to do this was proposed by Cullum and Willoughby [212].

Although the simplest form of the Lanczos algorithm is still used to find the extremal eigenstates of large matrices, modified versions or other methods are often better, depending of the type of problem to solve. However, the Lanczos algorithm can be extended straightforwardly to calculate dynamical [193, 213] and temperature-dependent [214] quantities. Nevertheless, new techniques, such as using a Chebyshev expansion to calculate dynamical quantities, can achieve better stability [215].

2.1.3 The Davidson method

The method of Davidson [216] is usually suitable for problems where the Hamiltonian is sparse and has a large diagonal-dominance ratio. The term diagonal-dominance ratio refers to the ratio $d = \min_{ij} |(H_{ii} - H_{jj})/H_{ij}|$. In Lanczos, we build an easy-to-compute three-term recurrence and project the Hamiltonian onto the Krylov subspace of order M. However, a large number of iterations may be required before a sufficiently invariant subspace is found.

The Davidson method reduces the number of iterations at the expense of a more complicated step. In fact, a perturbative scheme is used to efficiently estimate the eigenvectors. The vector basis is built up using the residual of the previous vector and a diagonal preconditioner. Thus, the subspace formed provides better information about the required eigenvectors than the Krylov subspace.

The algorithm to calculate the lowest k eigenvalues is summarized as follows:

1. Choose $\ell \geq k$ orthonormal vectors, $|u_1\rangle$, $|u_2\rangle$, ..., $|u_\ell\rangle$ and define **B** as the rectangular matrix containing these vectors as columns.

2. Apply the Hamiltonian to these states to form the vectors $|w_1\rangle = \hat{H}|u_1\rangle$, $|w_2\rangle = \hat{H}|u_2\rangle$, ..., $|w_\ell\rangle = \hat{H}|u_\ell\rangle$ and the rectangular matrix **A** which contains these vectors as columns.

3. Form the $(\ell \times \ell)$-square matrix $\mathbf{C} = \mathbf{B^T A}$ and diagonalize it exactly, obtaining the ℓ eigenvalues, λ_1^ℓ, $\cdots$, λ_ℓ^ℓ, and ℓ eigenvectors, $|z_1^\ell\rangle$, $\cdots$, $|z_\ell^\ell\rangle$.

4. Test the convergence of the first k vectors by forming the residual vector

$$|q^\ell\rangle = \left(\mathbf{A} - \lambda_k^\ell \mathbf{B}\right)|z_k^\ell\rangle$$

   and calculate its norm. If $|| |q^\ell\rangle|| < \varepsilon$, then consider the procedure converged and stop, concluding that λ_1^ℓ, $\cdots$, λ_k^ℓ and $|\psi_1\rangle = \mathbf{B}|z_1^\ell\rangle$, $\cdots$, $|\psi_k\rangle = \mathbf{B}|z_k^\ell\rangle$ are eigenvalues and eigenstates of the Hamiltonian. Otherwise, continue.

5. Extend the basis by using the correction vector (diagonal preconditioner)

$$|r^\ell\rangle = \left(\mathbf{D} - \lambda_k^\ell \mathbf{I}\right)^{-1}|q^\ell\rangle,$$

   where **D** is a matrix containing the diagonal elements of **H** and **I** is the unit matrix. Orthonormalize $|r^\ell\rangle$ against $|u_1\rangle$, $\cdots$, $|u_\ell\rangle$ to form $|u_{\ell+1}\rangle$.

6. Expand the matrix **B** and **A** by adding $|u_{\ell+1}\rangle$ and $|w_{\ell+1}\rangle = \hat{H}|u_{\ell+1}\rangle$ as additional columns. Set $\ell = \ell + 1$ and continue from step 2.

The starting point is usually a set of orthogonal random vectors. However, to speed up the convergence and reduce the storage space needed, a set of vectors from a previous step can be used instead and the process can be iterated. There is a caveat: if we apply Davidson's method to a diagonal matrix, it then stagnates. However, the method is not restricted to the use of the diagonal preconditioner, and a different preconditioner can be used instead [217].

2.2 Quantum information

In the past few years, there has been an increasingly active exchange of ideas and methods between the formerly somewhat mutually insulated fields of quantum information and many-body physics. This has been due, on the one hand, to the growing sophistication of methods and the increasing complexity of problems treated in quantum information theory, and, on the other, to the recognition

that a number of central issues in many-body quantum systems can fruitfully be approached from the quantum information point of view [218, 219].

The central concept is the entanglement. Entanglement describes a correlation between quantum mechanical systems, such as spins and electrons, that does not occur in classical physics [220–223]. A recent experiment pointed out that entanglement effects are also relevant on the macroscopic scale [224]. Therefore, not only is the energy spectrum of a system important, but it is also important to investigate quantities such the entanglement. A small amount of entanglement can produce significant effects in the macroscopic world. The role of entanglement has been shown to be fundamental at a phase transition [225].

Unfortunately, a unique definition of entanglement does not exist [226–228] and many criteria have been proposed to distinguish separable states and entangled states [229, 230], such as the Schmidt rank or the von Neuman entropy [231]. In the next section, we describe the density-matrix formalism as the basic description of the system, and, using its properties, define the von Neumann entropy, which we use as the measure of the entanglement.

2.2.1 The density matrix

To describe a phenomenon correctly and conveniently, we have to parameterize the states of a physical system with a familiar and consistent basis set [232–236], i.e., spin orientation, total angular spin, or number of particles. However, the *real* state of the system is usually a superposition of these.

States of maximal information are often called *pure states* or simple states. A pure state is characterized by the existence of an experiment that gives a certain predictable outcome when the experiment is performed on the system in that state and in that state only. However, quantum systems for which the information is less than maximal also occur. These states are called *mixed states* because they can be described by the incoherent superposition of pure states. The description of mixed states as a mixture of pure states is not unique.

In the ordinary formalism of quantum mechanics, a pure state can be expanded in terms of a set of eigenvectors $|n\rangle$

$$|\Psi_{pure}\rangle = \sum_n |n\rangle\langle n|\Psi_{pure}\rangle = \sum_n c_n|n\rangle \, ,$$

where $c_n = \langle n|\Psi_{pure}\rangle$. For a system in this state, the expectation value of an operator O can be calculated as

$$\langle O\rangle = \sum_{nn'} O_{nn'}c_n^* c_{n'} \, ,$$

where $O_{nn'} = \langle n|O|n'\rangle$. On the other hand, for a mixed states with weights $p^{(i)}$, the mean value of O is given by the grand average

$$\langle O \rangle = \sum_i p^{(i)} \langle O \rangle_i = \sum_{nn'} O_{nn'} \sum_i p^{(i)} c_n^{*(i)} c_{n'}^{(i)} \,.$$

Therefore, defining the density matrix

$$\rho_{n'n} = \sum_i p^{(i)} c_n^{*(i)} c_{n'}^{(i)} \,,$$

we can express the mean value of an observable as

$$\langle O \rangle = \sum_{nn'} O_{nn'} \rho_{n'n} = \sum_n [O\rho]_{nn} = \mathrm{Tr}\,(O\rho)\,.$$

The density matrix represents the minimum set of input data which is needed to calculate the mean value of any operator for a system prepared in a given way. The density matrix elements have the following properties and restrictions:

1. Since $\langle O \rangle$ is real for every Hermitian operator O, ρ also has to be Hermitian,

$$\rho_{n'n} = \rho_{nn'}^{*}\,.$$

2. The trace of a density matrix is unity because the mean value of the identity operator is also unity,

$$\mathrm{Tr}\,\left(\hat{1}\rho\right) = \mathrm{Tr}\,(\rho) = \sum_n \rho_{nn} = 1\,.$$

3. The density matrix has to be positively definite, i.e., in every representation or basis

$$\rho_{nn} \geq 0\,.$$

4. Since the density matrix is Hermitian can be diagonalized by a unitary matrix U,

$$\rho_j \delta_{jj'} = \sum_{nn'} U_{jn} \rho_{nn'} U_{n'j'}^{-1}\,,$$

$$\mathrm{Tr}\,\left(\rho^2\right) = \sum_j \rho_j^2 \leq \left(\sum_j \rho_j\right)^2 = [\mathrm{Tr}\,(\rho)]^2 = 1\,.$$

Indeed, a pure state is characterized by $\rho^2 = \rho$, and is represented by a density matrix with one eigenvalue equal to one and all others equal to zero. Therefore, ρ^2 expresses the mixing [237].

Let us consider the state of two interacting systems a and b represented by the density matrix ρ^{ab}. An operator acting on system a can be treated as an operator of the whole system, and we have

$$\langle O^a \rangle = \mathrm{Tr}_{ab}\left[\left(O^a \otimes 1^b\right) \rho^{ab}\right] = \mathrm{Tr}_a\left(O^a \rho^a\right),$$

where $\rho^a = \mathrm{Tr}_b\left(\rho^{ab}\right)$ represents the information on alone a contained in ρ^{ab}. The states of the two systems are uncorrelated when

$$\langle O^a O^b \rangle = \langle O^a \rangle \langle O^b \rangle$$

for all pairs $O^a O^b$. This requires that the total density matrix be a product,

$$\rho^{ab} = \rho^a \otimes \rho^b.$$

Given a density matrix of dimension N, pure states of the system $\mathrm{Tr}(\rho^2) = 1$ contain maximum information, and states with $\mathrm{Tr}(\rho^2) = N^{-1}$ instead contain the minimum. This is because the statistical fluctuations of a physical quantity, represented by $\langle O^2 \rangle - \langle O \rangle^2$, tend to increase as $\mathrm{Tr}(\rho^2)$ decreases from one to N^{-1}. Thus, the quantity $\sum_i \rho_i^2 = \mathrm{Tr}\left(\rho^2\right) = \langle \rho \rangle \leq 1$ can be used as a measure of information as well. However, information theory [238, 239] implies that the total quantity of information of a set of uncorrelated systems is the sum of the quantity of information of the single ones. Since the density matrix ρ^{ab} of two uncorrelated systems is the product of the density matrices ρ^a and ρ^b of the two systems, we then have

$$\langle \rho^{ab} \rangle = \mathrm{Tr}_{ab}\left[\left(\rho^{ab}\right)^2\right] = \left[\mathrm{Tr}_a\left(\rho^a\right)\right]^2 \left[\mathrm{Tr}_b\left(\rho^b\right)\right]^2.$$

Thus, $\ln\langle \rho \rangle = \ln\mathrm{Tr}\left(\rho^2\right)$ is additive and corresponds to the concept of information better than $\langle \rho \rangle = \mathrm{Tr}\left(\rho^2\right)$ itself.

Nevertheless, in statistical mechanics the entropy of a system coincides with the mean value $S(\rho) = -k\langle \ln \rho \rangle$, where k is the Boltzmann constant [240–242]. This suggests that one uses $\langle \ln \rho \rangle = \mathrm{Tr}\left(\rho \ln \rho\right)$, or, still better, $\langle \ln N\rho \rangle = \mathrm{Tr}\left(\rho \ln N\rho\right)$, as the suitable definition of the quantity of information. This definition allows one to introduce a *quantity of information operator* $\ln(N\rho)$, which has the additivity property

$$\ln(N_{ab}\rho^{ab}) = \ln(N_b\rho^a) + \ln(N_b\rho^b)$$

whenever the states of a and b are uncorrelated, or not entangled. Notice that $\langle \ln \rho \rangle$ and $\langle \rho \rangle$ vary between the same limits and that their values are never very different [233].

Possible measures of entanglement are the Schmidt number and the single-copy entanglement. The Schmidt number N corresponds to the number of density matrix eigenvalues different from zero. Since states with zero weight do not contribute to the description of the state, the number corresponds to the dimension of the density matrix. This quantity can better characterize the entanglement of a finite system [243, 244]. The single-copy entanglement is obtained from the highest eigenvalue of the density matrix ω_0, $E = -\ln \omega_0$. Since the trace of the density matrix is invariant and equal to unity, we clearly obtain information about the entanglement from the highest eigenvalue. Moreover, for a critical system, this quantity takes on exactly half the value of the entropy [245, 246].

2.2.2 The von Neuman entropy

A correct definition of entropy is possible only in the framework of quantum mechanics [232, 236, 237, 247]. Entropy can be interpreted as a measure of the amount of mixing in a mixed quantum states or as the lack of information about the system. Since statements in statistical mechanics are true only in the thermodynamic limit, we expect properties such as ergodicity, mixing, or stability [248] to hold strictly only in the thermodynamic limit [249].

The von Neumann entropy of a quantum system described by a density matrix ρ is defined as

$$S(\rho) = -\mathrm{Tr}\left(\rho \ln \rho\right) .$$

We consider the relation between the entropies of two subsystems and show one of the most important results in the quantum theory of correlation, the Araki-Lieb inequality [250]. Let ρ^a and ρ^b be the reduced density matrices of subsystem a and b, respectively, and let ρ^{ab} be the density matrix of a composite system; then

$$S(\rho^a) + S(\rho^b) \geq S(\rho^{ab}) \geq |S(\rho^a) - S(\rho^b)| . \tag{2.9}$$

Physically, the left-hand side implies that we have more information in an entangled state than if the two states are treated separately. Considering the two systems separately, we neglect the entanglement and therefore lose information. An interesting result can be obtained considering the composite system to be in a pure state; then $S(\rho^{ab}) = 0$, and it follows from the right hand side of Eq.(2.9) that $S(\rho^a) = S(\rho^b)$.

Two important properties of the entropy are [237] additivity,

$$S(\rho^a \otimes \rho^b) = S(\rho^a) + S(\rho^b) ,$$

i.e., for two independent systems the entropies add up, and, concavity,

$$S\left(\sum_i \lambda_i \rho^i\right) \geq \sum_i \lambda_i S(\rho^i) ,$$

which reflects the fact that mixing increases uncertainty.

Now we define the von Neumann mutual information, which refers to the correlation between the different partitions of a system. This quantity is particularly useful in quantum chemistry DMRG [251–261]. The von Neumann mutual information between two subsystems ρ^a and ρ^b of a joint system described by ρ^{ab} is defined as

$$I(\rho^a : \rho^b; \rho^{ab}) = S(\rho^a) + S(\rho^b) - S(\rho^{ab}) \,.$$

This quantity can be interpreted as a distance between two quantum states [262–265].

Defining the von Neumann relative entropy between two states σ and ρ as

$$S(\sigma \| \rho) = \mathrm{Tr}\left[\sigma \left(\ln \sigma - \ln \rho\right)\right] \,,$$

we can show that (after some algebra)

$$I(\rho^a : \rho^b; \rho^{ab}) = S(\rho^{ab} \| \rho^a \otimes \rho^b) \,.$$

Therefore, the von Neumann mutual information can be understood as the distance in the Hilbert space between the state ρ^{ab} and the uncorrelated state $\rho^a \otimes \rho^b$. Furthermore, if we consider the entire system to be in a pure state, then the expression reduces to $I(\rho^a : \rho^b; \rho^{ab}) = 2S(\rho^a) = 2S(\rho^b)$.

Another key result in quantum information theory is the Holevo bound [266]. A quantum communication channel consists of N prepared states $\rho_1, \ldots, \rho_N$, encoding a message according to probabilities $p_1, \ldots, p_N$. If we perform a set of measurements to determine the correct sequence of states and probabilities, then the accessible information is given by the mutual information between the measurements and $\rho_1, \ldots, \rho_N$, and is bounded,

$$S\left(\sum_i p_i \rho_i\right) - \sum_i p_i S(\rho_i) \geq \max_E I(E : \rho) \,,$$

where E is the set of measurements.

The von Neumann entropy has been found to be intimately connected to many-body properties of a quantum system such as the quantum criticality. In one dimension, $S(N)$ will increase logarithmically with N if the system is quantum critical, but will saturate with N if the system is not [267, 268]. If a quantum critical system is also conformally invariant, additional, specific statements can be made about the entropy [186]. In higher dimensions, the von Neumann entropy will be bounded from below by a number proportional to the area (or length or volume, as appropriate) of the interface between the two parts of the system [184].

2.3 The DMRG method

In the first section, we have seen how big system sizes cannot be treated by exact diagonalization. The basis of the Hilbert space becomes exponentially large; therefore a method to systematically reduce the size of the basis is required. An approach to do this for the Kondo problem, the numerical renormalization group method (NRG), was develop by Wilson [269, 270]. The Wilson procedure consists of the following [271]: first, we start with a finite system that we can diagonalize (completely). Second, we keep the m lowest energy eigenstates. Third, we add a new site, and we iterate, keeping constant the number of states. The procedure works excellently for a large class of quantum impurity models [168, 171, 272–277].

However, the limitations of applying the method to quantum lattice models became clear soon after its invention, and a generalization of the method was required [278]. The origin of the difficulties was pointed out some time later, in terms of a simple noninteracting problem. The failure of the NRG could be related to the effect of boundary conditions on the way the blocks are combined [279]. A workable method for many-body systems was developed only a few years later, when S. R. White discovered the optimal way to truncate the basis using the block density matrix [46].

The DMRG algorithm can be explained in terms of a few important ingredients. The first is to consider a bipartite system, where Schmidt decomposition is known to hold, and to use a truncation scheme based on the density-matrix eigenvalues. The second is to build up the system starting from a small one by adding sites to the center of the chain until we reach the system size needed (warm-up). Finally, using the block representations obtained in the warm-up, we converge to the ground state by sweeping forward and backward, adding two new sites on the middle at every step to regenerate previously missed states.

2.3.1 The density matrix projection

Consider a finite many-body system in a pure state $|\Phi_0\rangle$. In practice, such a state is obtained from an iterative diagonalization of the Hamiltonian of the system. Now, we consider the system to be divided into two parts, A and B. In general, the parts cannot be represented using a wave function, but only using the density matrix representation [232, 234, 235]. Therefore, the two subsystems are characterized by intrinsic mixing that limits the separability of the state of the system into the basis of the two subsystems [229, 230]. Our aim is to truncate the basis to the relevant part and to eliminate the rest of the basis. Let us call $|\tilde{\Phi}_0\rangle$ the new, approximate representation of the original state $|\Phi_0\rangle$. We want to minimize the error ε_{TE}

$$\varepsilon_{TE} = \left| |\Phi_0\rangle - |\tilde{\Phi}_0\rangle \right|^2$$

by selecting m appropriate states in the A block. Given a basis $\{|i\rangle\}$ for the block A and a basis $\{|j\rangle\}$ for the block B, we can represent $|\Phi_0\rangle$ as

$$|\Phi_0\rangle = \sum_{i,j} \phi_{ij} |i\rangle |j\rangle \,.$$

Note that the bases $\{|i\rangle\}$ and $\{|j\rangle\}$ do not necessarily have to be complete, but must span the space that contains $|\Phi_0\rangle$. The new basis states are formed by m relevant elements, $\{|\xi\rangle\}_{\xi=1}^m$, and they can be expressed the previous basis $\{|i\rangle\}$ and can be taken to be orthonormal, so that

$$|\xi\rangle = \sum_i u_i^\xi |i\rangle, \qquad \langle \xi|\xi'\rangle = \sum_i u_i^{\xi*} u_i^{\xi'} = \delta_{\xi\xi'}. \qquad (2.10)$$

The approximation to $|\Phi_0\rangle$ can be expressed in terms of these states,

$$|\tilde{\Phi}_0\rangle = \sum_{\xi j} \tilde{\phi}_{\xi j} |\xi\rangle |j\rangle \,.$$

The (truncation) error then becomes

$$\varepsilon_{TE} = \sum_{ij} \left(\phi_{ij} - \sum_\xi \tilde{\phi}_{\xi j} u_i^\xi \right)^2 \,.$$

The truncation error must be minimized over the parameters under the orthogonalization condition, Eq.(2.10). In order to do this, we introduce the Lagrange multipliers $\mu_{\xi\xi'}$ and solve

$$\frac{\partial \epsilon_{TE}}{\partial u_i^\xi} = \frac{\partial \epsilon_{TE}}{\partial \tilde{\phi}_{\xi j}} = \frac{\partial \epsilon_{TE}}{\partial \mu_{\xi\xi'}} = 0 \,.$$

After introducing the density matrix $\boldsymbol{\rho}$ of A with matrix elements

$$\rho_{ii'} = \sum_j \phi_{ij}^* \phi_{i'j}$$

and carrying out some algebra, we obtain the expressions

$$\tilde{\phi}_{\xi j} = \sum_i \phi_{ij} u_i^\xi, \quad \mu_{\xi\xi'} = 0,$$

and the equation

$$\sum_{i'} \rho_{ii'} u_i^\xi - \sum_{i'i''\xi'} u_i^{\xi'} u_{i'}^{\xi'*} \rho_{i'i''} u_{i''}^\xi = 0 \,.$$

In vector notation, this equation can be rewritten

$$\left[1 - \sum_{\xi'} \mathbf{u}^{\xi'} \left(\mathbf{u}^{\xi'} \right)^{\dagger} \right] \cdot \boldsymbol{\rho} \cdot \mathbf{u}^{\xi} = 0$$

This equation can be interpreted as a projector acting on the vector $\boldsymbol{\rho} \cdot \mathbf{u}^{\xi}$. The projector removes all the components of the vector along one of the vectors $\mathbf{u}^{\xi''}$ as

$$\left[1 - \sum_{\xi'} \mathbf{u}^{\xi'} \left(\mathbf{u}^{\xi'} \right)^{\dagger} \right] \cdot \mathbf{u}^{\xi''} = 0 \, .$$

We require that the basis spanned by $\{\mathbf{u}^{\xi}\}$ has to contain all vectors $\{\boldsymbol{\rho} \cdot \mathbf{u}^{\xi}\}$. Thus, a set of eigenvectors of $\boldsymbol{\rho}$ clearly satisfies this condition. We set $\{\mathbf{u}^{\xi}\}$ to be eigenvectors of $\boldsymbol{\rho}$ with eigenvalue λ^{ξ}. It follows that

$$\lambda^{\xi} = \mathbf{u}^{\xi\dagger} \cdot \boldsymbol{\rho} \cdot \mathbf{u}^{\xi} = \sum_{ii'j\xi} u_{i'}^{\xi*} \phi_{i'j}^{*} \phi_{ij} u_{i}^{\xi} = \sum_{j} \left| \sum_{i} \phi_{ij} u_{i}^{\xi} \right|^{2} \geq 0 \, .$$

Since the set of eigenvectors $\mathbf{u}^{\xi}$ is orthonormal and complete,

$$\sum_{\xi} \lambda^{\xi} = \sum_{ii'j} \phi_{i'j}^{*} \phi_{ij} \delta_{ii'} = \sum_{i} \rho_{ii} = \sum_{ij} \phi_{ij}^{2} = 1.$$

Finally, inserting u_{i}^{ξ} and $\tilde{\phi}_{\xi j}$ into the definition of the truncation error and selecting m vectors, we obtain

$$\varepsilon_{TE} = 1 - \sum_{\xi=1}^{m} \lambda^{\xi} \, .$$

We conclude that the eigenvectors $\mathbf{u}^{\xi}$ of $\boldsymbol{\rho}$ corresponding to the m largest eigenvalues λ^{ξ} are the optimal choice for the basis $\{|\xi\rangle\}_{\xi=1}^{m}$.

Originally, S. R. White arrived at similar conclusions [46,47] by considering the singular value decomposition (SVD) [280,281]. The SVD is used in sound and image signal compression [282] and its generalization to tensorial form could become the key to extending the DMRG to two- and three-dimensional systems. The relationship of the SVD to the DMRG is contained in the Schmidt decomposition [283]. The relevant basis states $\{|\bar{\xi}\rangle\}_{\xi=1}^{m}$ in B are given by

$$|\bar{\xi}\rangle = \sum_{j} v_{j}^{\xi} |j\rangle,$$

where the vectors $\mathbf{v}^{\xi}$ are related to the vectors $\mathbf{u}^{\xi}$ through the relations

$$v_{j}^{\xi} = \frac{1}{\sqrt{\lambda^{\xi}}} \sum_{i} \phi_{ij}^{*} u_{i}^{\xi*} \iff u_{j}^{\xi} = \frac{1}{\sqrt{\lambda^{\xi}}} \sum_{i} \phi_{ij} v_{i}^{\xi} \, .$$

These basis states are orthonormal and they are indeed the largest eigenvectors of the density matrix $\rho_{jj'}^B = \sum_i \phi_{ij}^* \phi_{ij'}$ as can be seen by evaluating

$$\sum_{j'} \rho_{jj'} v_{j'}^\xi = \frac{1}{\sqrt{\lambda^\xi}} \sum_{ii'j'} \phi_{ij}^* \phi_{ij'} \phi_{i'j'}^* \phi_{i'j'} u_{i'}^{\alpha*} = \sqrt{\lambda^\xi} \sum_i \phi_{ij}^* u_i^{\xi*} = \lambda^\xi v_j^\xi.$$

The ground state can be expressed in this basis as

$$|\Phi_0\rangle = \sum_{ij} \phi_{ij} |i\rangle |j\rangle = \sum_{\xi=1}^{m_s} \sqrt{\lambda_\xi} |\xi\rangle |\overline{\xi}\rangle.$$

This is the Schmidt decomposition. For every basis state $|\xi\rangle$ in A there is exactly one $|\overline{\xi}\rangle$ in B. The number m_S is the Schmidt dimension and can be at most the smaller of the dimension of A and B. The approximation for the ground state can be rewritten as $|\tilde{\Phi}_0\rangle = \sum_{\xi=1}^m \sqrt{\lambda^\xi} |\xi\rangle |\overline{\xi}\rangle$, where m is the number of states that are kept.

From the Schmidt decomposition, the two following conclusions can be reached: first, if the truncation error is zero, then the approximate wave vector has properties identical to the original one. Second, the set of quantum numbers contained in A determines the set of quantum numbers in B. Every vector $|\xi\rangle$ in A must have the correct quantum number so that the sum with the quantum number of $|\overline{\xi}\rangle$ in B forms the required quantum numbers of the wave function $|\Phi_0\rangle$.

Density matrix and quantum numbers The density matrix has the same block matrix structure as the block Hamiltonian. Suppose the system is in a pure state α with quantum number $\mathbf{Q}$. Dividing the system in two, we construct the state combining the two bases of the subsystems with the right quantum numbers, $\mathbf{Q} = q + \overline{q}$,

$$|\Psi_\alpha(\mathbf{Q})\rangle = \sum_{ij} c_{ij}^{q,\overline{q}}(0) |i, q\rangle |j, \overline{q}\rangle .$$

Let us calculate the identity operator

$$\hat{1} = |\Psi_\alpha(\mathbf{Q})\rangle \langle \Psi_\alpha(\mathbf{Q})| = \sum_{ij} \sum_{i'j'} c_{ij}^{q,\overline{q}}(\alpha) \left(c_{i'j'}^{q',\overline{q}'}(\alpha) \right)^* |i, q\rangle |j, \overline{q}\rangle \langle i', q'| \langle j', \overline{q}'|$$

and trace over the subsystem B in order to obtain the reduced density matrix for the subsystem A

$$\sum_{\tilde{j}} \langle \tilde{j}, \overline{\tilde{q}} | \cdots | \tilde{j}, \overline{\tilde{q}} \rangle = \sum_{\tilde{j}} \sum_{ij} \sum_{i'j'} c_{ij}^{q,\overline{q}}(\alpha) \left(c_{i'j'}^{q',\overline{q}'}(\alpha) \right)^* |i, q\rangle \langle i', q'| \langle \tilde{j}, \overline{\tilde{q}} | j, \overline{q} \rangle \langle j', \overline{q}' | \tilde{j}, \overline{\tilde{q}} \rangle$$

$$= \sum_{ii'} |i, q\rangle \langle i', \overline{q}| \sum_{\tilde{j}} c_{i\tilde{j}}^{q,\overline{q}}(\alpha) \left(c_{i'\tilde{j}}^{q,\overline{q}}(\alpha) \right)^* .$$

Therefore, the density matrix has the same block structure as the block Hamiltonian. For instance, the Heisenberg Hamiltonian of a two-site chain embedded in a four-site chain is

$$H = \frac{1}{4} \begin{pmatrix} 1 & 0 & 0 & 0 \\ 0 & -1 & 2 & 0 \\ 0 & 2 & -1 & 0 \\ 0 & 0 & 0 & 1 \end{pmatrix},$$

and its density matrix is

$$\rho = \frac{1}{12\sqrt{2+\sqrt{3}}} \begin{pmatrix} 1 & 0 & 0 & 0 \\ 0 & 11+6\sqrt{3} & -2(5+3\sqrt{3}) & 0 \\ 0 & -2(5+3\sqrt{3}) & 11+6\sqrt{3} & 0 \\ 0 & 0 & 0 & 1 \end{pmatrix}.$$

Using this property, we can easily obtain the single-site density matrix because states map one-to-one to quantum numbers.

Single-site density matrix For the spin-1/2 case, S^z_{tot} is conserved, and the single-site density matrix is of the form

$$\rho_{s=1/2} = \begin{pmatrix} \rho_{\uparrow\uparrow} & 0 \\ 0 & \rho_{\downarrow\downarrow} \end{pmatrix}$$

with $\rho_{\uparrow\uparrow} = \hat{s}_z \left(\hat{s}_z + 1 \right)/2$ and $\rho_{\downarrow\downarrow} = \hat{s}_z \left(\hat{s}_z - 1 \right)/2$. Thus, it is diagonal and it is required to measure only s_z and s_z^2.

The spin-one case, when total S_z is conserved, can also be reduced to a diagonal matrix

$$\rho_{s=1} = \begin{pmatrix} \rho_{11} & 0 & 0 \\ 0 & \rho_{00} & 0 \\ 0 & 0 & \rho_{-1-1} \end{pmatrix}$$

where $\rho_{11} = \hat{S}_z \left(\hat{S}_z + 1 \right)/2$, $\rho_{00} = 1 - \hat{S}_z^2$, and $\rho_{-1-1} = \hat{S}_z \left(\hat{S}_z - 1 \right)/2$.

For the single-site Hubbard basis, in a system that conserves $N^{\uparrow}$ and $N^{\downarrow}$, we obtain

$$\rho_{\mathrm{H}} = \begin{pmatrix} \rho_0 & 0 & 0 & 0 \\ 0 & \rho_{\uparrow} & 0 & 0 \\ 0 & 0 & \rho_{\downarrow} & 0 \\ 0 & 0 & 0 & \rho_{\downarrow\uparrow} \end{pmatrix},$$

where $\rho_0 = 1 - \hat{n}_{\downarrow} - \hat{n}_{\uparrow} + \hat{n}_{\downarrow}\hat{n}_{\uparrow}$, $\rho_{\uparrow} = 2\hat{s}_z^2 - \hat{s}_z$, $\rho_{\downarrow} = 2\hat{s}_z^2 + \hat{s}_z$, and $\rho_{\downarrow\uparrow} = \hat{n}_{\downarrow}\hat{n}_{\uparrow}$.

The multi-site density matrix can also be calculated, but multi-point correlation functions and different operators must be calculated [284–287]. For example, for
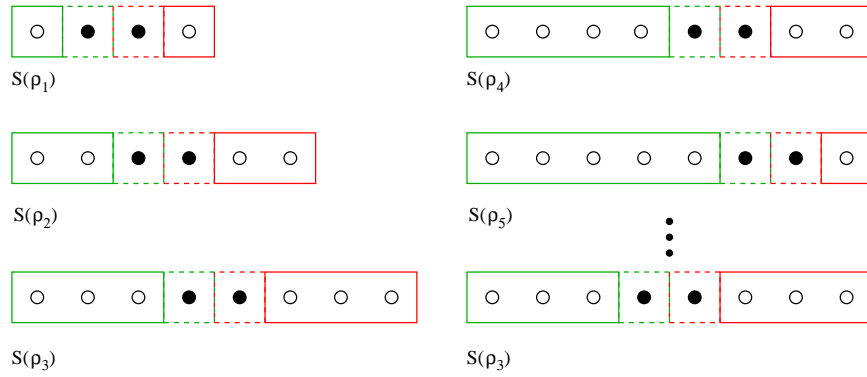
Figure 2.1: The infinite-system DMRG algorithm on the left and the finite-system DMRG on the right.

spinless fermions the two-site entropy reads

$$
\rho_F(\ell, m) = \begin{pmatrix} u^- & 0 & 0 & 0 \\ 0 & \omega & z & 0 \\ 0 & z^* & \omega & 0 \\ 0 & 0 & 0 & u^+ \end{pmatrix},
$$

where $u^- = 1 + \langle n_\ell n_m \rangle - \frac{3}{2}\langle n_\ell \rangle - \frac{1}{2}\langle n_m \rangle$, $u^+ = \langle n_\ell n_m \rangle + \frac{1}{2}\langle n_\ell \rangle - \frac{1}{2}\langle n_m \rangle$, $\omega = \frac{1}{2}\langle n_\ell \rangle + \frac{1}{2}\langle n_m \rangle - \langle n_\ell n_m \rangle$, and $z = \frac{1}{2}\langle c_\ell^\dagger c_m + c_m^\dagger c_\ell \rangle$. It easy to note that the two-site density matrix has the same block structure as the two-site block Hamiltonian.

The system block density matrix is a direct byproduct of the DMRG algorithm and the single-site and two-sites entropies can be easily implemented as measurements of observables. These and related entropies have been shown to be very important in studying quantum phase transitions, e.g., the two-site entropy can be used to characterize a transition to a dimerized phase [288].

2.3.2 The algorithm

Based on the previous ideas, we will first describe the infinite-system algorithm, and then go on to describe the finite-system algorithm.

The infinite system algorithm can be summarized as follows; see also Fig.(2.1).

1. Form a superblock S containing $\ell + \ell'$ sites which is small enough to be diagonalized. The basis can be written as the tensor product of a left part,

L, formed from the first ℓ sites and a right part, R, formed from the remaining ℓ' sites

$$|ij\rangle_{S(\ell+\ell')} = |i\rangle_{L(\ell)} \otimes |j\rangle_{R(\ell')} \qquad i = 1, \cdots, m_L;\ j = 1, \cdots, m_R.$$

Thus, the dimension of the entire Hilbert space is $m_S = m_L \times m_R$.

2. Using the Lanczos or the Davidson algorithm, diagonalize the superblock Hamiltonian, obtaining the ground states eigenvalue E_0 and eigenvector

$$|\Phi_0(\ell + \ell')\rangle = \sum_{ij} \phi_{ij}^{\ell+\ell'} |ij\rangle_{S(\ell+\ell')}.$$

3. Form the reduced density matrix ρ^L for the current system block from the ground state wavefunction, tracing out the right block

$$\rho_{ii'}^{L(\ell)} = \sum_{j} \phi_{ij}^{\ell+\ell'} \phi_{i'j}^{*\,\ell+\ell'}.$$

4. Diagonalize ρ^L completely to obtain all m_L eigenvalues and eigenvectors. Use the $m \leq m_L$ eigenvectors with largest eigenvalues as columns of the projector $\mathcal{P}_m^{\bar{L}(\ell)}$. Apply the projector that diagonalizes and truncates ρ^L to the largest m eigenvalues

$$|\tilde{i}\rangle_{\tilde{L}(\ell)} = \mathcal{P}_m^{L(\ell)} |i\rangle_{L(\ell)} \qquad \tilde{i} = 1, \cdots, m;\ i = 1, \cdots, m_L.$$

5. Transform all relevant operators represented in the old basis to the new reduced density matrix basis, $|\tilde{i}\rangle_{\tilde{L}(\ell)}$, including the block Hamiltonian

$$\tilde{H}^{L(\ell)}(m) = \left(\mathcal{P}_m^{L(\ell)}\right)^{\dagger} H^{L(\ell)}(m_L) \mathcal{P}_m^{L(\ell)}$$

and, similarly,

$$\tilde{A}^{L(\ell)}(m) = \left(\mathcal{P}_m^{L(\ell)}\right)^{\dagger} A^{L(\ell)}(m_L) \mathcal{P}_m^{L(\ell)},$$

where A is a generic operator inside the block.

6. Extend the left and right block by one site

$$|i\rangle_{L(\ell+1)} = |\tilde{i}\rangle_{\tilde{L}(\ell)} \otimes |s\rangle_1$$

$$|j\rangle_{R(\ell'+1)} = |s\rangle_1 \otimes |\tilde{j}\rangle_{R'(\ell')}$$

7. Form a superblock of size $L = \ell + \ell' + 2$, combining the bases

$$|ij\rangle_{S(\ell+\ell'+2)} = |i\rangle_{L(\ell+1)} \otimes |j\rangle_{R(\ell'+1)}$$

Thus, the action of the superblock Hamiltonian operator on a wave function $|\Phi\rangle$ can be represented as

$$\langle ij|\hat{H}^{S(\ell+\ell'+2)}|\Phi\rangle = \sum_{\alpha}\sum_{i'}\langle i|\hat{A}_{\alpha}^{L(\ell+1)}|i'\rangle \sum_{j'}\langle j|\hat{B}_{\alpha}^{R(\ell'+1)}|j'\rangle \varphi_{i'j'}\,,$$

where $\hat{A}_{\alpha}$ and $\hat{B}_{\alpha}$ are pairs of operator defined on the left and right block, respectively. For each α, this equation is equivalent to two matrix multiplications.

8. Repeat, starting at step 2.

The cycle continues until a given system size is reached, $L \sim 10^4$, 10^5. In principle, we are interested in results converged to the thermodynamic limit. This method has significant limitations. Good accuracy is obtained only very close to the center of the chain, and, for very large systems, a spurious correlation length appears [289–291]. However, the infinite-system algorithm can be used as the initial stage of the finite system algorithm.

The finite system algorithm proceeds as follows, see also Fig.(2.1):

1. Carry out the infinite system algorithm until the superblock reaches a particular size L, storing $H^{L(\ell)}$ and the operators needed to connect the block at each step.

2. Carry out steps 3-5 of the infinite system algorithm to obtain $H^{L(\ell+1)}$. Store it. (Now $\ell \neq \ell'$.)

3. Form a super block of size L using $H^{L(\ell+1)}$, two single sites and $H^{R(\ell'-1)}$ with $\ell' = L - \ell - 2$.

4. Repeat steps 2-3 until $\ell = L - 3$ (i.e. $\ell' = 1$). This is the left-to-right phase of the algorithm.

5. Carry out steps 3-5 of the infinite system algorithm, reversing the roles of $H^{L(\ell)}$ and $H^{R(\ell')}$; i.e., switch directions to build up the right block and obtain $H^{R(\ell'+1)}$ using the stored $H^{L(\ell)}$ as the environment. Store $H^{R(\ell'+1)}$.

6. Form a super block of size L using $H^{L(\ell-1)}$, two single sites, and $H^{R(\ell'+1)}$.

7. Repeat steps 5-6 until $\ell = 1$. This is the right-to-left phase of the algorithm.

8. Repeat, starting with step 2.

Modifications to this algorithm using different configurations, for example, the three-block system [292, 293], and tree lattices [294], have been also developed. Note that for a three-block configuration, the Schmidt decomposition is more complicated and is not always applicable [295].

Recently, a new scheme that is particularly efficient for PBC, has been proposed by White [296]. In the usual case, the system is divided into two blocks and, to each step, after projecting out unnecessary states, the two blocks are expanded by adding two new sites at each block. Two new sites must be added in order to facilitate convergence. In fact, after the truncation, the blocks can lack relevant quantum sectors and states, and the addition of an additional site can restore them. The original procedure becomes expensive for sites with many states or complex hopping. Therefore, White proposed to add only a single site instead of two, solving the problem of missed states by adding an explicit perturbation term into the density matrix. For the Heisenberg chain one adds

$$\Delta\rho = a \left(\hat{S}_\ell^+ \rho \hat{S}_\ell^- + \hat{S}_\ell^- \rho \hat{S}_\ell^+ + \hat{S}_\ell^z \rho \hat{S}_\ell^z \right) ,$$

where typically $a \sim 10^{-3} - 10^{-6}$, which is small enough to not affect the numerical precision. This term allows transitions between different quantum numbers explicitly. The approach is similar to the description of the evolution of the density matrix in the master equation, with the Lindblad operators acting on it [236, 297].

2.3.3 Measurements

A single-site operator, $\mathcal{O}_\ell$, such as the spin density or charge density on a site, with ℓ in the left block, can be calculated as

$$\langle \Phi_0 | \mathcal{O}_\ell | \Phi_0 \rangle = \sum_{ii';j} \phi_{ij}^* \langle i | \mathcal{O}_\ell | i' \rangle \phi_{i'j} = \sum_{ii'} \langle i | \mathcal{O}_\ell | i' \rangle \rho_{ii'} .$$

Alternatively, after having transformed the operator into the basis of eigenvectors of the density matrix, we can sum the product of the diagonal values of the operator and the corresponding eigenvalues of the density matrix.

For the expectation values of operators acting on different sites, $\mathcal{O}_\ell \mathcal{O}_m$, we have to consider two separate cases. When the two sites are on different blocks, then

$$\langle \Phi_0 | \mathcal{O}_\ell \mathcal{O}_m | \Phi_0 \rangle = \sum_{ii';jj'} \phi_{ij}^* \langle i | \mathcal{O}_\ell | i' \rangle \langle j | \mathcal{O}_m | j' \rangle \phi_{i'j'} .$$

When the two sites ℓ and m are on the same block we must use instead

$$\langle\Phi_0|\mathcal{O}_\ell\mathcal{O}_m|\Phi_0\rangle \;=\; \sum_{ii';jj'}\phi^*_{ij}\langle i|\mathcal{O}_\ell\mathcal{O}_m|i'\rangle\phi_{i'j} \tag{2.11}$$

$$\neq\; \sum_{ii';jj'}\sum_{i''}\phi^*_{ij}\langle i|\mathcal{O}_\ell|i''\rangle\langle i''|\mathcal{O}_m|i'\rangle\phi_{i'j}\,, \tag{2.12}$$

where $\langle i|\mathcal{O}_\ell\mathcal{O}_m|i'\rangle$ is calculated as a single operator, because the basis $\{|i''\rangle\}$ is incomplete due to the truncation process. Since during the DMRG iterations ℓ and m can be either on the same block or on different ones, we have to keep track of all $\mathcal{O}_\ell\mathcal{O}_m$, $\mathcal{O}_\ell$ and $\mathcal{O}_m$ operators.

2.3.4 Wave-function transformation

In order to speed up the diagonalization process, a good starting wave vector is necessary. Since different approximations to the same finite system are made at each step of the finite system algorithm, an obvious starting point is the result $\Phi_0^{L(\ell)}$ of the previous system step. However, this wave function is not in an appropriate basis for H^S because it is formed using different superblock configurations. In order to use the wave function $\Phi_0^{L(\ell)}$ obtained in the previous step ℓ as input for the next step $\ell+1$, we must first transform the wave function into the new basis.

At step ℓ, the superblock basis is given by

$$|i^{L(1,\ell)}s_{\ell+1}s_{\ell+2}j^{R(\ell+3,L)}\rangle = |i^{L(1,\ell)}\rangle\otimes|s_{\ell+1}\rangle\otimes|s_{\ell+2}\rangle\otimes|j^{R(\ell+3,L)}\rangle\,,$$

where $|i^{L(1,\ell)}\rangle$ is the basis of the left block containing the sites $1,\ldots,\ell$, $|s_{\ell+1}\rangle$, $|s_{\ell+2}\rangle$ are the single-site bases for the sites at positions $\ell+1$ and $\ell+2$, and $|j^{R(\ell+3,L)}\rangle$ is the basis for the right block formed by sites $\ell+3,\ldots,L$.

Assuming the algorithm builds up the system block from left to right, these states must be transformed to the configuration of the superblock at the next step

$$|i^{L(1,\ell+1)}s_{\ell+2}s_{\ell+3}j^{R(\ell+4,L)}\rangle\,.$$

This transformation can be broken up into two steps. The left block is transformed from the original product basis, $|i^{L(1,\ell)}s_{\ell+1}\rangle$ to the truncated basis of the density matrix

$$|i^{L(1,\ell+1)}\rangle = \sum_{s_{\ell+1},i_\ell}L^{\ell+1}[s_{\ell+1}]_{i_{\ell+1},i_\ell}|i^{L(1,\ell)}\rangle\otimes|s_{\ell+1}\rangle,$$

where the transformation matrix $L^{\ell+1}[s_{\ell+1}]_{i_{\ell+1},i_\ell}$ contains the density-matrix eigenvectors. Similarly, for the right basis one defines

$$|j^{R(\ell+3,L)}\rangle = \sum_{s_{\ell+3},j_{\ell+4}}R^{\ell+3}[s_{\ell+3}]_{j_{\ell+3},j_{\ell+4}}|s_{\ell+3}\rangle\otimes|j^{R(\ell+4)}\rangle\,.$$

Transformations similar to these were introduced for the first time in the context of the matrix-product-state picture [298].

To perform the wave function transformation, we expand the superblock wavefunction as

$$|\Phi\rangle = \sum_{i_\ell s_{\ell+1} s_{\ell+2} i_{\ell+3}} \phi(i_\ell, s_{\ell+1}, s_{\ell+2}, j_{\ell+3})|i_\ell, s_{\ell+1}, s_{\ell+2}, j_{\ell+3}\rangle$$

by inserting the quasi-identity $\sum_{i_{\ell+1}} |i_{\ell+1}\rangle\langle i_{\ell+1}| \approx 1$.

The coefficients of the wave function in the new basis can be calculated in two steps, first forming the intermediate states

$$\phi(i_{\ell+1}, s_{\ell+2}, j_{\ell+3}) = \sum_{i_\ell s_{\ell+1}} L^{\ell+1}[s_{\ell+1}]_{i_{\ell+1},i_\ell}\phi(i_\ell, s_{\ell+1}, s_{\ell+2}, j_{\ell+3})$$

and then forming

$$\phi(i_{\ell+1}, s_{\ell+2}, s_{\ell+3}, j_{\ell+4}) = \sum_{j_{\ell+3}} \phi(i_{\ell+1}, s_{\ell+2}, j_{\ell+3})R^{\ell+3}[s_{\ell+3}]_{j_{\ell+3},j_{\ell+4}} \, .$$

An analogous transformation with the roles of L and R reversed is used for a step in the right-to-left direction.

2.3.5 Accuracy and truncation errors

The reduction of the Hilbert space carried out in the DMRG method is closely related to the problem of quantum data compression [299, 300]. In quantum data compression, the Hilbert space of the system Λ is divided into two parts: the "typical subspace" Λ_{typ}, which is retained, and the "atypical subspace" Λ_{atyp}, which is discarded. For pure states, there is a well defined relationship between Λ_{typ} and the von Neumann entropy s of the corresponding ensemble. In general, it has been shown that

$$\beta \equiv \ln (\dim \Lambda_{typ}) - s \, , \tag{2.13}$$

is independent of the system size for large enough systems [243, 244].

Since one fundamentally treats a bipartite system in the DMRG, each subsystem is, in general, in a mixed state. In the context of the DMRG, the accessible information [266, 301] of mixed-state ensembles can be interpreted as the information loss due to the truncation procedure. This information loss is a better measure of the error than the discarded weight of the reduced density matrix

$$\varepsilon_{\mathrm{TE}} = 1 - \sum_{\alpha=1}^{m} w_\alpha \, , \tag{2.14}$$

(also called the truncation error). Here the w_α are the eigenvalues of the reduced density matrix ρ of either subsystem; both must have the same nonzero eigenvalue spectrum.

Based on these considerations, the convergence of the DMRG can be improved significantly by selecting the states kept using a criterion related to the accessible information. In general, the accessible information must be less than the Holevo bound [266]

$$I \leq s(\rho) - p_\mathrm{typ} s(\rho_\mathrm{typ}) - (1 - p_\mathrm{typ}) \, s(\rho_\mathrm{atyp}) \,, \qquad (2.15)$$

where ρ_typ or ρ_atyp are the portions of the density matrix formed from the basis states that are kept and discarded, respectively. The probability p_typ is chosen to be appropriate for the corresponding binary channel. The behavior of the mutual information for particular ensembles as a function of p_typ, including various bounds on the mutual information can be found in Ref. [301]. For the DMRG, the atypical subspace should contain as little information as possible if the approximation is to be accurate. Assuming that this is the case, we take $p_\mathrm{typ} = 1$, and the number of block states are selected so that $s(\rho) - s(\rho_\mathrm{typ}) \leq \chi$. This *a priori*-defined χ satisfies a well-defined entropy sum rule which is related to the total quantum information generated by the DMRG. Deviations from this sum rule provide a measure of the error of the DMRG calculation. Therefore, χ can be chosen to control its accuracy. Fig. 2.2 shows the relative error of the ground state energy, defined as
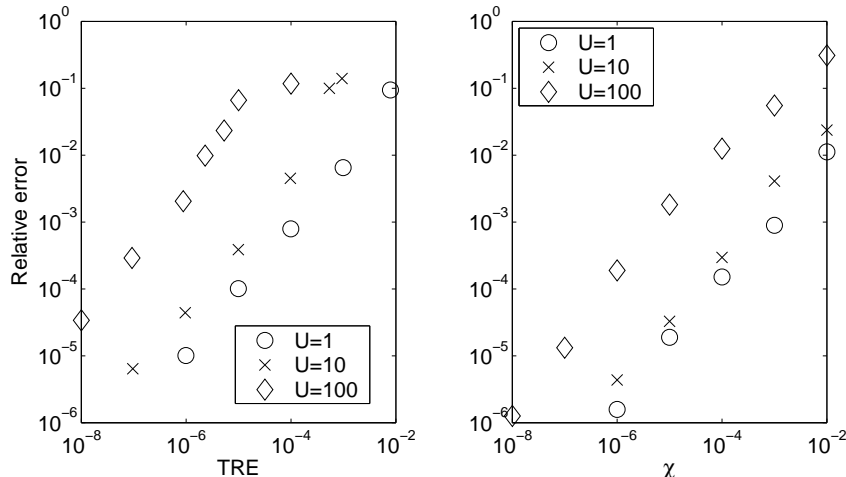

Figure 2.2: The relative error of the ground state energy for the half-filled Hubbard chain for various values of the on-site Coulomb interaction U on an $N = 80$-site lattice with periodic boundary conditions as a function of (a) the truncation error and (b) the threshold value of Holevo's bound on accessible information, Eq. (2.15). After Legeza [260].

$(E_{\mathrm{DMRG}} - E_{\mathrm{exact}})/E_{\mathrm{exact}}$, plotted on a logarithmic scale for various values of the Coulomb interaction U for the one-dimensional Hubbard model. In Fig. 2.2(a), it is plotted as a function of $\varepsilon_{\mathrm{TE}}$, whereas in Fig. 2.2(b), it is plotted as a function of χ. As can be seen, the error in the latter plot behaves very stably as a function of χ, even for very small values of the retained eigenvalues of ρ_{typ}. On the other hand, the error in the energy behaves somewhat less regularly as a function of $\varepsilon_{\mathrm{TE}}$. Therefore, an extrapolation of the energy as a function of χ would be significantly better behaved than one as a function of $\varepsilon_{\mathrm{TE}}$. We find that such behavior is representative; generically, extrapolation with χ is as stable or more stable than extrapolation with $\varepsilon_{\mathrm{TE}}$ for a wide variety of systems [244].

2.3.6 DMRG and entropy sum rule

In the DMRG procedure, when we add a site to the left block of size ℓ the entropy changes as

$$S_L(\ell) + S_{i+1} + I_L(\ell) = S_L(\ell + 1)$$

where $I_L(\ell)$ is the mutual information that quantifies the correlation between the subsystem and the new site added [244]. A similar equation holds for the right block

$$S_R(r) + S_{i+2} + I_R(r) = S_R(r + 1)\,.$$

Since we apply only unitary operations to each basis block, we cannot increase the entanglement between the left and right block. Thus, the amount of information generated by a forward renormalization step can be measured as

$$I_L(\ell) = S_L(\ell + 1) - S_L(\ell) - S_{\ell+1}\,,$$

where ℓ runs from 1 to $N - 1$. The information generated by the backward sweep is analogous. The total information gain of a full half sweep can be calculated as $\sum_{\ell=1}^{N} I_L(\ell)$. It is easy to show that, if no truncation is applied, the sum rule

$$\sum_{\ell=1}^{N-1} I_L(\ell) = -\sum_{\ell=1}^{N} S_\ell\,,$$

holds, where we have set $S_L(1) = S_1$ and $S_L(N) = 0$.

However, this equality does not hold in the DMRG calculation. In fact, during the DMRG process $S_L(\ell+1)$ is reduced to $S_L^{\mathrm{Trunc}}(\ell+1)$. Once the DMRG converges, the following equality holds:

$$\sum_{\ell=1}^{N-1} I_L(\ell) \approx -\sum_{\ell=1}^{N} S_\ell + \sum_{\ell=2}^{N} \left[S_L(\ell) - S_L^{\mathrm{Trunc}}(\ell) \right]\,.$$

Therefore, the following equation can be used as an alternative check of the convergence

$$\sum_{\ell=1}^{N-1} I_L(\ell) + \sum_{\ell=1}^{N} S_\ell < (N-1)\varepsilon \,.$$

Practically, an effective system of length $N+2$ is formed by adding two noninteracting sites to the ends of the chain. Therefore, all the blocks from size 1 to N can be generated.

2.4 Remarks

In this chapter, we have presented an introduction to the DMRG algorithm and have discussed a few notions of quantum information [302]. Following the motto *Programming is Understanding* [303] we dedicated part of the initial time to implement a new C++ DMRG code for spin-one chains. Therefore, it is natural that we have summarized some of the technical details here [304]. A good implementation of the algorithm requires an optimal bookkeeping of states and an efficient use of the appropriate iterative method to diagonalize matrices.

Concepts coming from quantum information theory are necessary to understand how quantum objects relate [43, 305].

For one-dimensional models, the DMRG algorithm has become a state-of-art tool. The results obtained with the DMRG achieve a formidable accuracy. The deep connection with quantum information, and the possibility to extend the method to dynamical processes, time-evoluting problems, and to systems at $T \neq 0$ makes the DMRG unique [306]. However, despite the great success, careful finite-size scaling studies continue to be vital to make any conclusion about behavior in the thermodynamic limit [289, 307].

3 Band-Mott insulator transition

The discovery of the neutral-ionic transition in charge-transfer complex [22] has led to a fruitful field to investigate. Charge-transfer complexes are formed by stack of π-electron donor (D), usually DMTTF molecules, and acceptor (A), CA molecules; see Fig. 3.1. The neutral phase corresponds to uniform and neutral distribution of charge, $D^0 A^0 D^0 A^0$, and the ionic phase to an alternation of positive and negative charges, $D^+ A^- D^+ A^-$. The ionic Hubbard model (IHM) is a simple description of this phenomena that can be treated in a controlled way. The model is obtained by extending the Hubbard model [308] with an alternating ionic potential; the potential simulates the effects of the alternate charge distribution on the molecules that electrons feel.

The ionic Hubbard model is also of interest in the context of a completely different material: the ferroelectric perovskites [309]. These systems show an enhancement of the electron-lattice interactions that may be due to purely strong correlation effects [310]. Therefore, these phenomena represent a new class of systems that spontaneously dimerize with a mechanism that is not the Peierls one. Recently [311], the neutral-ionic transition has been measured in organic charge-transfer complex close to zero temperature, $T = 0$, motivating the interest in it as a pure quantum phase transition.

3.1 Ionic Hubbard model

The Hamiltonian of the ionic Hubbard model can be grouped into three terms, a one-dimensional nearest-neighbor hopping term with matrix element t, an on-site Coulomb repulsion of strength U, and an ionic alternating potential of depth Δ,

$$\hat{H} = \hat{H}_{\text{hopping}} + \hat{H}_{\text{Coulomb}} + \hat{H}_{\text{ionic}} \,, \tag{3.1}$$

with

$$\hat{H}_{\text{hopping}} = t \sum_{i=1,\sigma}^{L-1} \hat{c}_{i\sigma}^{\dagger} \hat{c}_{i+1\sigma} + \hat{c}_{i+1\sigma}^{\dagger} \hat{c}_{i\sigma} \,, \tag{3.2}$$

$$\hat{H}_{\text{Coulomb}} = \frac{U}{2} \sum_{i=1,\sigma}^{L} \hat{n}_{i\sigma} \hat{n}_{i-\sigma} \,, \tag{3.3}$$
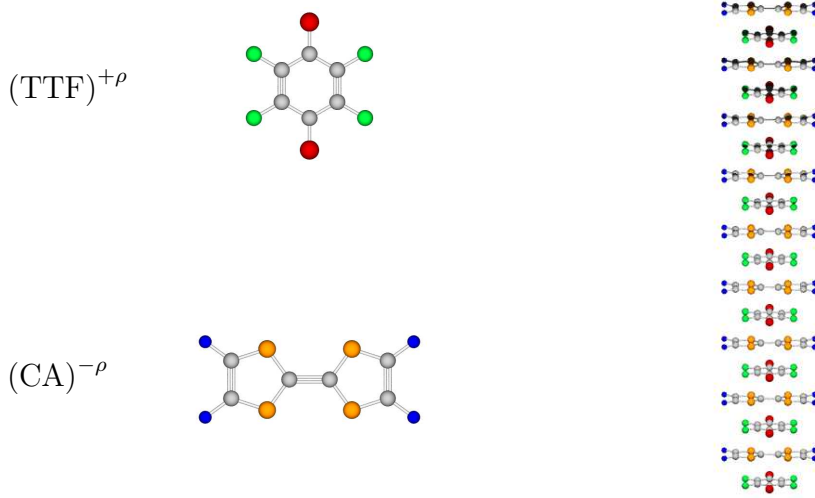
Figure 3.1: The TTF and chloranil QCl_4 are planar π electron donor and acceptor molecules. The charge-transfer complex is formed by stacks of these molecules: $D^{+\rho}A^{-\rho}D^{+\rho}A^{-\rho}D^{+\rho}A^{-\rho}$, where ρ is the ionicity.

and

$$\hat{H}_{\text{ionic}} = \frac{\Delta}{2} \sum_{i=1,\sigma}^{L} (-1)^i \, \hat{n}_{i,\sigma} \, . \tag{3.4}$$

Here $\hat{c}_{i\sigma}^\dagger$ ($\hat{c}_{i\sigma}$) are the usual creation (annihilation) operators on site i for an electron of spin σ and $\hat{n}_{i\sigma} = \hat{c}_{i\sigma}^\dagger \, \hat{c}_{i\sigma}$. Although the overall physics described by this model is now fairly well known, many details of the transition are still unclear.

3.1.1 Atomic limit

Let us examine what happens in the atomic limit, $t = 0$, which can be easily treated. For $U > \Delta$ and at half filling, there is no double occupancy in the ground state, which consists of a series of singly occupied sites with energy $\pm\Delta/2$ so that the entire system has energy $E = 0$. For $U < \Delta$, double occupancy is favorable, and the ground state consists of doubly occupied sites at energy $U - \Delta$ alternating with empty sites so that the energy of the system is $L(U - \Delta)/2$. At $(U - \Delta) \to 0$, a level crossing of two configurations occurs so that the transition must be first-order.
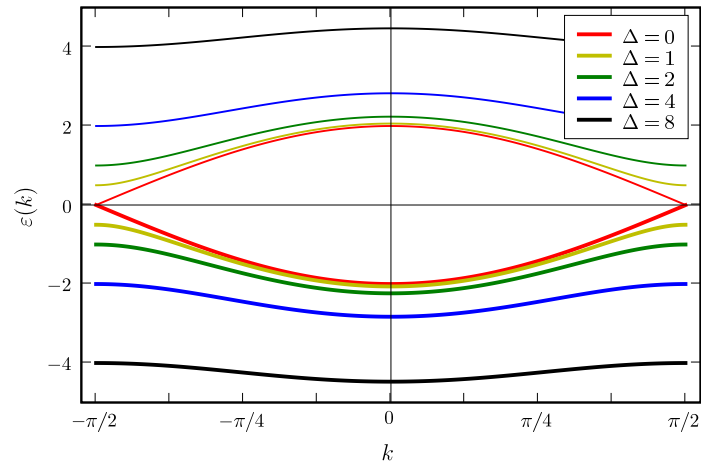
Figure 3.2: The band structure of the $t-\Delta$ model showing the two-band structure. A band gap opens linearly, $\Delta_{c,s} = \Delta$, near the Fermi level, at $k = \pm\pi/2$. For $\Delta = 0$, the same spectrum is obtained as that of the tight-binding model, but the Brillouin zone is halved and folded into itself.

3.1.2 Non-interacting limit

In the non-interacting limit, $U = 0$, the two band Hamiltonian is diagonal in k-space. Considering the lattice formed by two sub-lattices, we can write

$$H_{t-\Delta}(k) = \begin{bmatrix} -\Delta/2 & -t\cos(k) \\ -t\cos(k) & \Delta/2 \end{bmatrix} \tag{3.5}$$

in order to obtain the energy dispersion

$$\varepsilon(k) = \pm\sqrt{4t^2\cos^2 k + \frac{\Delta^2}{4}}\,. \tag{3.6}$$

It follows that Δ opens a charge and spin gap at $k = \pm\pi/2$, and the two gaps have the same value: exactly Δ, see Fig. 3.2. Therefore, the exponential decay of spin-spin and charge-charge correlations confirm that the system is a band insulator. Without the ionic potential, $\Delta = 0$, the model reduces to the one-dimensional Hubbard model, whose behavior is well understood, see Ch.1 and Refs. [312, 313]. The scenario does not change with the inclusion of a weak interaction, U; the electrons still prefer to doubly occupy sites with lower potential, and the system remains a band insulator.

3.1.3 Strong coupling limit

In the large-U limit, the double occupancy can be treated perturbatively and the low-energy physics of the IHM is described by the effective spin one-half Heisenberg model [314–317]

$$H_{eff}^{(4)} = J \sum_i \hat{S}_i \cdot \hat{S}_{i+1} + J' \sum_i \hat{S}_i \cdot \hat{S}_{i+2} \,, \tag{3.7}$$

where the exchange coupling constants are given by

$$J = \frac{4t^2}{U} \left[\frac{1}{1-\lambda^2} - \frac{4t^2}{U^2} \frac{1+4\lambda^2-\lambda^4}{(1-\lambda^2)^3} \right]$$

and

$$J' = \frac{4t^4}{U^3} \frac{1+4\lambda^2-\lambda^4}{(1-\lambda^2)^3} \,,$$

where $\lambda = \Delta/U$. Therefore, the strong-coupling limit of the IHM is the same as the strong-coupling limit of the Hubbard model, but with different J and J'. For $J' < 0.24J$ the spin gap vanishes [318].

Since the fourth-order terms are irrelevant, the exactly solvable nearest-neighbor Heisenberg model

$$H_{eff}^{(2)} = \frac{4t^2}{U^2 - \Delta^2} \sum_i \hat{S}_i \cdot \hat{S}_{i+1} \,, \tag{3.8}$$

already correctly describes this regime.

It is important to note that the system restores translation invariance, and that the charge and spin sectors are completely separated. We have gapless spin excitations, and critical spin-spin correlations, while the charge gap, in contrast, scales as U for large U. We call this phase the Mott-Heisenberg insulator [41]. This description is robust for a wide range of parameters in the strong coupling limit, but fails close to the transition line because perturbation theory breaks down in the critical regime [45]. In fact, there are numerical indications [319, 320] that show that higher-order spin excitations mix into the charge degrees of freedom everywhere in the Mott-Heisenberg phase.

3.1.4 Bosonization and more

A few years ago, Fabrizio, Gogolin and Nersesyan proposed a new, interesting scenario based on field-theoretical arguments [321]. They argued that two quantum

transitions occur, an Ising transition between the band insulator and an intermediate spontaneously dimerized phase, followed by (for increasing U/Δ) a Kosterlitz-Thouless-like transition between the dimerized phase and the Mott-Heisenberg insulator. This scenario is based on an argument in which the transition is approached from two different limits: from the Mott-Heisenberg insulator side and the band insulator, and demonstrates that two different types of transitions must occur.

First, the authors consider the weak-coupling case, $(U, \Delta) << t$, linearize the spectrum, and take the continuum limit by making the substitution

$$\frac{\hat{c}_{\ell\sigma}}{\sqrt{a}} \to i^{\ell}\psi_{R\sigma}(x) + (-i)^{\ell}\psi_{L\sigma}(x) \,,$$

where $\psi_{L,R}$ are the right and left components of the Fermi field. Thus, the fields are bosonized within the standard abelian bosonization framework [124]. The effective bosonized Hamiltonian is $H_{eff} = H_c + H_s + H_{cs}$, where the charge, the spin, and the spin-charge coupling contributions are

$$
\begin{aligned}
H_c &= \frac{v_c}{2}\left[\Pi_c^2 + (\partial_x\Phi_c)^2\right] \\
&\quad -\frac{g_3}{2(\pi\alpha)^2}\cos\sqrt{8\pi}\Phi_c + \frac{2g_2 - g_1}{\pi}\partial_x\phi_{cR}\partial_x\phi_{cL} \,,
\end{aligned}
\tag{3.9}
$$

$$
\begin{aligned}
H_s &= \frac{v_s}{2}\left[\Pi_s^2 + (\partial_x\Phi_s)^2\right] \\
&\quad +\frac{g_1}{2(\pi\alpha)^2}\cos\sqrt{8\pi}\Phi_s - \frac{g_1}{\pi}\partial_x\phi_{sR}\partial_x\phi_{sL} \,,
\end{aligned}
\tag{3.10}
$$

and

$$H_{cs} = -\frac{2\Delta}{\pi\alpha}\sin\sqrt{2\pi}\Phi_c\cos\sqrt{2\pi}\Phi_s \,, \tag{3.11}$$

respectively. Therefore, the spin and charge sectors are coupled by the parameter Δ. Nevertheless, under the assumption that the spin sector is gapless and that the charge sector is gapped, we integrate out the charge degrees of freedom and the Δ term goes directly to renormalize g_1 into the spin sector

$$g_1' = g_1 - C\frac{\Delta^2}{m^2}v_c \,.$$

Thus, the leading effective theory is the sine-Gordon Hamiltonian, which is known to undergoes to a continuous transition (KT) from the spin gapless (Mott-Heisenberg) phase to a spin gapped phase; the charge gap stays finite across the transition.

Thus, for U small and $(t, \Delta) << U$, the ionic potential shifts the opening of the spin gap to slightly larger U, compare with the Hubbard model

$$U_{c2} = \frac{2\pi t}{\ln(t/\Delta)} \left\{ 1 + O\left[\frac{\ln\ln(t/\Delta)}{\ln(t/\Delta)} \right] \right\}. \tag{3.12}$$

On the other hand, from the band-insulating side, they use free massive Fermions to describe the non-interacting band insulator in absence of interactions

$$H_{mfF} = \sum_{k\sigma} \left(\begin{array}{cc} \hat{c}^\dagger_{k\sigma} & \hat{c}^\dagger_{k+\pi\sigma} \end{array} \right) \left[\begin{array}{cc} -2t\cos(k) & \Delta \\ \Delta & 2t\cos(k) \end{array} \right] \left(\begin{array}{c} \hat{c}_{k\sigma} \\ \hat{c}_{k+\pi\sigma} \end{array} \right). \tag{3.13}$$

Subsequently, they introduce the most generic interaction compatible with the symmetry of the original IHM, and characterize instabilities through their generalized susceptibilities [109]. The instability analysis shows that the interaction drives the BI phase to a SDI phase via a transition in which the charge degrees of freedom take part and the spin degrees of freedom are excluded. Therefore, two different transitions must occur because of their entirely different nature. In fact, for small U and Δ, the two transitions are definitively separate, with

$$\frac{U_{c2}}{U_{c1}} - 1 = \frac{\text{const}}{\ln(t/\Delta)}.$$

Finally, they treated the Hamiltonian H_{eff} as a phenomenological Landau-Ginzburg energy functional; this allows them to investigate the nature of the transition from BI to SDI in all regimes. The saddle points of the effective potential in H_{eff} identify two possible phases: the massive BI phase, characterized by topological excitations carrying charge $Q = \pm 1/2$ and spin $S^z = \pm 1/2$, and the massive SDI phase, in which topological excitations have spin $S^z = 1/2$ and fractional charge. In addition, the effective potential becomes a massless φ^4-Ising-theory exactly at the BI-SDI transition point. The Ising scenario is also supported the behavior of the the charge degrees of freedom when the spin bosonic field is locked, as the instabilities indicate to be the case in the BI phase. The resulting effective model is a double sine-Gordon (DSG) Hamiltonian [322]

$$[H_c]_{\Phi_s=0,\sqrt{\pi/2}} = \frac{v_c}{2} \left\{ \Pi_c^2(x) + [\partial\Phi_c(x)]^2 \right\} - \frac{g}{\pi^2 a_0} \cos\sqrt{8\pi K_c}\Phi_c(x) - \frac{2\Delta}{\pi a_0} \sin\sqrt{2\pi K_c}\Phi_c(x), \tag{3.14}$$

in which a quantum phase transition of an Ising type is know to occur [323]. This model can be mapped to two coupled quantum Ising chains in a transverse field;

one of the chains passes through a critical point and the order parameter of the transition is proportional to the dimerization operator. Finally, Fabrizio, Gogolin and Nersesyan argued that the Ising transition in the charge sector would change to a first-order transition if an extra finite-range interaction, e.g., $V \sum_i n_i n_{i+1}$ were added to the model [322, 324].

3.2 Effective model

At least one transition consistent with the band-insulator-dimerized insulator has been found in all numerical work [288, 316, 319, 320, 324–328] published after Ref. [321], although, for the most part, without characterizing the critical behavior. However, even confirming that there is a second transition has been a quite difficult task. The two transitions turn out to be very close to one another and, since the transition to the Mott-Heisenberg insulator is expected to be a KT-like transition, it is very difficult to find and characterize using finite-size scaling studies [319]. Additionally, which energy scale characterizes the intermediate phase is not obvious from the original model. For these reasons, study of an effective model characterizing the region of the transition and the intermediate phase is useful.

Another very important subtlety is how to map the gaps from the field theoretical model onto the original lattice model. In the ionic Hubbard model, the charge gap, the one-particle gap, and the spin gap all behave differently at the transitions. The one-particle gap is related to the charge and spin gaps, but the first implies a change of one particle and the latter two are spectral gaps of excitations only in the charge or spin sectors, respectively. One way of locating critical points is to examine the smallest energy gap, i.e., the mass gap, as a function of the tuning parameters. The critical point is then the point at which the gap vanishes in the thermodynamic limit. However, this method has serious shortcomings when the transition is difficult to find. As we shall see, it is usually advantageous to use the static susceptibility related to the relevant order parameter to study the transition [319].

3.2.1 Derivation of the effective Hamiltonian

In order to investigate the critical behavior of the ionic Hubbard model at half filling, we derive an effective model, formulated in terms of spin-one operators, valid for $(U, \Delta) >> t$. In this limit, the doubly occupied state on the even sites (with on-site potential $\Delta/2$) and the unoccupied state on the odd sites can be projected out. At half-filling, a double occupancy on an even site is necessarily associated with a completely unoccupied odd site, with a cost in energy of $U + \Delta$. This procedure is a second-order strong-coupling expansion in $(U, \Delta)/t$ analogous

Table 3.1: Mapping between the single-site basis states of the ionic Hubbard model and those of the effective spin-one model.

$-\Delta/2$			$+\Delta/2$		
$\mid 0 \,\rangle$	$\rightarrow$	excluded	$\mid 0 \,\rangle$	$\rightarrow$	$\mid 0 \,\rangle$
$\mid \uparrow \,\rangle$	$\rightarrow$	$\mid 1 \,\rangle$	$\mid \uparrow \,\rangle$	$\rightarrow$	$\mid 1 \,\rangle$
$\mid \downarrow \,\rangle$	$\rightarrow$	$\mid -1 \,\rangle$	$\mid \downarrow \,\rangle$	$\rightarrow$	$\mid -1 \,\rangle$
$\mid d \,\rangle$	$\rightarrow$	$\mid 0 \,\rangle$	$\mid d \,\rangle$	$\rightarrow$	excluded

to that used to derive the t-J model from the Hubbard model. In fact, the resulting model can equivalently be formulated in terms of t-J operators rather than spin-one operators; we feel that the latter formulation is more intuitive for the half-filled system [329]. The physical meaning of the spin-one states is as follows: the $S_z = \pm 1$ state corresponds to a singly occupied site with a spin-1/2 electron with spin up or down, while the $S_z = 0$ state corresponds to an unoccupied site on the even sites and a doubly occupied site on the odd sites.

The mapping of the states of the ionic Hubbard model to the effective spin-one model is shown in Table 3.1. As we shall see, conservation of particle number leads to a spin exchange process for the spin-one operators that is more restricted than the Heisenberg exchange. Given this mapping of states, the effective Hamiltonian can most easily be derived by first expressing the original Hamiltonian as a function of the Hubbard operators [42, 330] $\hat{X}_i^{\alpha\beta} = |\alpha_i\rangle\langle\beta_i|$, defined as

$$\hat{X}_i^{\alpha\beta} = \begin{bmatrix} (\hat{1} - \hat{n}_\downarrow)(\hat{1} - \hat{n}_\uparrow) & \hat{c}_\uparrow(\hat{1} - \hat{n}_\downarrow) & \hat{c}_\downarrow(\hat{1} - \hat{n}_\uparrow) & \hat{c}_\downarrow\hat{c}_\uparrow \\ \hat{c}_\uparrow^\dagger(\hat{1} - \hat{n}_\downarrow) & (\hat{1} - \hat{n}_\downarrow)\hat{n}_\uparrow & \hat{c}_\uparrow^\dagger\hat{c}_\downarrow & -\hat{c}_\downarrow\hat{n}_\uparrow \\ \hat{c}_\downarrow^\dagger(\hat{1} - \hat{n}_\uparrow) & \hat{c}_\downarrow^\dagger\hat{c}_\uparrow & \hat{n}_\downarrow(\hat{1} - \hat{n}_\uparrow) & \hat{n}_\downarrow\hat{c}_\uparrow \\ \hat{c}_\uparrow^\dagger\hat{c}_\downarrow^\dagger & -\hat{c}_\downarrow^\dagger\hat{n}_\uparrow & \hat{n}_\downarrow\hat{c}_\uparrow^\dagger & \hat{n}_\downarrow\hat{n}_\uparrow \end{bmatrix}_{\alpha\beta,i} \tag{3.15}$$

and then mapping it onto the spin-one model expressed in terms of the operators $L_i^{ss'} = |s_i\rangle\langle s_i'|$ in the spin-one basis [331],

$$\hat{L}_i^{SS'} = \begin{bmatrix} \frac{(\hat{S}_i^z)^2 + \hat{S}_i^z}{2} & \frac{\hat{S}_i^z\hat{S}_i^+}{\sqrt{2}} & \frac{(\hat{S}_i^+)^2}{2} \\ \frac{\hat{S}_i^-\hat{S}_i^z}{\sqrt{2}} & \hat{1}_i - (\hat{S}_i^z)^2 & -\frac{\hat{S}_i^+\hat{S}_i^z}{\sqrt{2}} \\ \frac{(\hat{S}_i^-)^2}{2} & -\frac{\hat{S}_i^z\hat{S}_i^-}{\sqrt{2}} & \frac{(\hat{S}_i^z)^2 - \hat{S}_i^z}{2} \end{bmatrix}_{SS',i}. \tag{3.16}$$

For instance, we rewrite the ionic potential and the Coulomb interaction as

$$\hat{H}_U = U \sum_{i=1}^{L} \hat{X}_i^{dd}$$

$$= U \sum_{j=1}^{L/2} \left(\hat{X}_{2j-1}^{dd} + \hat{X}_{2j}^{dd} \right) ,$$

and

$$\hat{H}_\Delta = \frac{\Delta}{2} \sum_{i=1}^{L} \left(\hat{X}_i^{\uparrow\uparrow} + \hat{X}_i^{\downarrow\downarrow} + 2\hat{X}_i^{dd} \right)$$

$$= \frac{\Delta}{2} \sum_{j=1}^{L/2} \left(-\hat{X}_{2j-1}^{\uparrow\uparrow} - \hat{X}_{2j-1}^{\downarrow\downarrow} - 2\hat{X}_{2j-1}^{dd} + \hat{X}_{2j}^{\uparrow\uparrow} + \hat{X}_{2j}^{\downarrow\downarrow} + 2\hat{X}_{2j}^{dd} \right) .$$

The single-site Hilbert space truncation is defined as

$$\begin{cases} \hat{X}_i^{\alpha\beta} \to 0 & \text{for } \alpha, \beta = 0 \text{ and } i = 2j - 1 \\ \hat{X}_i^{\alpha\beta} \to 0 & \text{for } \alpha, \beta = d \text{ and } i = 2j \\ \hat{X}_i^{\alpha\beta} = \hat{L}^{\alpha\beta} & \text{otherwise} \end{cases} . \tag{3.17}$$

Hence, the interaction and the potential parts are transformed to

$$\hat{H}_U = U \sum_{j=1}^{L/2} \hat{L}_{2j-1}^{00} , \tag{3.18}$$

$$\hat{H}_\Delta = -\frac{\Delta}{2} \sum_{j=1}^{L/2} \left(\hat{L}_{2j-1}^{11} + \hat{L}_{2j-1}^{-1-1} + 2\hat{L}_{2j-1}^{00} - \hat{L}_{2j}^{11} - \hat{L}_{2j}^{-1-1} \right) . \tag{3.19}$$

Altogether, defining the coupling constant $\varepsilon = U - \Delta$, the doping $\delta = N - L$, and writing the terms using spin-one operators, the two-term contribution becomes

$$\hat{H}_\varepsilon = -\frac{\varepsilon}{2} \sum_{i=1}^{L} \left(\hat{S}_i^z \right)^2 - \frac{\varepsilon}{2} L - \frac{U}{2} \delta . \tag{3.20}$$

Likewise, the hopping part is translated to

$$\hat{H}_t = t \sum_{i=1}^{L} \left(\hat{L}_i^{0-1} \hat{L}_{i+1}^{01} - \hat{L}_i^{01} \hat{L}_{i+1}^{0-1} + \hat{L}_i^{-10} \hat{L}_{i+1}^{10} - \hat{L}_i^{10} \hat{L}_{i+1}^{-10} \right) \tag{3.21}$$

that, rewritten in the spin one language, becomes

$$\hat{H}_t = \frac{t}{2} \sum_{i=1}^{L} \left(-\hat{S}_i^+ \hat{S}_i^z \hat{S}_{i+1}^- \hat{S}_{i+1}^z + \hat{S}_i^- \hat{S}_i^z \hat{S}_{i+1}^+ \hat{S}_{i+1}^z + \text{h.c.} \right) . \tag{3.22}$$

In summary, the Hamiltonian for the effective spin-one model can thus be expressed in terms of the usual spin-one operators, yielding $\hat{H}^e = \hat{H}_t^e + \hat{H}_\varepsilon^e + \hat{H}_{\text{const}}^e$, with the hopping term

$$\hat{H}_t^e = \frac{t}{2} \sum_{i=1}^{L} \left\{ \left(\hat{S}_i^+ \hat{S}_{i+1}^- + \hat{S}_i^- \hat{S}_{i+1}^+ \right) \hat{S}_{i+1}^z - \hat{S}_i^z \left(\hat{S}_i^+ \hat{S}_{i+1}^- + \hat{S}_i^- \hat{S}_{i+1}^+ \right) \right\} , \tag{3.23}$$

the interaction term governed by the single parameter $\varepsilon = U - \Delta$

$$\hat{H}_\varepsilon^e = -\frac{\varepsilon}{2} \sum_{i=1}^{L} \left(\hat{S}_i^z \right)^2 , \tag{3.24}$$

and the constant term

$$\hat{H}_{\text{const}}^e = \frac{\varepsilon}{2} L - \frac{U}{2} \delta . \tag{3.25}$$

Note that it is immediately clear from the effective model that the relevant energy scale for the transition is set by $\varepsilon = U - \Delta$. While the zeroth-order argument $(t = 0)$ indicates that there should be a transition between an ionic and a Mott-like phase near $U \sim \Delta$, the nature of the transition(s) and possible intermediate phases for finite t still needs to be determined.

A sketch of the allowed processes is shown in Fig.3.3. These processes are a relative small subset of those of the isotropic Heisenberg spin chain model, and the AFM exchange in the IHM maps to two scattering process in the effective model.

In particular, it is important to investigate whether the behavior in the vicinity of $\varepsilon = 0$ agrees with previous numerical results for the ionic Hubbard model, [316, 319, 324] as well as with field-theoretical treatments [321].

One relevant characteristic of the effective model is the extent to which the symmetries of the original model are preserved or modified. The interaction term $\hat{H}_\varepsilon^e$ is local, translation invariant, and depends only on $(S^z)^2$, in contrast to the on-site part of the IHM Hamiltonian (3.1). The greater symmetry of the effective model is a consequence of the particle-hole symmetry of the IHM at half-filling. (Note that the *interpretation* of the $S^z = 0$ state is not translationally invariant.) Since the spin exchange term has the same symmetries as the hopping term in the IHM, the remaining symmetries of the original model are preserved in the effective model. Conserved quantities in the original model, such as the total z-component
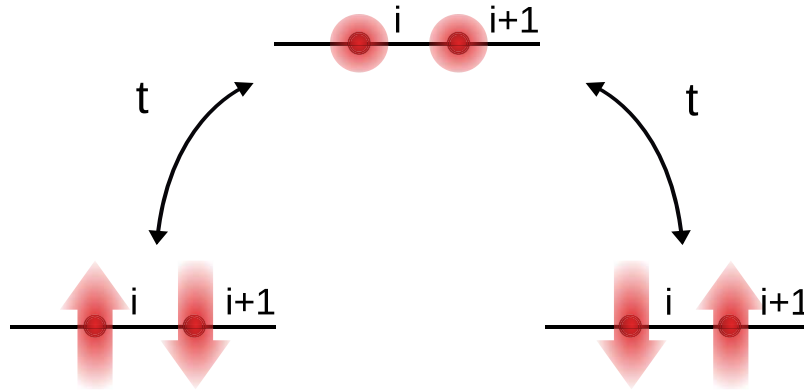
Figure 3.3: Sketch of the allowed processes, which are a relatively small subset of those of the isotropic Heisenberg spin-chain model. The drawing show how the AFM exchange in the IHM maps to two scattering process in the effective model.

of the spin, s_z, the total spin, s, and the number of particles, N, are still conserved in the effective model, but have different meanings.

One can also examine the expected phases in appropriate limiting cases. For $\varepsilon \gg t$, the on-site $S^z = 0$ state is strongly suppressed so that the remaining degrees of freedom, spin up and spin down, correspond to the localized spin-1/2 degrees of freedom of the MI phase of the original model. For $\varepsilon \to -\infty$, the $S^z = \pm 1$ local states are suppressed, leading to a ground state that is a simple product of local $S^z = 0$ states, which maps to the band insulator. At the transition between these two phases, the effective model allows the same low-lying charge and spin fluctuations as well as the same spontaneous breaking of site parity (an exact symmetry for periodic, but not open BCs) as the IHM.

Note that the derivation of the effective model can easily be extended to include additional interaction terms that do not break the symmetries of the original model, such as a next-nearest-neighbor Coulomb repulsion.

3.2.2 Observables

Since the formulation of the effective model in terms of spin-one operators is a notational convenience rather than physical, we are interested in studying observables relevant to the original model rather than the usual spin observables. Therefore, it is necessary to translate the observables relevant to the IHM into the language of the spin-one model. The local spin operators map as (small letters: IHM, capital

letters: effective model)

$$\hat{s}_i^z \;\rightarrow\; \frac{1}{2}\hat{S}_i^z\,,$$

$$\hat{s}_i^{\pm} \;\rightarrow\; \frac{1}{2}\left(\hat{S}_i^{\pm}\right)^2\,,$$

$$\hat{s}_i^2 \;\rightarrow\; \frac{3}{4}\left(\hat{S}_i^z\right)^2\,,$$

the local charge operators as

$$\hat{n}_i = \begin{cases} \left(\hat{S}_i^z\right)^2 & i \;=\; \text{even} \\[2em] 2-\left(\hat{S}_i^z\right)^2 & i \;=\; \text{odd}\,, \end{cases}$$

and total spin and charge operators as

$$\hat{s}^z \;\rightarrow\; \frac{1}{2}\hat{S}^z\,,$$

$$\hat{s}^2 \;\rightarrow\; \frac{1}{2}\hat{S}^z\left(\frac{1}{2}\hat{S}^z+1\right)+\frac{1}{4}\sum_{i,j=1}^{L}\left(\hat{S}_i^-\right)^2\left(\hat{S}_j^+\right)^2\,,$$

$$\hat{N} \;\rightarrow\; L+\sum_{i=1}^{L}(-1)^i\left(\hat{S}_i^z\right)^2\,.$$

As we can see, conservation of s^z in the IHM leads to conservation of S^z in the effective model, with the spin scaled by a factor of one half. However, conservation of the total spin in the IHM does not lead to conservation of total spin for the effective model, which is not $SU(2)$-invariant.

In Table 3.2 we show the mapping of the most important quantities from the original ionic Hubbard model to the effective spin-one model.

3.3 Numerical simulation

We have investigated the effective model by performing DMRG calculations for different system sizes, from $L=200$ up to 600 sites, with open boundary conditions (OBC). The algorithm performs best for even chains with OBC, but for small chains boundary effects can be large, depending on the correlation length. Thus, in order to minimize any dispersion due to the edges, or Friedel oscillations and

Table 3.2: Mapping of differt physical quantities to the effective spin one model.

	Ionic Hubbard model	Effective spin one model
Ionicity	$I = \dfrac{2}{L} \sum_{i=1}^{L} (-1)^i \langle \hat{n}_i \rangle$	$I = 2 - \dfrac{2}{L} \sum_{i=1}^{L} \langle \left(\hat{S}_i^z \right)^2 \rangle$
Polarization	$P = \dfrac{1}{L} \sum_{i=1}^{L} x_i \langle \hat{n}_i \rangle$	$P = \dfrac{1}{L} \sum_{i=1}^{L} (-1)^i \, x_i \langle \left(\hat{S}_i^z \right)^2 \rangle - \dfrac{1}{2}$
Electric susceptibility	$\chi_e = - \left. \dfrac{\partial P(E_x)}{\partial E_x} \right|_{E_x=0}$	$\chi_e = - \left. \dfrac{\partial P(E_x)}{\partial E_x} \right|_{E_x=0}$
Bond order parameter	$D = \dfrac{1}{L-1} \sum_{i=1}^{L-1} (-1)^i \langle \hat{c}_i^\dagger \hat{c}_{i+1} + \hat{c}_{i+1}^\dagger \hat{c}_i \rangle$	$D = \dfrac{1}{L-1} \sum_{i=1}^{L} (-1)^i \left[\langle \left(\hat{S}_i^+ \hat{S}_{i+1}^- + \hat{S}_i^- \hat{S}_{i+1}^+ \right) \hat{S}_{i+1}^z \rangle \right.$ $\left. - \langle \hat{S}_i^z \left(\hat{S}_i^+ \hat{S}_{i+1}^- + \hat{S}_i^- \hat{S}_{i+1}^+ \right) \rangle \right]$
B.o.p. susceptibility	$\chi_D = - \left. \dfrac{\partial D(h_D)}{\partial h_D} \right|_{h_D=0}$	$\chi_D = - \left. \dfrac{\partial D(h_D)}{\partial h_D} \right|_{h_D=0}$
AFM order	$A = \dfrac{1}{L} \sum_i (-1)^i \langle \hat{s}_i^z \rangle$	$A = \dfrac{1}{L} \sum_i (-i)^i \langle \hat{S}_i^z \rangle$
AFM susceptibility	$\chi_{\mathrm{AFM}} = - \left. \dfrac{\partial A(B_z)}{\partial B_z} \right|_{B_z=0}$	$\chi_{\mathrm{AFM}} = - \left. \dfrac{\partial A(B_z)}{\partial B_z} \right|_{B_z=0}$

odd-even effects, we analyze systems of at least 200 sites. In order to achieve sufficiently high accuracy, at least 5 sweeps must be performed, with up to 1280 states retained in the last one. The maximum system size that can be accurately treated is than approximately 600 sites. The maximum discarded weight of the density matrix for the effective model is then always less than 10^{-8}, and is typically zero to within the numerical precision far from the critical points. We target the ground state in the $S^z = 0$ sector, both the ground state target and the first excited state in the $S^z = 0$ sector, and the lowest state in the $S^z = 1$ and $S^z = 2$ sectors. These states correspond to the states needed in the original ionic Hubbard model to calculate the ground state energy, the "exciton" gap, the charge gap, and the spin gap.

We have repeated the same calculations using the dynamic block-state selection (DBSS) approach [258,332], fixing the threshold of maximum quantum information loss to $\chi = 10^{-6}/L$ at each step. For instance, $m \approx 500$ basis states are enough to correctly describe the ground-state wave function of a system 500 sites for $\varepsilon = 1.23$. However, as we increase ε, the number of states required increases, for example, $m \approx 900$ states must be kept to obtain the ground state at $\varepsilon = 2$. For ground states of other symmetry sectors, e.g., the lowest triplet excitation, this number is typically the same order as the number required for the overall ground state, but it can sometimes be much more larger despite the fact that its Fock subspace is smaller when the excited state is delocalized. Nevertheless, since we are interested in only the energy of these states and since measurements are carried out only on the ground state, keeping of the order of a thousand states is usually sufficient.

Therefore, we consider simulations with up to 500 sites to be under good control and those for $L = 550$ and 600 sites to possibly have a deficiency in accuracy when $m_{max} = 1280$, even near the critical region.

3.4 BI to SDI transition

In this section we will explore the region where we observe that the minimum of the mass gap goes to zero in the thermodynamic limit for $\varepsilon_c = 1.28(65)$ and reopens again; see Fig. 3.4, which shows the mass gap as a function of the system size. A level crossing is visible. For smaller ε values, the mass gap is purely determined by the singlet and the triplet is at much higher energy. The triplet and the first excited singlet cross just after the last reopens. For $\varepsilon \geq 1.35$ the triplet and the first excited singlet are degenerate, and the gap goes to zero exponentially with ε. We have compared results from the effective model to DMRG results for the IHM for $(U, \Delta) >> t$ in order to test the validity of the effective model [319]. All the quantities that we measure: gaps, ionicity, bond order parameter and polarization, are in good agreement to within a few percent.
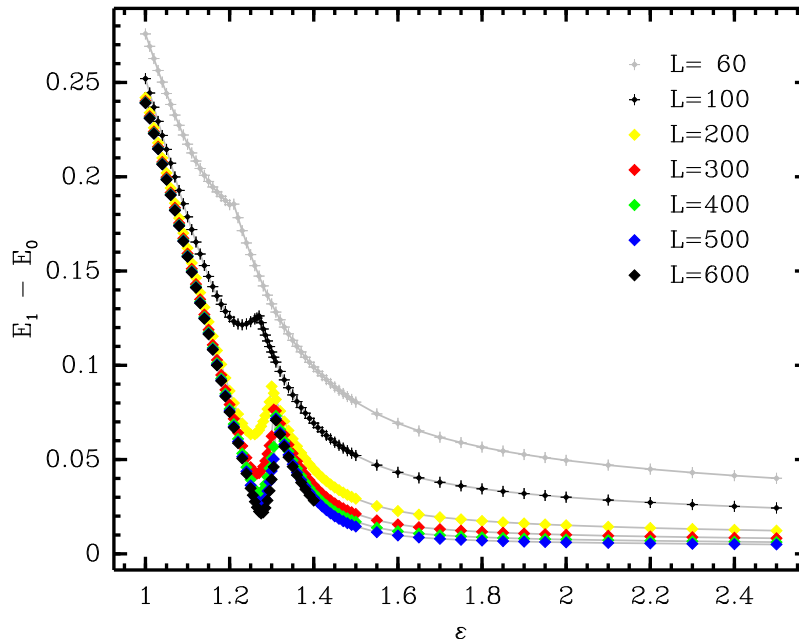
Figure 3.4: Mass gap as function of the coupling ε for different system sizes.

3.4.1 Dynamic critical exponent z

For a quantum system related to a classical model by the transfer matrix, the dynamical critical exponent can plays the role of an extra dimension, i.e., $z = 1$. In general, space and time correlations can be coupled and the value of z can be different from one. Therefore, an estimation of z is required to determine and interpret all exponents. First, we identify the mass gap [80], which here is given by

$$F(\varepsilon, L) = E_1(\varepsilon, L) - E_0(\varepsilon, L), \qquad (3.26)$$

taking the gap scaling to zero most quickly close to the critical point. This gap is proportional to the inverse of the correlation length, ξ^{-1}. Subsequently, since $\xi(L)$ is limited by the system size L [72], the ratio

$$\overline{R}_z(N, M, \varepsilon) = \frac{F(\varepsilon, N)}{F(\varepsilon, M)} \frac{N}{M} \qquad (3.27)$$

of the mass gaps for different system sizes behaves as $\overline{R}_z(\varepsilon_c, N, M) \sim (N/M)^{1-z}$ for $N, M >> 1$, and thus depends only on the ratio of system sizes. We plot all measured $\overline{R}_z$ ratios in Fig. 3.5. In Fig. 3.5 (a), we show that all the gap ratios with the same r cross $\overline{R}_z = 1$ at the same point. In Fig. 3.5 (b), curves with different r, scaled by the $L = 200$ gap, also cross at the same point. Thus, it is clear that

all curves cross each other approximately at the same value of ε, $\varepsilon \approx 1.3$, where $\overline{R}_z(N, M) \approx 1$, consistent with $z = 1$ [81].
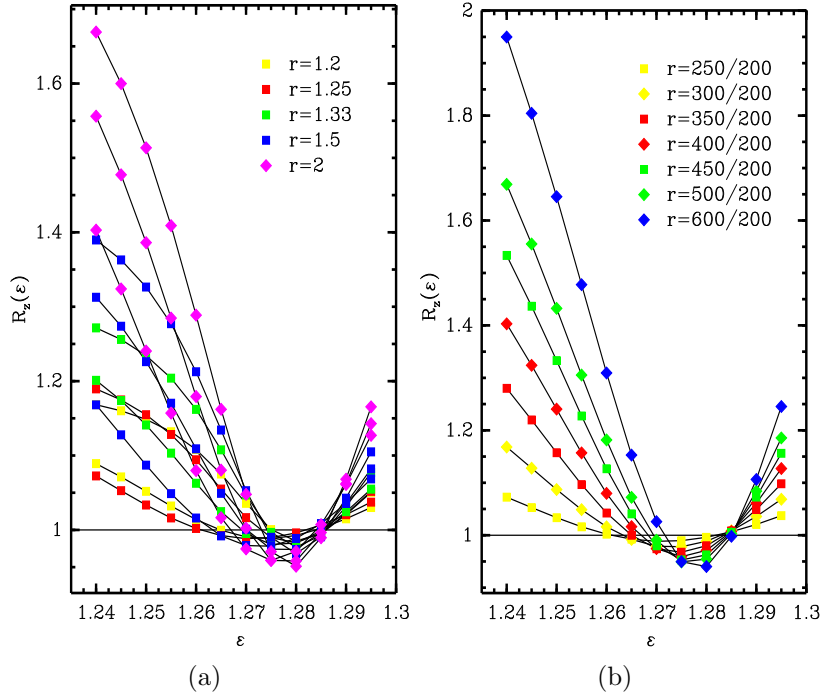

Figure 3.5: Different system-size gap ratios as function of the coupling ε. (a) Sets of gap ratios with the same ratio r. (b) Sets of gap ratios with different r, scaled by the $L = 200$ gap.

3.4.2 Correlation length exponent ν

Taking $z = 1$ from now on, we can use the definition of the logarithmic mass gap ratio [84]

$$R(L, \varepsilon) = \frac{\ln F(\varepsilon, L + 2) - \ln F(\varepsilon, L)}{\ln(L + 2) - \ln L} \qquad (3.28)$$

to estimate a series of pseudo-critical points converging to the critical point in the thermodynamic limit. The pseudo-critical points, $\varepsilon^*(L)$, are computed so that $R(L, \varepsilon^*) + 1 = 0$, as shown in Fig. 3.6. Since the mass gap goes to zero from both sides, the curves of the scaled ratio cross the line at two points, defining two possible sets of pseudo-critical points. Since this behavior could also indicate a first-order transition, we check that the minima of the normal ratio $\frac{F(\varepsilon, L+2)}{F(\varepsilon, L)} \frac{L+2}{L}$ converges to unity, as required if the transition is second-order [84]. We summarize all the

critical points in Fig. 3.6, which shows the two series of pseudo-critical points and mass-gap minimums. All curves are fit very well with third-order polynomials. In the thermodynamic limit they converge to the same point, to within the accuracy of the extrapolation, as can be seen in Fig. 3.6. Extrapolating using either series of

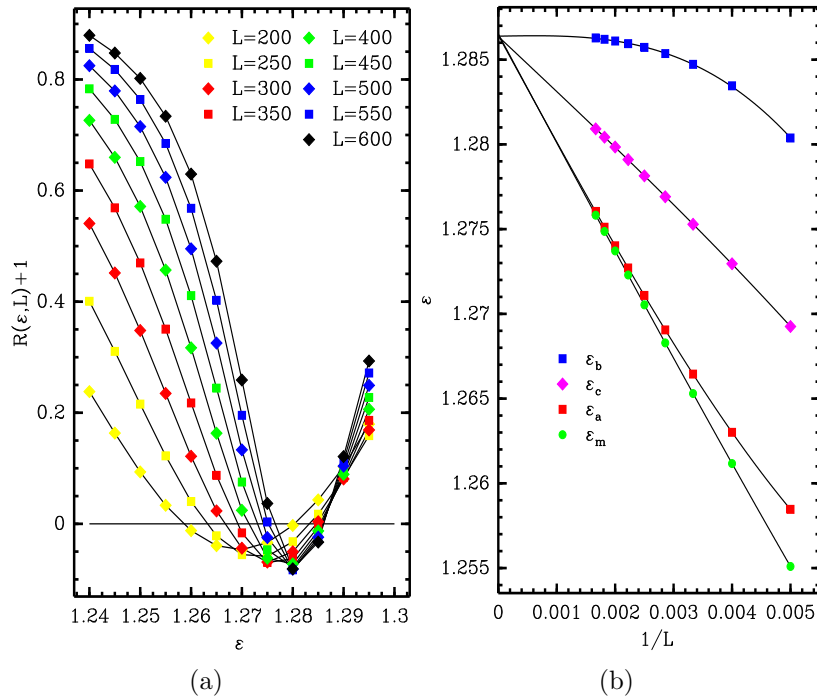(a)   (b)

Figure 3.6: Scaled logarithmic mass gap ratio and critical point extrapolation. The pseudo-critical series of points are shown, as well as the gap minimum. In the legend, ε_m is the position of mass gap minimum, ε_c is the position of the minimum of the scaled mass gap ratio, and, ε_a and ε_b are the first and the second series of pseudo-critical points. The lines are guides to the eye.

pseudo-critical points, which remain close to the gap minimum, can yield unreliable results because the derivative of the mass gap is zero or close to zero. By fitting the curves with a third-degree polynomial, we extrapolate to the thermodynamic limit and thereby obtain the critical point

$$\varepsilon_c = 1.28(64).$$ (3.29)

We can now use the finite-size version of the Callan-Symanzik [84, 85, 333, 334] β-function to estimate the correlation-length exponent

$$\beta_{cs}^{-1}(\varepsilon, L) = \frac{1}{F(\varepsilon, L)} \frac{\partial F(\varepsilon, L)}{\partial \varepsilon}$$ (3.30)

with the critical behavior

$$\beta_{cs}\left(\varepsilon_c, L\right) \sim L^{-\frac{1}{\nu}} . \tag{3.31}$$

To calculate the exponent ν, we proceed as follows: we calculate the ratio from the second series of pseudo critical points, $\varepsilon_L^* = \varepsilon_b(L)$:

$$\frac{\beta_{cs}(\varepsilon^*, L+l)}{\beta_{cs}(\varepsilon^*, L)} \sim \left(\frac{L+l}{L}\right)^{-\frac{1}{\nu}}$$

in the thermodynamic limit. If $|1/\nu| < 1$ and $L >> l$, then
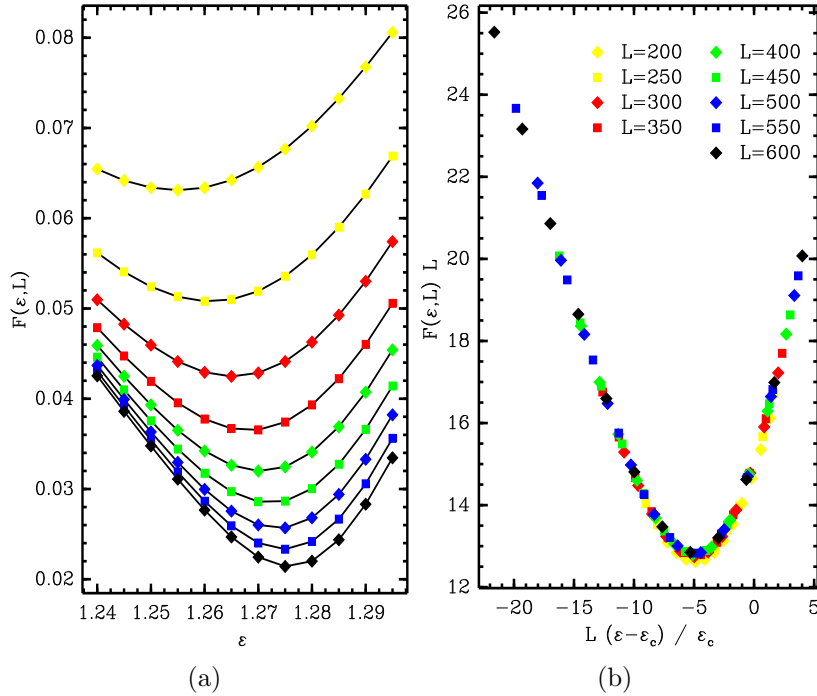

(a) (b)

Figure 3.7: (a) Scaling of the mass gap around the first critical point. The lines are guides to the eye. The picture on the right (b) is rescaled using $F(\varepsilon, L)L$. The collapse of the data onto a single curve confirms that $\nu = 1$.

$$\left(1 + \frac{l}{L}\right)^{-\frac{1}{\nu}} \sim 1 - \left(\frac{1}{\nu}\right)\frac{l}{L},$$

and

$$\frac{L}{l}\left[\frac{\beta_{cs}(\varepsilon^*, L+l)}{\beta_{cs}(\varepsilon^*, L)} - 1\right] \sim -\frac{1}{\nu} .$$

Additionally, we use the limiting behavior

$$\frac{\ln \beta_{cs}(\varepsilon^*, L+2) - \ln \beta_{cs}(\varepsilon^*, L)}{\ln(L+2) - \ln L} \sim -\frac{1}{\nu} \tag{3.32}$$

as a check. From the numerical extrapolation, we obtain

$$\frac{1}{\nu} = 0.99(6) \tag{3.33}$$

The plot of the mass gap collapse is shown in Fig.3.7.

3.4.3 Thermodynamic exponents β, α and γ

The bond order parameter is the order parameter of the bond-order-wave (BOW) phase. Fabrizio, Gogolin, and Nersesyan have argued that the bond order parameter is the right quantity to characterize the Ising-like transition in the IHM [321, 322]. The order parameter, expressed in the spin-one language, is

$$D(\varepsilon, L) = \frac{1}{L-1} \sum_{i=1}^{L} (-1)^i \left[\langle \left(\hat{S}_i^+ \hat{S}_{i+1}^- + \hat{S}_i^- \hat{S}_{i+1}^+ \right) \hat{S}_{i+1}^z \rangle \right.$$

$$\left. - \langle \hat{S}_i^z \left(\hat{S}_i^+ \hat{S}_{i+1}^- + \hat{S}_i^- \hat{S}_{i+1}^+ \right) \rangle \right] ; \tag{3.34}$$

see Fig. 3.8.
We use the bond order parameter to determine the second critical exponent, β

$$D(\varepsilon \sim \varepsilon_{c_1}, L) \sim L^{-\frac{\beta}{\nu}}. \tag{3.35}$$

Using the logarithmic derivative

$$\frac{\ln D(\varepsilon^*, L+l) - \ln D(\varepsilon^*, L)}{\ln L + l - \ln L} \sim -\frac{\beta}{\nu}, \tag{3.36}$$

we obtain:

$$\frac{\beta}{\nu} = 0.12(4) \tag{3.37}$$

The data are also ploted in Fig. 3.9. The excellent data collapse in Fig. 3.8(b) confirms that the transition point belongs to the 2D-Ising universality class.

Since, in a quantum phase transition, the coupling plays the same role as temperature in a thermal phase transition, we can define a corresponding "specific heat" [80, 335]

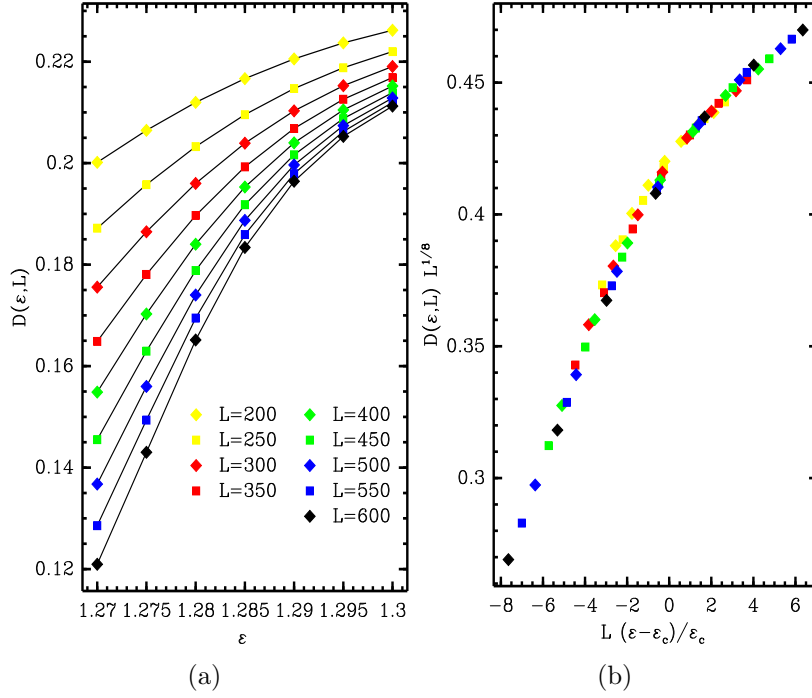$$c_v(\varepsilon, L) = -\frac{\varepsilon}{L} \frac{\partial^2 E_0(L)}{\partial \varepsilon^2} .$$

Figure 3.8: The bond order parameter as a function of the coupling ε around the transition point. (a) The bond order parameter for different system sizes near the first transition. (b) The collapse of the points as expected for a 2D-Ising universality class with $D(\varepsilon, L)L^{1/8}$.

Note that this quantity does not correspond to the real specific heat. Nevertheless, due to the scaling relations and its interplay with the other quantities, it has to diverge with the exponent α. The physical specific heat exponent is different and is related to our α by the Grüneisen parameter [336].

The specific heat usually contains a regular term that is typically larger in amplitude than the singular one. Therefore, instead of using the logarithmic derivative to estimate the exponent α/ν, we instead use

$$\frac{L}{2}\frac{c_v(L+2) - c_v(L)}{c_v(L)} \sim \frac{\alpha}{\nu}. \tag{3.38}$$

To overcome possible problems in determining this exponent, we use the Hellman-Feynman [337–339] theorem to exploit the accuracy of the DMRG in calculating local quantities

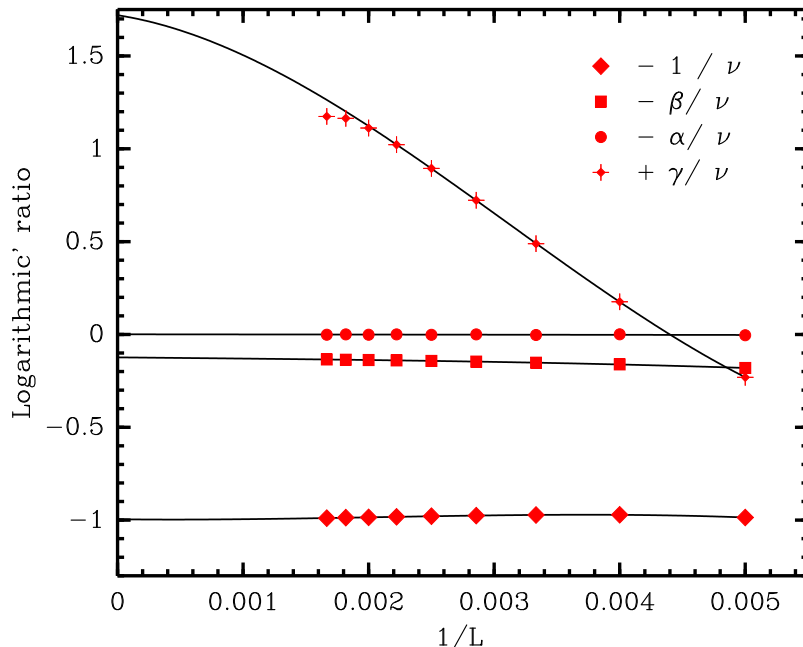$$\frac{\partial E_0}{\partial \varepsilon} = -\frac{1}{2}\sum_i^L \langle (\hat{S}_i^z)^2 \rangle. \tag{3.39}$$

Figure 3.9: Finite-size behavior of the exponents ν, β, α and γ. The fit is to a third-degree polynomial in $1/L$. Note that the points for the smallest $1/L$ are not included in fitting γ.

This trick reduces the computational cost to that of calculating the first derivative of the cubic spline, which interpolates the data points [207]. The result is the following:

$$\frac{\alpha}{\nu} = 0.00(1) \tag{3.40}$$

The finite-size behavior of the various exponents is plotted in Fig. 3.9. The first scaling relation $\alpha = 2(1 - \nu)$ is fulfilled, see Eq.(1.3).

Finally, we determine the exponent γ associated with the relevant susceptibility. The susceptibility corresponding to the bond order parameter is

$$\chi_D(\varepsilon) = -\frac{1}{L} \left. \frac{\partial D(\varepsilon, L)}{\partial h_D} \right|_{h_D=0}. \tag{3.41}$$

In order to calculate this quantity, we turn once more to the Hellman-Feynman theorem and to linear response theory. We perturb the Hamiltonian with a small field h_D conjugate to the order parameter D. The field has to be small enough to reveal a linear regime in the changes, but not smaller than the actual DMRG resolution; we use $2\delta h_D = 10^{-4}t$. Thus, we have measured the order parameter for 4 points around $h_D = 0$ in order to compute its first derivative at $h_D = 0$.
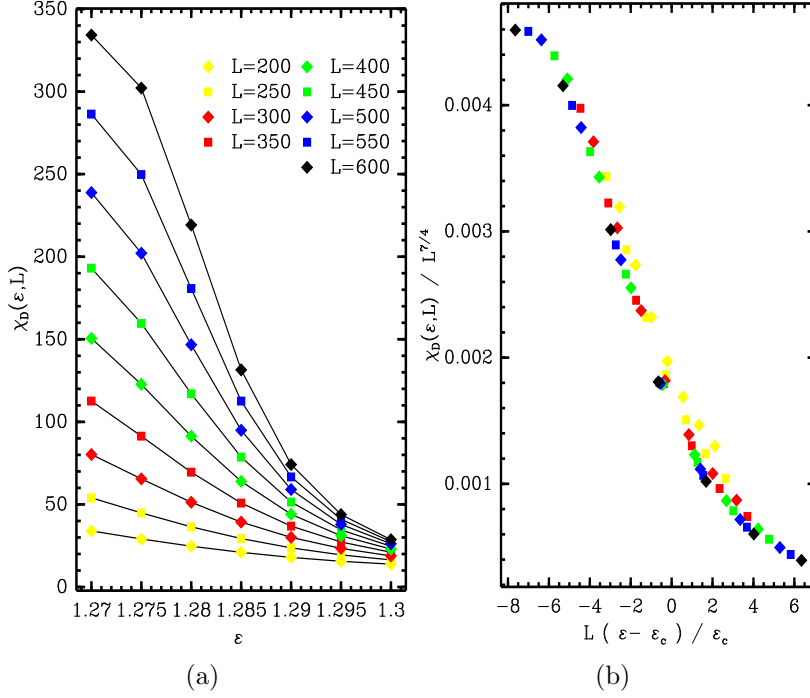
Figure 3.10: (a) Bond order parameter susceptibility as function of the coupling ε for different system sizes. (b) The collapsed curves obtained with an exponent $\gamma = 7/4$.

Once we have evaluated the static susceptibility for different system sizes, we proceed in the same way as for the previous exponents. The scaling relation is

$$\chi(\varepsilon_c, L) \sim L^{\gamma/\nu} \,. \tag{3.42}$$

Thus, from

$$\frac{\ln \chi(\varepsilon^*, L + l) - \ln \chi(\varepsilon^*, L)}{\ln (L + l) - \ln L} \sim \frac{\gamma}{\nu} \tag{3.43}$$

we obtain the last thermodynamic exponent, as plotted in Fig. 3.9

$$\frac{\gamma}{\nu} = 1.7(2) \tag{3.44}$$

As shown in the figure, the last points for the largest system sizes have been excluded in calculating the exponent. The reason is that the calculation of the susceptibility becomes uncontrolled for very big system sizes. In order to compensate the occurrence of non-linear behavior in the response for larger system sizes, we have to use a very small perturbation field. However, the effect of such a small

field can be difficult to distinguish from the numerical noise. In addition, we have to carry out two cubic-spline interpolations: one to determine the derivative of the bond order parameter as function of the perturbation field and one to fit its susceptibility. For these reasons we prefer to neglect them. We see that the second scaling relation $\gamma = 2(\nu - \beta)$ is fulfilled to within our estimated error, see Eq.(1.3).

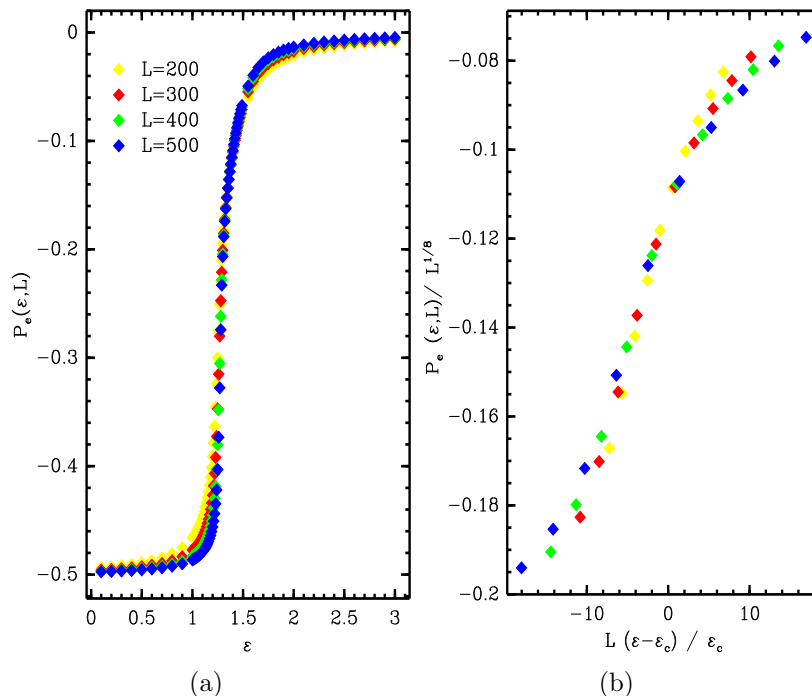Other quantities such as the electric polarization and the electric susceptibil-

Figure 3.11: (a) The electric polarization P_e as function of the coupling ε for different system sizes. The collapsed curve in (b) confirms the Ising character of the transition.

ity scale with the same exponents of bond order parameter and its susceptibility, respectively. This confirms the universality class of the transition, see the data collapse in Fig. 3.11 and Fig. 3.12.

In addition, we have calculated the value of the central charge using the method of Ref. [291]. The scaling of the low-lying energy levels with system size is uniquely determined by the conformal tower. This scaling can be used to determine the central charge [100]. The value obtained, $c = 0.5(0)$, is consistent with that expected for the 2D Ising model. We determine the central charge using the entropy profile in chapter 5 and obtain the same value ($c \approx 0.5$) at ε_c.
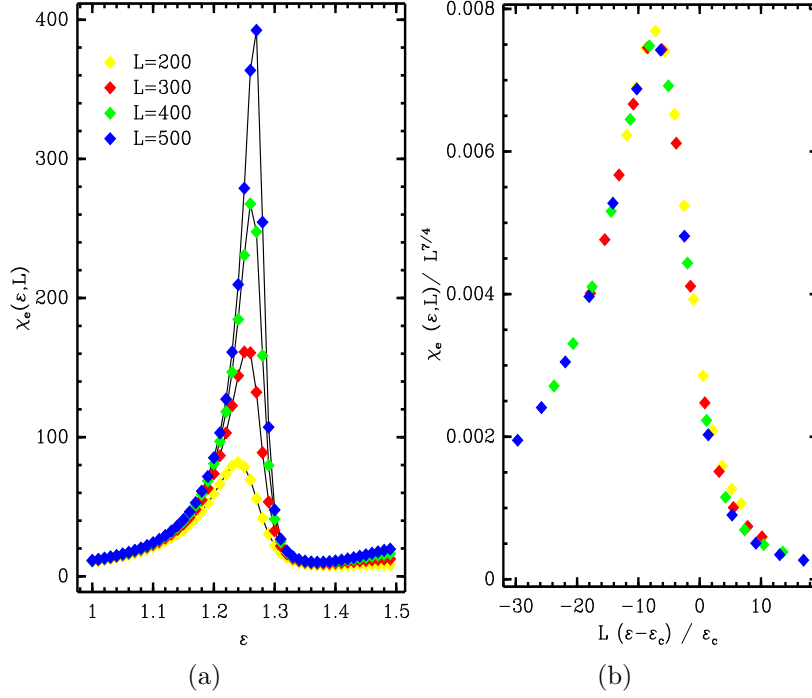
Figure 3.12: (a) The electric susceptibility χ_e as function of the coupling ε for different system sizes. The collapsed curve in (b) confirms the Ising character of the transition.

3.5 SDI to MI transition

In this section we analyze how the spin gap closes in the vicinity of the second critical point, see Fig. 3.4. This point corresponds to an essential singularity in the energy gap and it delineates the beginning of the critical region. Presumably, the transition is driven by marginal operators that induce logarithmic corrections which are typical for a $c = 1$ CFT [124]. Therefore, a more careful treatment than at the 2D Ising transition point is required.

3.5.1 Correlation length and mass gap

Here we present numerical results on the second critical point and determine its universality class. After the first critical point there is a change in the character of the mass gap, which formerly was determined by the gap between the ground state and the first singlet excited state. Here it is set by the gap between the ground state and the lowest-lying triplet, which is degenerate with excited singlet states.

The behavior of the mass gap energy is a clear signal of KT critical behavior:

the mass gap closes exponentially to a second critical point distinct from the first one; see Fig. 3.13. Therefore, in the thermodynamic limit and assuming that the transition is a KT transition, we write the singular part of the correlation length as

$$
\begin{aligned}
\xi\left(L=\infty\right) &= Ce^{b/t^{\sigma}} && \text{for} \quad 0 < t << 1 \\
\xi\left(L=\infty\right) &= \infty && \text{for} \quad t < 0
\end{aligned}
\tag{3.45}
$$

where

$$
t = \left(\varepsilon_c - \varepsilon\right)/\varepsilon_c ,
$$

and σ is the exponent of the essential singularity. (The XY model has $\sigma = 1/2$.) However, strictly speaking, we note that the expression for the correlation length is valid only in a narrow region close to the KT critical point, requiring the study of very large systems [340], or the inclusion of higher order corrections.

Nevertheless, neglecting the corrections, we consider a system of finite size L; hence, the correlation length is limited by L: $\xi\left(L\right) \sim L$. Therefore, we can define a set of pseudo-critical points, $\varepsilon^*(L)$, as for a second order transition, but it scales to the critical point ε_c logarithmically,

$$
\frac{\varepsilon^*\left(L\right) - \varepsilon_c}{\varepsilon_c} \sim \left(\ln L\right)^{-1/\sigma} .
$$

Analogously, all the points $\varepsilon > \varepsilon^*\left(L\right)$ constitute a pseudo-critical region. Since the mass gap is related to the inverse of the correlation length, we can apply the same arguments that we derived for the correlation length to it.

Furthermore, in a critical region described by a CFT the relation [178]

$$
E_i\left(L\right) - E_0\left(L\right) = \frac{2\pi x_i v}{L}
$$

is valid, where x_i is the scaling index and v the "excitation" velocity. As a result, in the plot of the mass gap times the system size L all curves merge into a single one exactly at the critical point ε_{c_2}; see Fig. 3.13. Therefore, the system is in a critical regime above a critical coupling $\varepsilon_{c_2} \approx 1.8$. The point at which the curves merge is clearly separated from the first critical point that we found at $\varepsilon_{c1} = 1.28(64)$. Since the distance between the two critical points is much bigger, $\Delta\varepsilon \approx 0.6$, than any deviation due to the logarithmic corrections, we conclude that there are two phase transitions.

In addition, we plot the mass gap ratio, but now the curves do not cross the line corresponding to a ratio of unity due to the logarithmic corrections [85]. Nevertheless, the curves stay very close to one everywhere in the critical region; see Fig. 3.14(a). The behavior of the mass-gap ratio curves further supports the KT scenario. They grow with the system size for $\varepsilon < 1.7$ and scale to one for larger
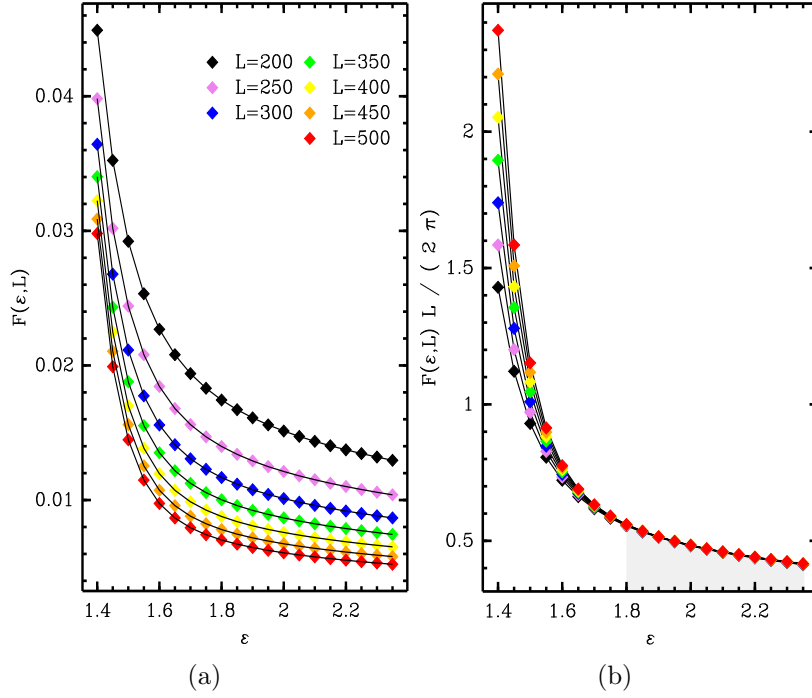
Figure 3.13: (a) Mass gap and (b) mass gap times L relative to the second critical point as function of the coupling ε and for different system sizes.

values of ε. In addition, we define and calculate the scaled difference of mass gaps, Q,

$$Q(\varepsilon; L', L) = \frac{L'}{2\pi} \frac{F(\varepsilon, L') \cdot L' - F(\varepsilon, L) \cdot L}{L' - L} \ .$$

For an arbitrary L', the first-order finite-size scaling terms cancel out and $Q(\varepsilon; L', L)$ vanishes in the critical region. In Fig. 3.14(b) we show results for $L' = 500$. We conclude that the critical point occurs at $\varepsilon_{c2} \approx 1.8$ and the gap closes exponentially.

We have also calculated the approximate β-function, see Eq. (3.30). However, for this kind of transition, it has no zeros as we might expect [85]. Nevertheless, we have extrapolated the value of the minima of the β-function to the thermodynamic limit and have found $\varepsilon_{\min \beta} = 1.9(2)$. The approximate β-function does not capture the peculiarity of a KT transition entirely because of the logarithmic corrections. Therefore, we argue that this value is larger than it should be.
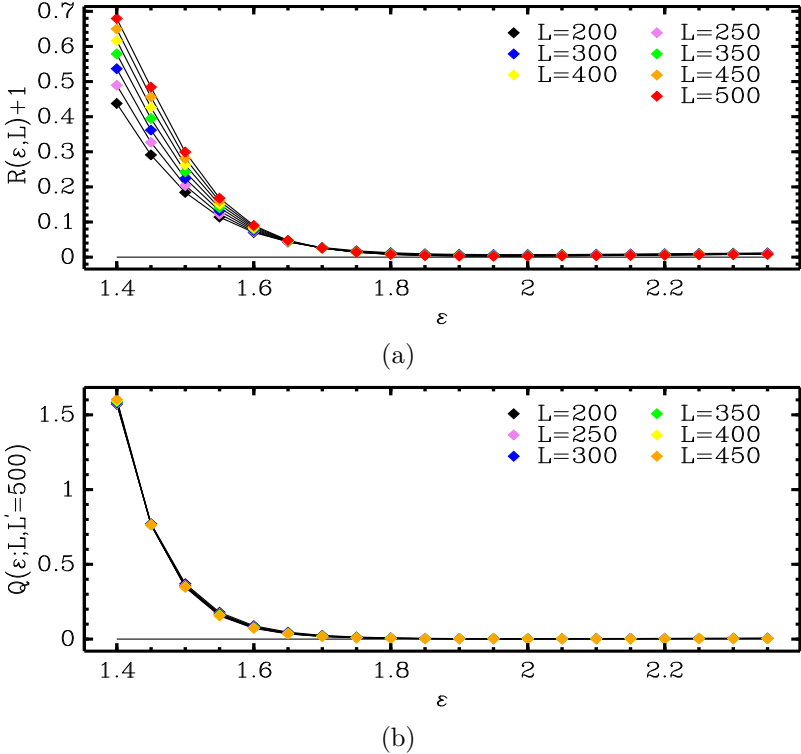
Figure 3.14: (a) The logarithmic mass gap ratio plus one. (b) The scaled difference of mass gaps Q for $L' = 500$ and various values of L.
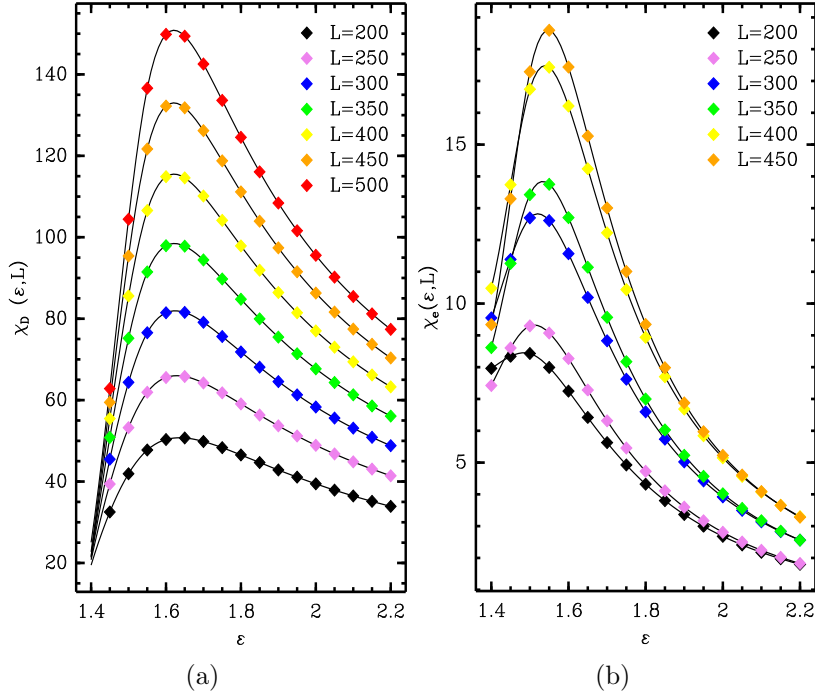
Figure 3.15: (a) The bond order susceptibility and (b) the electrical susceptibility for the second transition point.

3.5.2 The bond-order and electric susceptibility

In order to classify the transition as a KT transition we examine the bond-order susceptibility and the electric susceptibility; see Fig. 3.15. We look at the peak of the bond-order susceptibility in order to estimate the exponent of the susceptibility,

$$\gamma_{\text{peak}}^* (L) = \frac{\ln \chi \left(\varepsilon_{\text{peak}}^*, L + 2 \right) - \ln \chi \left(\varepsilon_{\text{peak}}^*, L \right)}{\ln (L + 2) - \ln L} \, .$$

Here we neglect the logarithmic corrections because the systems are not large enough to appreciate any deviations. The position of the peak in the bond-order susceptibility converges to the value $\varepsilon_{\text{peak}} \approx 1.6(2)$ and the series of pseudo-exponents, $\gamma_{\text{peak}}^* (L)$, converges to $\gamma \approx 1.2(7)$ in the thermodynamic limit. For comparison, we calculate the electric susceptibility, shown in Fig. 3.15(b). The finite-size effects are much stronger for the electric susceptibility than for the bond-order susceptibility. In fact, we observe a narrow peak that grows and moves with the system size. However, we conclude that the coincidence of the gap closing to zero exponentially with a diverging susceptibility corresponds to the typical scenario of an infinite-order phase transition. The critical exponent of the suscep-
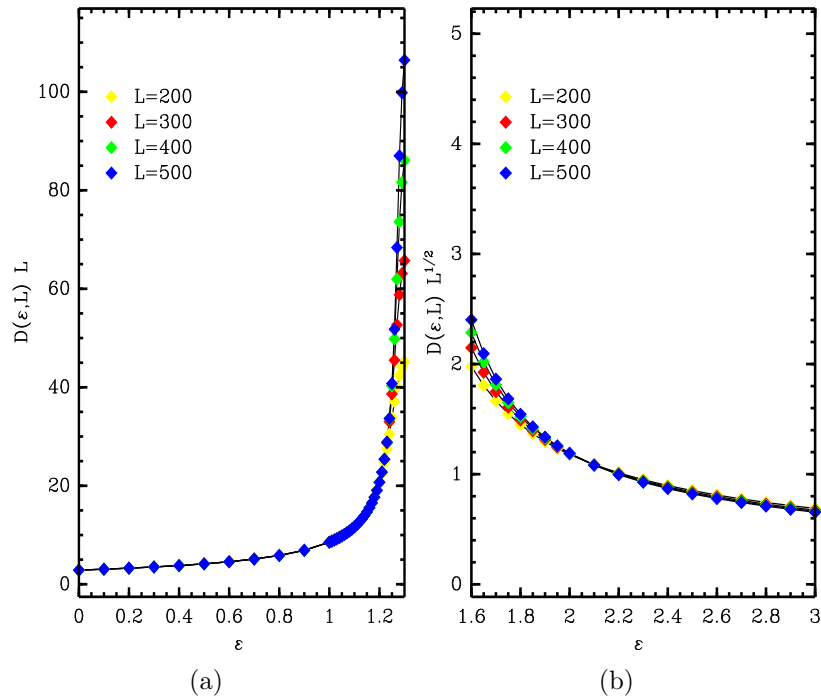
Figure 3.16: Collapse of the bond order parameter relative to the band insulator and Mott insulator phases. In (a) the scaling is relative to the band-insulator phase and the bond-order parameter scales to zero as $1/L$. In (b) bond-order parameter scales to zero as $1/\sqrt{L}$ plus corrections in the Mott-insulator phase.

tibility γ cannot be determined correctly because of the still strong influence of the bond-order wave that scale to zero very slowly as $1/\sqrt{L}$, see Fig. 3.16(b).

Additionally, we have calculated the central charge from the expression of the entropy profile that we use extensively in chapter 5. The result is consistent with the finite-size scaling analysis to a good approximation. The fitting parameter of the central charge has the value $c \approx 1$ (typical for a KT transition) near $\varepsilon_{cc} \approx 1.65$. At this point, the χ^2 of the fit has a minimum. However, more investigation would be necessary to address this issue.

3.6 Summary and outlook

In this chapter we have analyzed the band-to-Mott insulator transition in the strong-coupling limit. Using simple energetic arguments, we have derived a simpler effective model starting from the ionic Hubbard model. The effective model

captures the physics of the transition and is less computationally demanding than the ionic Hubbard model. The DMRG simulation has confirmed that there are two well defined transitions separated by a finite energy scale. The extraction of critical exponents for the first transition confirms that it belongs to the 2D Ising universality class. Subsequently, we have observed that the mass gap closes exponentially, and that all relevant susceptibilities diverge, behavior typical of a KT transition.

The mapping can be adapted to similar models or to extensions of the ionic Hubbard model, e.g., chains with other periodicities of the ionic potential or even two-dimensional problems. Another potentially useful application would be to relate exactly solvable spin-one models to electronic models and *vice versa* the spin-one models to spin-one-half models via the spin-one composite representation. In a similar context, related effective models were develop several years ago in Ref. [341] and recently in Ref. [342].

Another possibility that we are investigating is to bosonize the ladder chain obtained via the spin-one composite representation. This will determine which model is most fundamental to describe the band insulator to Mott insulator transition.

4 Mott insulator - Metal transition

During the last decades, the Mott metal-insulator transition has been the subject of great interest [41,343,344]. In the canonical model for this transition – the single-band Hubbard model – the origin of the insulating behavior is the on-site Coulomb repulsion between electrons. For an average density of one electron per site, the transition from the metallic to the insulating phase is expected to occur when the electron-electron interaction strength U is of the order of the delocalization energy (which is a few times the hopping amplitude t). The critical value $(U/t)_c$ turns out to be quite independent of the specific band structure [345]. It is important to recall that the Mott transition is often preceded by antiferromagnetic ordering, which usually leads to insulating behavior and thus masks the Mott phenomenon.

While the underlying mechanism driving the Mott transition is by now well understood, many questions remain open, especially about the region close to the transition point where perturbative approaches fail to provide reliable answers. The situation is more fortunate in one dimension, where non-perturbative analytical methods together with well-controlled numerical approaches allow both the ground state and the low-lying excited states to be determined in many cases [40, 312, 313]. However, even in one dimension, apart from the exactly solvable cases, a full treatment of the fundamental issues related to the Mott transition still constitutes a hard and long-standing problem.

In this chapter, we study the $t - t'$ Hubbard chain, which includes both nearest, t, and next-nearest-neighbor, t', hopping terms. We limit ourselves to an average density of one electron per site (the half-filled band case). Depending on the ratio between t' and t, the system has two or four Fermi points. Correspondingly, it shows one- or two-band behavior and has a rich phase diagram. Therefore, it is not surprising that the model has been the subject of intensive analytical and numerical studies, including a weak-coupling renormalization group analysis [346], DMRG calculations for charge and spin gaps [347–351], the electric susceptibility [352], the momentum distribution function [353–356], and the conductivity [351] as well as, very recently, a variational technique [357].

Unfortunately, conflicting results have been reported for the transition region, in particular regarding the character of the transition, the number of different phases and the number of gapless modes. In this work, we hope to settle some of the unresolved issues using a combined analytical and numerical analysis. We focus our attention on the insulator-metal transition as a function of t' for a fixed

on-site repulsion U. An effective continuum theory allows us to show that in the parameter range $0.5t < t' < t'_c$ the system exhibits the characteristic behavior of a commensurate-incommensurate transition [358–361]. Close to the transition point, additional scattering processes characteristic of two-band behavior [346] set in. We argue that these processes induce a crossover to Kosterlitz-Thouless type critical behavior, as found in Ref. [352]. The numerical analysis also allows us to study the gaps in the excitation spectrum as well as the charge and spin density distributions.

4.1 $t - t' - U$ **Hubbard model**

The one-dimensional $t - t'$ Hubbard model is defined by the Hamiltonian

$$
\begin{aligned}
\mathcal{H} \ = \ & -t \sum_{j,\sigma}^{L} \left(c_{j,\sigma}^{\dagger} c_{j+1,\sigma} \ + \ c_{j+1,\sigma}^{\dagger} c_{j,\sigma} \right) \\
& + \ t' \sum_{j,\sigma}^{L} \left(c_{j,\sigma}^{\dagger} c_{j+2,\sigma} \ + \ c_{j+2,\sigma}^{\dagger} c_{j,\sigma} \right) \\
& + \ U \sum_{j,\sigma}^{L} \left(n_{j,\uparrow} - 1/2 \right) \left(n_{j,\downarrow} - 1/2 \right),
\end{aligned}
\tag{4.1}
$$

where $c_{j,\sigma}^{\dagger}$ $(c_{j,\sigma})$ are electron creation (annihilation) operators on site j with spin projection $\sigma = \uparrow, \downarrow$, $n_{j,\sigma} = c_{j,\sigma}^{\dagger} c_{j,\sigma}$, and U is the on-site Coulomb repulsion.
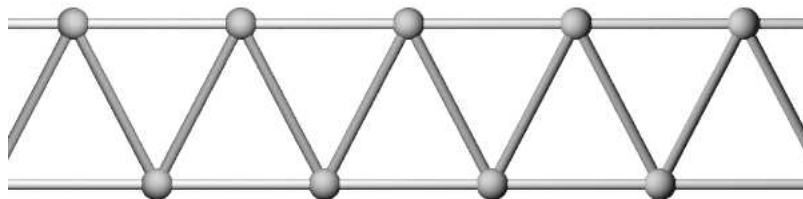

Figure 4.1: The $t - t'$ Hubbard chain.

The model can be viewed either as a single chain with both nearest- and next-nearest-neighbor hopping or, as illustrated in Fig. 4.1, as a system of two coupled chains. The former view is appropriate for $t \gg t'$, the latter for $t' \gg t$.

For $t' = 0$, we recover the ordinary Hubbard model which is exactly (Bethe Ansatz) solvable [312]. In the case of a half-filled band, the ground state is insulating for arbitrary positive values of U; the charge excitation spectrum is gapped while the spin excitation spectrum is gapless [312, 313]. For $U \ll t$ the charge gap Δ_c is exponentially small, $\Delta_c \approx \sqrt{Ut}e^{-2\pi t/U}$, while $\Delta_c \approx U$ for $U \gg t$ [313].

4.1.1 Noninteracting case

For $t' \neq 0$ the model is no longer integrable except in the non-interacting limit, $U = 0$, where H is diagonalized by Fourier transformation and has a single-electron spectrum

$$\varepsilon(k) = -2t \cos k + 2t' \cos 2k. \qquad (4.2)$$

For $t' < 0.5t$, the electron band has two Fermi points at $k_F = \pm\pi/2$, separated from each other by the umklapp vector $q = \pi$ (see Fig. 4.2). In this case, a weak-coupling renormalization group analysis [346] predicts the same behavior as for $t' = 0$ because the umklapp term of order U is not modified; it again leads to the dynamical generation of a charge gap for $U > 0$, while the magnetic excitation spectrum remains gapless. Note that the stability of the Mott insulating phase with respect to the weak perturbation caused by the next-nearest-neighbor hopping is an intrinsic feature of the 1D system, where the topology of the Fermi surface remains unchanged for $t' < 0.5t$. For instance, for the 2D half-filled $t - t'$ Hubbard model, the ideal nesting of the square Fermi surface at $t' = 0$ is broken by an arbitrarily small $t' \neq 0$, thereby destroying the insulating behavior for $U \to 0$ [362].

The two-chain band picture

For comparison with the ionic Hubbard model, we include the calculation for the two-band picture. Dividing the lattice into two sublattices, one containing the odd and one the even sites, we can rewrite the Hamiltonian

$$H_{tt'}(k) = \begin{pmatrix} 2t' \cos k & -2te^{-ik/2} \cos k/2 \\ -2te^{+ik/2} \cos k/2 & 2t' \cos k \end{pmatrix}. \qquad (4.3)$$

The solution of the secular equation yields the dispersion relation of Eq. 4.2, but the k-points are ordered differently. Since, the two diagonal elements are equal, the system is gapless for any value of t and t'.
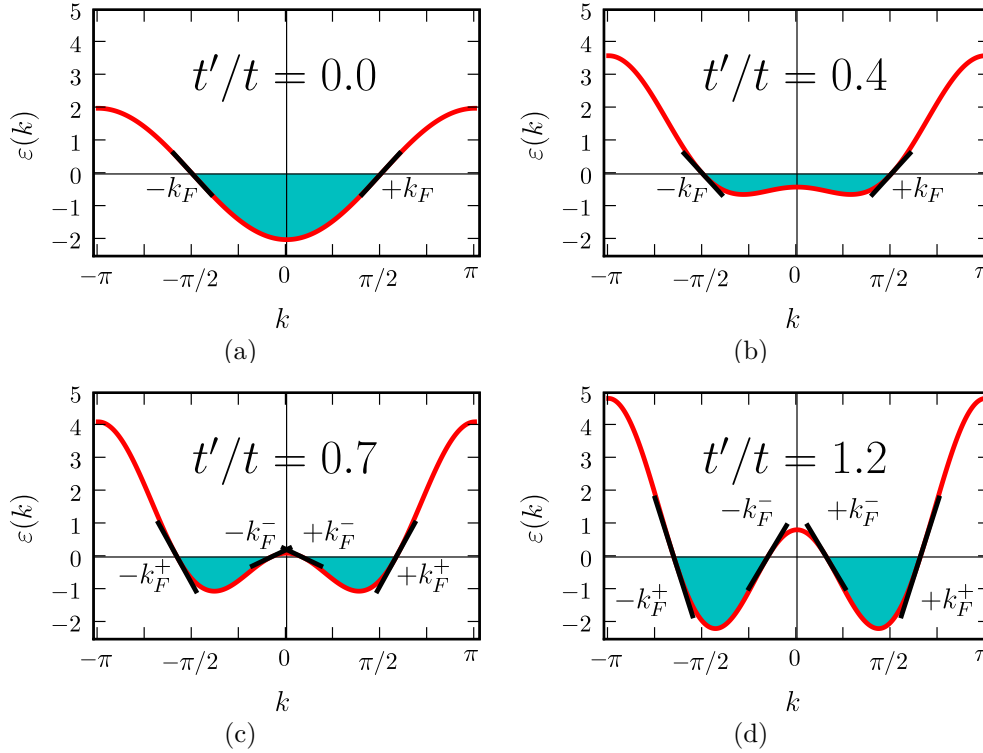
Figure 4.2: The $t - t'$ noninteracting band picture for $t = 1$ and different values of t'. For $0 \leq t' < 1/4$, (a), there is a minimum at $k = 0$ and there are two Fermi points at $k = \pm\pi/2$. For $1/4 < t' < 1/2$, (b), there are two minimum and the two Fermi points at $k = \pm\pi/2$ remain. At exactly $t' = 1/2$, there are three Fermi points at $k = 0$ and $\pm\pi/2$. For $t' > 1/2$, (c) and (d), there are four Fermi points. Fig. (a), (b), (c), and (d) are relative to $t' = 0\,,0.4\,,0.7\,,1.2$.

Finite-size effects

The discretization of the finite-size lattice and a strong energy-dispersion curvature can generate an artificial contribution to the gap. Increasing with system size, this contribution scales to zero in an unpredictable way because of the strong non-linearity of the energy spectrum near the Fermi points. For large t' the finite-size scaling is quite irregular. For small system size there is a quite big gap which oscillates incommensurately and scales to zero only for very large system size (see Fig.4.3). In the continuous case, all gaps are zero, in contrast to the lattice case where zeros occur only at special values of L and t'/t. The interaction term U reduces the finite-size effects because a gap is present. However, the problem is still persist for small U.
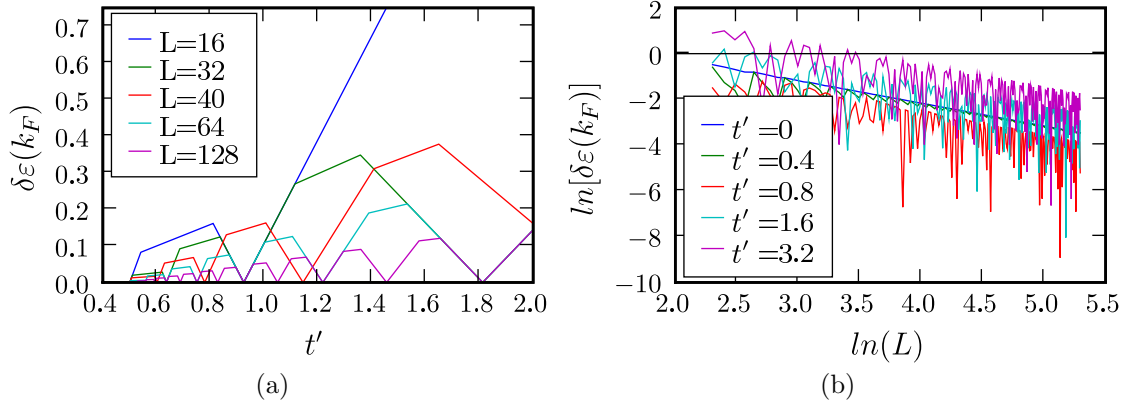
Figure 4.3: Finite-size effects in the incommensurate phase. (a) Dependence of the gap $\delta\varepsilon(k_F)$ on t' for different system sizes. Note that the zeros occurs at different t'-values for $L = 40$. (b) Finite-size scaling for various t' values, illustrating the irregular behavior due to incommensurateness.

4.1.2 Strong-coupling limit

In the strong-coupling limit, $U \gg t, t'$, the charge sector is gapped, while the spin sector can be mapped onto a frustrated Heisenberg chain

$$H = \sum_j \left(J\, \mathbf{S}_j \cdot \mathbf{S}_{j+1} + J'\, \mathbf{S}_j \cdot \mathbf{S}_{j+2} \right) , \qquad (4.4)$$

with $J = 4t^2/U$ and $J' = 4t'^2/U$. This model has been extensively studied using a number of different analytical methods [318, 363–366] and has been found to develop a spin gap for $J'/J \sim (t'/t)^2 > 0.2412$ [318, 363–365] and incommensurate antiferromagnetic order for $J'/J > 0.5$ [366]. This picture has been confirmed numerically [348, 350].

4.1.3 Two-chain limit

For $t' > 0.5t$, the Fermi level intersects the one-electron band at four points $\left(\pm k_F^\pm\right)$. This is the origin of more complex behavior for weak and intermediate values of U. For weak coupling ($U \ll t$), the ground-state phase diagram is well understood in the two-chain limit ($t' \gg t$) [346]. In this case, the Fermi vectors $k_F^\pm$ are sufficiently far from $\pi/2$ to suppress first-order umklapp processes. Therefore, the system is metallic. The infrared behavior is governed by the low-energy excitations in the vicinity of the four Fermi points, in full analogy with the two-leg Hubbard

91

model [367]. Thus, while the charge excitations are gapless, the spin degrees of freedom are gapped [346, 350, 351, 353, 354, 367]. Higher-order umklapp processes become relevant for intermediate values of U because the Fermi momenta fulfill the condition $4(k_F^+ - k_F^-) = 2\pi$ (at half-filling). Therefore, starting from a metallic region for small U at a given value of t' ($t' > 0.5t$), one reaches a transition line $U = U_c(t')$, above which the system is insulating with both charge and spin gaps [346].

4.2 The metal–insulator transition

4.2.1 Bosonization

We first consider the regime $U, t' \ll t$ where bosonization is applicable. After some standard algebra, we arrive at the bosonized version of the Hamiltonian (4.1)

$$\mathcal{H} = \mathcal{H}_s + \mathcal{H}_c \,,$$

where both the spin part

$$
\begin{aligned}
\mathcal{H}_s \;\; = v_s \int dx \;\; \Big\{ &\frac{1}{2}(\partial_x \varphi_s)^2 + \frac{1}{2}(\partial_x \vartheta_s)^2 \\
&+ \frac{m_s^0}{2\pi\alpha^2} \cos(\sqrt{8\pi}\varphi_s) \Big\},
\end{aligned}
\tag{4.5}
$$

and the charge part,

$$
\begin{aligned}
\mathcal{H}_c \;\; = v_c \int dx \;\; \Big\{ &\frac{1}{2K_c}(\partial_x \varphi_c)^2 + \frac{K_c}{2}(\partial_x \vartheta_c)^2 \\
&+ \frac{m_c^0}{2\pi\alpha^2} \cos(\sqrt{8\pi}\varphi_c) \Big\},
\end{aligned}
\tag{4.6}
$$

are described by the massive sine-Gordon model, with parameters

$$
\begin{aligned}
v_s \;\; &\approx \;\; v_c \approx v_F, \\
(K_c - 1) \;\; &= \;\; -2m_s^0 = 2m_c^0 \approx -U/\pi t \,.
\end{aligned}
\tag{4.7}
$$

There is an important difference between H_s and H_c due to the different stiffness constants. In the spin sector with $K_s = 1$, the system is in the weak-coupling limit and scales to a Gaussian model with gapless spin excitations. In the charge sector with $K_c < 1$, the system is in the strong-coupling regime and the low-energy behavior is dominated by the cosine term; see Ch.1. In the ground state, the field φ_c is pinned at one of the minima of the cosine term and, correspondingly, there is a finite energy gap for charge excitations.

Let us now discuss what happens when t' increases and reaches values of the order of $t/2$, where two additional Fermi points appear in the band structure. For spin degrees of freedom, new scattering channels appear at $t' = t/2$, and the system scales to strong coupling. Therefore, a spin gap is expected to open for $t' > t/2$, very much like in the case of two coupled Hubbard chains [367].

For the charge degrees of freedom, the situation is more complicated (and more interesting) because the charge gap blocks new scattering channels until t' is made sufficiently large so that additional states emerge beyond the gapped region. Thus, for t' slightly above $t/2$, the (bare) Fermi momentum changes without affecting the Umklapp processes. To discuss this phenomenon, it is useful to measure the single-particle energies with respect to the Fermi energy

$$\varepsilon_F = \begin{cases} -2t', & t' < 0.5t \\ \frac{-t^2}{2t'}, & t' > 0.5t \,. \end{cases} \tag{4.8}$$

In addition, the bosonized version of the single-particle part of the Hamiltonian introduces a chemical potential term $-2t'\sqrt{2/\pi}\int dx \partial_x \varphi_c$. In order to allow for a change of the particle number around the Fermi points $\pm\pi/2$, we therefore have to add a topological term

$$\delta H_c = -\mu_{\text{eff}}\sqrt{\frac{2}{\pi}}\int dx \, \partial_x\varphi_c \,, \tag{4.9}$$

where

$$\mu_{\text{eff}} = \begin{cases} 0 & \text{for} \quad t' < 0.5t \\ \frac{t^2}{2t'} - 2t' \neq 0 & \text{for} \quad t' > 0.5t \,. \end{cases} \tag{4.10}$$

The Hamiltonian $H_c + \delta H_c$ is the standard one for the commensurate-incommensurate transition [39, 124], and has been intensively studied in the past using bosonization [358–361] and the Bethe Ansatz [368].

We now apply the theory of commensurate-incommensurate transitions to the insulator-metal transition as a function of t'. At $\mu_{\text{eff}} = 0$ and $K_c < 1$, the ground state of the field φ_c is pinned at

$$\langle 0|\sqrt{8\pi}\varphi_c|0\rangle_0 = 2\pi n \,. \tag{4.11}$$

The presence of the effective chemical potential makes it necessary to consider the ground state of the sine-Gordon model in sectors with nonzero topological charge. Using the standard expression for the charge density in the case of two Fermi points, [124]

$$\begin{aligned} \rho_c(x) \quad \simeq \quad & \frac{1}{\sqrt{2\pi}}\partial_x\varphi_c \\ & + \quad A_{2k_F}\cos(2k_Fx)\sin(\sqrt{2\pi}\varphi_c)\cos(\sqrt{2\pi}\varphi_s) \\ & + \quad A_{4k_F}\cos(4k_Fx)\cos(\sqrt{8\pi}\varphi_c) \,, \end{aligned} \tag{4.12}$$
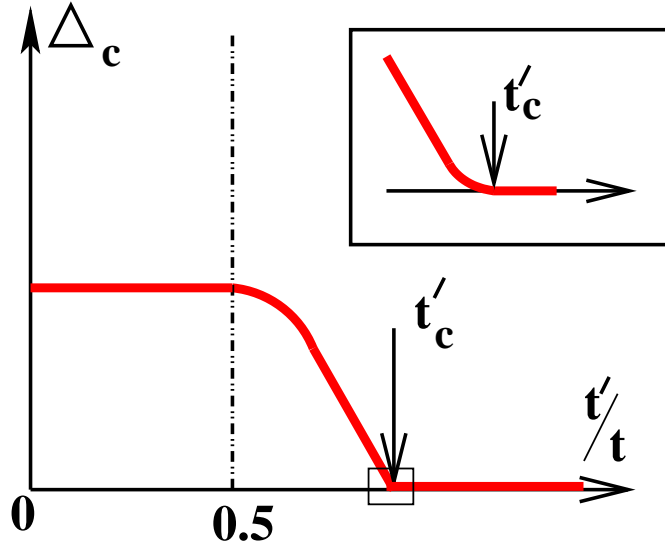
Figure 4.4: Sketch of the charge gap as a function of the parameter t'. The inset shows an enlargement of the vicinity of the transition point.

we observe that the pinning of the field φ_c in one of the minima (4.11) suppresses the $2k_F$ charge fluctuations and stabilizes the $4k_F$ component. Any distortion of the $4k_F$ charge distribution would require an energy greater than the charge gap. This competition between the chemical potential term and commensurability drives a continuous phase transition from a gapped (insulating) phase at $\mu_{\text{eff}} < \mu_{\text{eff}}^c$ to a gapless (metallic) phase at

$$\mu_{\text{eff}} > \mu_{\text{eff}}^c = \Delta_c \,, \tag{4.13}$$

where Δ_c is the charge gap at $\mu_{\text{eff}} = 0$.

We now separately consider the qualitative behavior of the system in the following three parameter regimes: *(i)* $t' < 0.5t$, *(ii)* $0.5t < t' < t_c'$, and *(iii)* $t' > t_c'$. In regime *(i)*, $t' < 0.5t$, we expect a charge gap $\Delta_c(U, t') \approx \Delta_c(U, t' = 0)$ and no spin gap, as in the simple Hubbard model ($t' = 0$). In regime *(ii)*, $0.5t < t' < t_c'$, the spin gap opens while the charge gap is reduced as

$$\Delta_c(U, t') = \Delta_c(U, 0.5t) - \mu_{\text{eff}} \,, \tag{4.14}$$

where μ_{eff} is given by Eq. (4.10). Therefore, the charge gap decreases with increasing t' and tends to zero at a t_c' qualitatively given by

$$\Delta_c(U, 0) - 2t_c' + t^2/2t_c' = 0 \,. \tag{4.15}$$

In regime *(iii)*, $t' > t'_c$, the behavior of the system is characterized by four Fermi points, $\pm k_F^{\pm}$. The charge excitations are gapless, while the spin excitations are, generically, gapped [346, 367]. Charge fluctuations will be characterized by two dominant periodic modulations with wave vectors $2k_F^-$ and $2k_F^+$. For t' slightly larger than t'_c, the usual charge-density wave ($2k_F^+ \approx \pi$) is accompanied by a long-wavelength modulation at $2k_F^-$.

Note that the closing of the charge gap is directly connected with the appearance of a "hole bag" at small momenta $|k| < k_F^-$, which is compensated (at half-filling) by the creation of occupied states at $\pi/2 < |k| < k_F^+$. (This will be discussed in more detail in Sec. 4.2.3 below.) Such a redistribution of occupied states in momentum space is generic for a transition in which the dynamically generated gap competes with some external parameter which tries to shift the system from the distribution most favored for gap formation. For example, in the case of the standard repulsive Hubbard model at half-filling, the chemical potential tries to shift the Fermi momenta of the system from the commensurate values $\pm\pi/2$, where the umklapp scattering processes responsible for the charge gap formation are relevant [124]. In the $t - t'$ Hubbard model, the same effect takes place via an increase of the next-nearest-neighbor hopping amplitude t'. Therefore, the gross features of the metal-insulator transition in the $t - t'$ Hubbard model are similar to those of the standard commensurate-incommensurate transition.

However, there is one important aspect which makes the metal-insulator transition in the $t - t'$ Hubbard model different from the case of the standard Hubbard chain. In marked contrast to the latter case, the metal-insulator transition in the $t - t'$ Hubbard chain is not associated with a change in the band filling. Therefore, the "effective" chemical potential is not an external parameter, but is instead determined by the hopping amplitudes t and t'. As a result, the change in the topology of the Fermi surface does not lead to complete suppression of the scattering processes responsible for the charge gap formation. Near the transition point, where the charge gap generated by the standard umklapp scattering processes vanishes, states in the vicinity of $k = 0$ will start to contribute to higher order umklapp scattering processes. These processes are responsible for the opening of a charge gap with increasing U in the two-band limit, i.e., when $t' \gg t$ [346]. Therefore, a crossover to the regime of two-band behavior takes place in the parameter range where the renormalized one-band (Hubbard) gap (4.14) becomes exponentially small. Therefore, the linear decay of the charge gap as a function of t' crosses over to exponential behavior. The evolution of the charge gap as a function of t' is sketched in Fig. 4.4.

4.2.2 Transition line

In order to investigate the detailed behavior of the metal-insulator transition and to test the validity of the picture obtained from bosonization, we have carried out numerical calculations using the DMRG [46, 47].
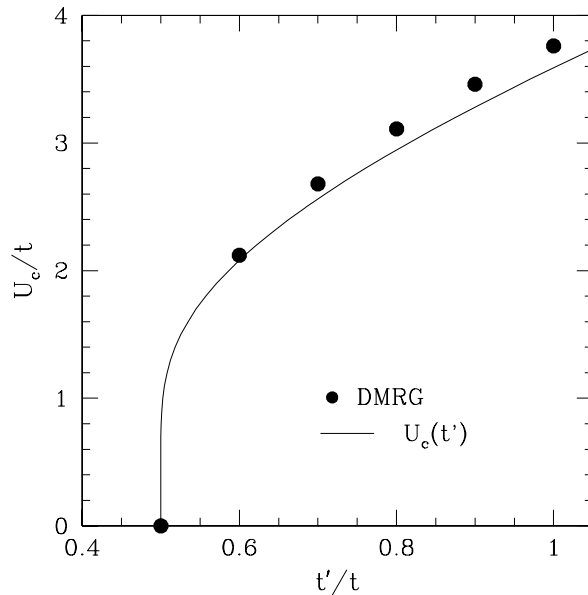

Figure 4.5: The metal-insulator transition line in the $t - t' - U$ model with $t = 1$ obtained from DMRG studies [352, 369] (black circles) and from Eq. (4.15) (solid line).

We have calculated the properties of the ground state and low-lying excited states for systems with open boundary conditions of lengths between $L = 32$ and $L = 128$ sites, keeping up to $m = 1000$ density-matrix eigenstates. As we shall see in the following, the finite-size effects are quite large in certain parameter regimes, so that a careful finite-size scaling must be carried out.

The critical behavior of the metal-insulator transition as a function of U/t for $t' > 0.5t$ can be obtained from the behavior of the electric susceptibility, which diverges in going from an insulator to a metal [352, 369]. In Fig. 4.5, we display the transition line in the $t - t' - U$ model at $t = 1$ obtained from the DMRG [352, 369] and from Eq. (4.15). The agreement between the DMRG results and Eq. (4.15) is remarkably good.

4.2.3 Momentum distribution function

In order to investigate the redistribution of occupied momentum states discussed at the end of Sec. 4.2.1, it is very instructive to examine the momentum distribution function calculated using the DMRG. The momentum distribution can be calculated by taking the Fourier transformation of the single-particle density matrix,

$$\langle n_k \rangle \equiv \frac{1}{2L} \sum_{i,\sigma} \sum_r \cos kr \ \langle c^\dagger_{i,\sigma} c_{i+r,\sigma} \rangle \tag{4.16}$$

with $k = \frac{2\pi}{L}n$ where $n = -L/2 + 1, ..., L/2$. Only the real part need be considered because the single-particle density matrix is even in r. In a system with periodic boundary conditions or an infinite system, the single-particle density matrix $\langle c^\dagger_{i,\sigma} c_{i+r,\sigma} \rangle$ would not depend on i due to translational invariance. For the open boundary conditions considered here, we carry out the average over i. While the discrete Fourier transform we use here is formally correct only for a periodic system, we find that using either an approximation to a Fourier integral or expanding in single-particle basis functions for open boundary conditions does not make a significant difference in the numerical results on the scale of the plots shown here.

In order to gauge the effect of the interactions, it is useful to compare with the momentum distribution for the noninteracting system. For $U = 0$, all momentum points within the Fermi points are fully occupied, i.e., $\langle n_k \rangle = 1$ only for $|k| < k_F$ for $|t'| < 0.5$ and only for $k_F^- < |k| < k_F^+$ for $|t'| > 0.5$, and all other k points are unoccupied, $\langle n_k \rangle = 0$; see also Fig. 4.2.

In Fig. 4.6, we present the momentum distribution as a function of t' for $U = 3t$. In the region $0 < t' < 0.6t$, $\langle n_k \rangle$ shows no qualitative differences from the $t' = 0$ case. Its insulating character manifests itself as a smooth variation of $\langle n_k \rangle$ at the Fermi points $\pm\pi/2$, in contrast to the Fermi step or Luttinger liquid singularity that one would expect for a metal. States near $k = 0$ begin to be removed at $t' \approx 0.6t$, significantly above the value at which the number of Fermi points changes from two to four in the noninteracting system ($t' = 0.5t$). The formation of this hole pocket proceeds continuously as t' is increased further. It is accompanied by a steepening of the slope of $\langle n_k \rangle$, both near k_F^- and near k_F^+. More studies will be needed to determine the detailed behavior of the momentum distribution function close to the Fermi points in this spin-gapped two-chain regime.

We have also performed simulations at larger values of U, where the first sign of a hole pocket appears at larger values of t', following essentially the metal-insulator transition line of Fig. 4.5. On the insulating side of this line, $\langle n_k \rangle$ is smooth, as expected.

Previously, we argued that the opening of the hole pocket occurs at the commensurate-incommensurate transition and leading to a shift in the metal-insulator transition
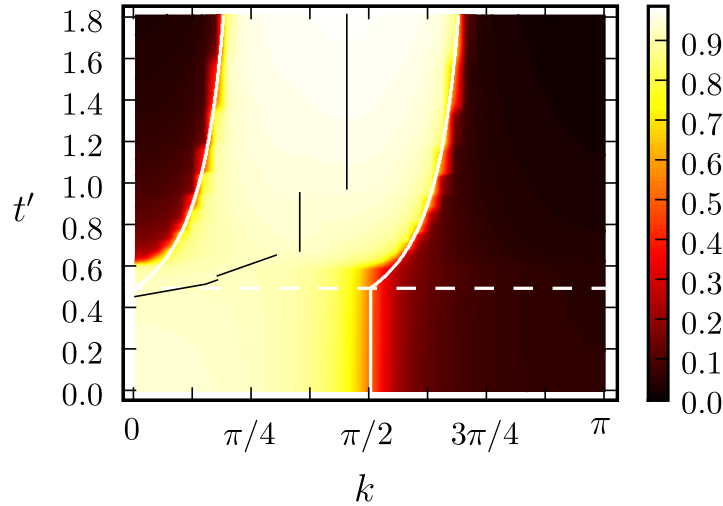
Figure 4.6: Momentum distribution $\langle n_k \rangle$ for $U/t = 3$ and system size $L = 80$. The white lines indicate the Fermi surface for $U = 0$, the black lines locate the maximum of $\langle n_k \rangle$.

to large values of t'. Fig. 4.7 shows the opening of the hole pocket at $k = 0$, which occurs exactly where we know where the commensurate-incommensurate transition takes place. At this small system size, $L = 32$, the finite-size effects are strong at small U values.

4.2.4 Charge and spin gaps

In order to investigate the predictions of the continuum theory, we calculate the charge gap, defined as

$$\Delta_c = \frac{1}{2} \left[E_0(N + 2, 0) + E_0(N - 2, 0) - 2E_0(N, 0) \right] \tag{4.17}$$

and the spin gap,

$$\Delta_s = E_0(N, 1) - E_0(N, 0), \tag{4.18}$$

where $E_0(N, S)$ is the ground-state energy for N particles and spin S on a chain of fixed length L, using the DMRG.

We will first examine the charge gap, starting with its system-size-dependence. In Fig. 4.8, we display the charge gap plotted as a function of the inverse chain length for various values of t' for $U/t = 3$. As can be seen, the scaling with $1/L$ is well-behaved for values of t' from 0 to 0.8. For $0 \leq t' \leq 0.6t$, the scaling has a substantial positive quadratic term in $1/L$ and the gap is finite. For $t' = 0.65t$ and $0.8t$, the extrapolated gap clearly vanishes and there is a negligible or
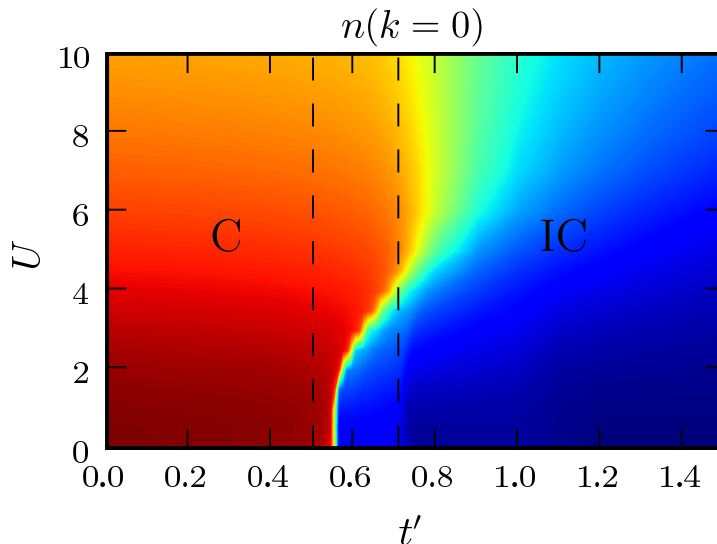
$$n(k=0)$$

Figure 4.7: The value of $n(k=0)$ as a function of U and t'. The red part corresponds to populated $k=0$ states and the blue to empty. The system size is $L = 32$. The vertical dashed lines represent the $t' = 1/2$ and $t' = 1/\sqrt{2}$ special cases.

negative quadratic contribution. For $t' > 0.8$ (not shown), the finite-size effects become irregular due to incommensurability of the charge excitations, and finite-size extrapolation becomes difficult.

In Fig. 4.9, the $L = \infty$ extrapolated value of the charge gap is displayed as a function of t' for $U/t = 2$ and $U/t = 3$. There is a clearly defined insulator-metal transition at $t_c = 0.55t$ at $U/t = 2$ and $t_c = 0.65t$ for $U/t = 3$. Note that the charge gap goes smoothly to zero above $t' = 0.5t$ for $U/t = 3$. The inset in Fig. 4.9 shows the charge gap for $U/t = 3$ as a function of the parameter $\mu_{\text{eff}} = 2t' - t^2/2t'$ for $0.5t < t' < 0.85t$. As can be seen, the charge gap drops off approximately linearly with μ_{eff}, in agreement with Eq. (4.14). For $U/t = 2$, there is a somewhat irregular behavior of the charge gap near the $t' = 0.5t$. In particular, there is a small peak exactly at $t' = 0.5$. The finite-size scaling for this point is completely regular, however, and we estimate the size of the total error, due to both the extrapolation and the DMRG accuracy, to be less than the symbol size. Therefore, in our estimation, the peak at $t' = 0.5$ is a real effect. For $t' = 0.55$, the value of the extrapolated charge gap is slightly below zero. This is due to errors in the finite-size extrapolation due to slightly irregular behavior with system size.

In Fig. 4.10, we display the spin gap as a function of t' at $U/t = 2$ and $U/t = 3$ for various values of the chain length L. As can be clearly seen, for $0 < t' \leq 0.5t$
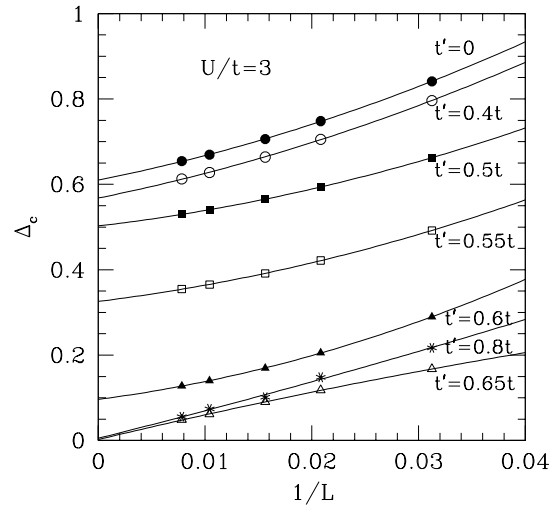
Figure 4.8: Charge gap of as a function of $1/L$ for $U/t = 3$ and various values of t'/t.

the spin excitation spectrum on finite chains does not depend on t'. For $t' \leq 0.5t$, the value of the spin gap is found to coincide with that of the half-filled Hubbard model ($t' = 0$) which vanishes in the infinite-chain limit [see Fig. 4.11].

A clear change in the t'–dependence of the spin gap at $U/t = 2$ takes place at $t' = 0.5t$, indicating the development of a new phase in the spin sector. It is known from other studies [346, 350, 351, 353, 354, 367] that a spin gap opens at a critical value of t' which is approximately at or slightly above $t' = 0.5t$, becoming weakly larger at intermediate U values.

In Fig. 4.11, we display the spin gap plotted as a function of the inverse chain length for three values of t' near the transition at $U/t = 3$. At $t' = 0.55t$, the spin gap clearly scales to zero at infinite system size, with the values at a particular system size virtually identical to the $t' = 0$ case and the scaling predominantly linear in inverse system size. For $t' = 0.6t$ and $t' = 0.65t$, the dominant scaling term is quadratic rather than linear in $1/L$ and there is clearly scaling to a finite value of the gap. For $t' = 0.65t$, the size of the extrapolated gap is smaller than for $t' = 0.6t$, and there is a slight upturn in the gap at the largest system size, which, however, is not significantly larger than the estimated error of the DMRG calculation, approximately the symbol size. However, for larger values of
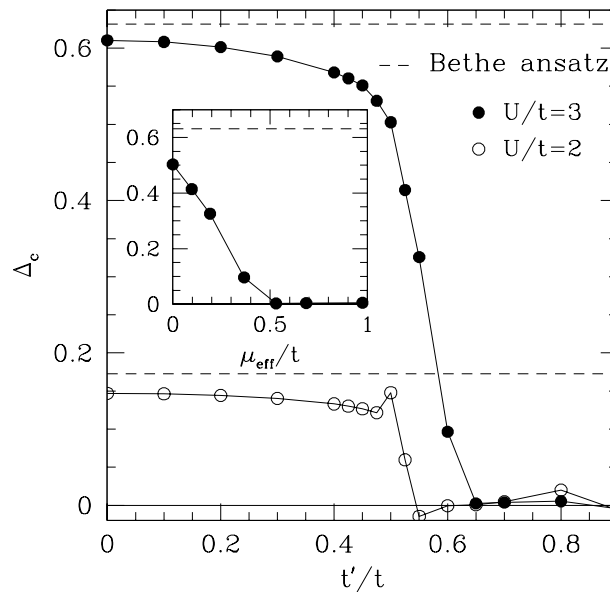
Figure 4.9: Charge gap of as a function of t' for $U/t = 3$ (black circles) and $U/t = 2$ (open circles). The inset shows the charge gap as a function of the parameter μ_{eff} for $0.5 < t' < 0.85t$.

t', the finite-size behavior becomes less regular, as can be seen in Fig. 4.10(a) and (b). This behavior is due to the appearance of an incommensurate wave vector characterizing the spin excitations that occurs when a substantial density of states at all four Fermi points develops and makes it virtually impossible to carry out a well-controlled finite-size scaling for larger values of t'.

The transition associated with the opening of the spin gap is independent of the insulator-metal transition, as can be clearly seen for $U/t = 3$ (where the effect of fluctuations is reduced). As is shown in Fig. 4.10(b) and Fig. 4.11, the spin gap opens for $t'_s \geq 0.55t$, while the insulator-metal transition takes place at $t'_c \simeq 0.65t$ (see Fig. 4.9). Note that the critical value of the next-nearest-neighbor hopping amplitude, corresponding to an opening of the spin gap at $U/t = 3$, $t'_s \geq 0.55t$, deviates from the line $t'_s \geq 0.5t$. Our findings agree with previous studies $[346, 350, 351, 353, 354, 367]$.

4.2.5 Two-chain limit

We now discuss the limit of strong next-nearest-neighbor hopping ($t' \gg t$). For $t = 0$, the system is decoupled into two half-filled Hubbard chains and, for arbitrary
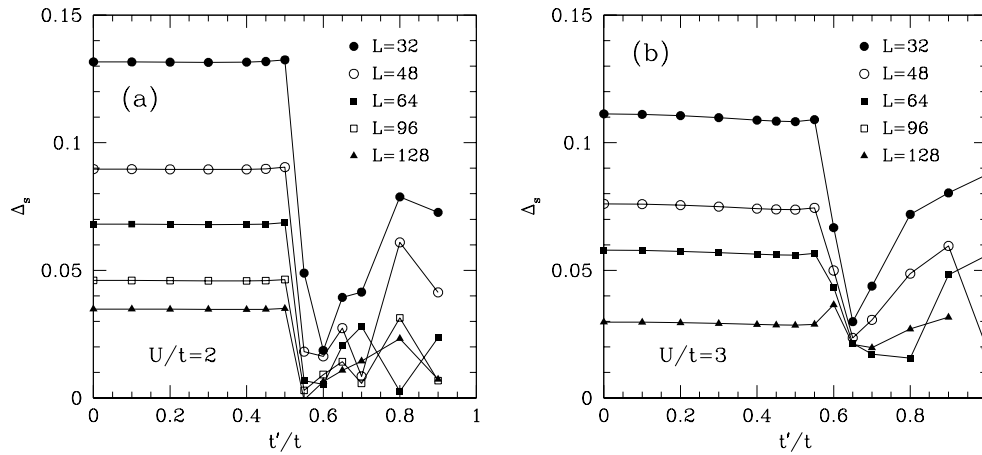
Figure 4.10: Spin gap of as a function of t' for (a) $U/t = 2$ and (b) $U/t = 3$.

$U > 0$, the ground state corresponds to a Mott insulator. The origin of the insulating behavior is the commensurability of umklapp scattering between the Fermi points, located at $\pm\pi/4$ and $\pm 3\pi/4$. When $t \neq 0$ this commensurability is lost. The Fermi points are shifted with respect to their values at $t = 0$, and the Fermi energy (the chemical potential for $U = 0$) moves away from 0 to $\varepsilon_F \approx -t^2/2t'$ (for $t \ll t'$). For large enough values of t, the system is therefore expected to be metallic.

In order to estimate the location of the Mott transition, we can use a similar argument to the one given above for $t' \approx 0.5$. As long as the chemical potential is smaller than the charge gap, the system remains an insulator. A transition to a metallic phase is expected to occur for ε_F of the order of Δ_c, i.e., for $t^2 \approx (Ut'^3)^{\frac{1}{2}} \exp(-2\pi t'/U)$. A qualitative sketch of the phase diagram is given in Fig. 4.12.

4.3 Spin-charge separation

4.3.1 Spin and charge densities

Valuable insight into the nature of the insulator-metal transition can be obtained by studying the charge density distribution in the ground state and the spin density distribution in the triplet excited state. The local density deviation $\langle n_\ell \rangle - \langle n \rangle$ on site ℓ and its Fourier transformation

$$\langle N_q \rangle \equiv \sum_\ell e^{-iq\ell} \left(\langle n_\ell \rangle - \langle n \rangle \right) \tag{4.19}$$
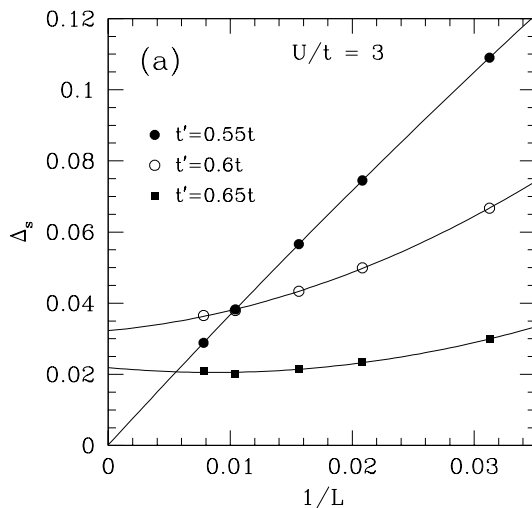
Figure 4.11: Spin gap as a function of $1/L$ for $U/t = 3$ and various values of t'/t.

yields information about the spatial and momentum components present in the ground state of a system with open boundary conditions because the ends behave like impurities which produce Friedel oscillations [370, 371]. Similar information about the lowest spin excited state in the triplet sector can be obtained by examining $\langle S_\ell^z \rangle$ and its Fourier transform $\langle S_q^z \rangle$, defined analogously to Eq. (4.19).

The Fourier transform of the charge distribution is shown in Fig. 4.13 for $U = 3$, an intermediate interaction strength, as a function of t'. For $t' < 0.6$, there are no significant fluctuations in the local charge density, as would be expected in one-chain picture ($\langle n_\ell \rangle = 1$ for all ℓ at $t' = 0$). At $t' \approx 0.6$ and larger, we see the development of peaks near $q = 0$ and $q = \pi$ which rapidly and symmetrically shift to higher and lower q values, respectively, with increasing t', going asymptotically towards $q = \pi/2$ for large values of t'. These peaks reflect scattering processes at $2k_F^-$ (low q) and $2k_F^+$ (high q). Above $t' \approx 0.9$, an additional peak at $q = \pi/2$ develops, quickly becoming dominant as t' is further increased. This peak is at the wave vector associated with scattering between the Fermi points, $k_F^+ - k_F^-$.

The behavior of the Fourier transform of the local spin density $|\langle S_q^z \rangle|$ of the ground state in the $S^z = 1$ sector is depicted in Fig. 4.14. For $t' \approx 0.5t$ and smaller, there is a single well-defined peak at $q = q^*$ slightly less than π. This is due to the soliton-antisoliton pair that makes up the lowest triplet excitation in a
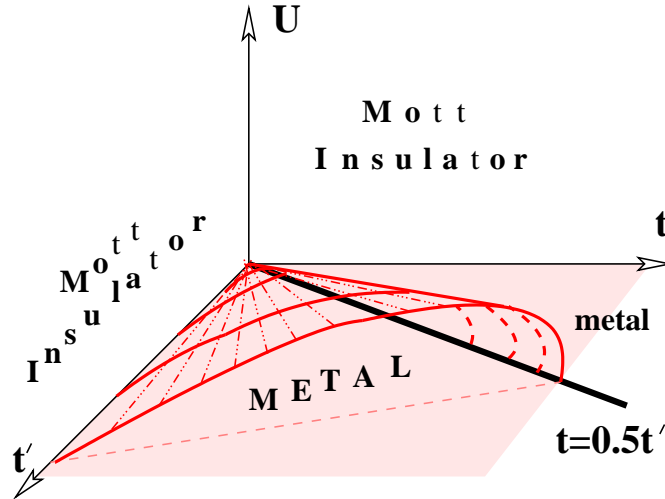
Figure 4.12: Qualitative phase diagram of the half-filled repulsive $t - t'$ Hubbard chain. A gapless charge excitation spectrum (metallic phase) exists at $U = 0$ for arbitrary t and t' and for $U > 0$ in the sector of parameter space below the "roof" covering the area $U < U_c$ between the lines $t' = 0.5t$ and $t = 0$ in the $U = 0$ plane.

single-chain picture, and is present in the Heisenberg chain. We expect q^* to shift closer and closer to π with system size because the size of the soliton-antisoliton pair is constrained by the number of sites. At $t' \approx 0.6$, this peak disappears rapidly with t' and is then replaced with a pattern of weaker peaks similar to those appearing in $|\langle N_q \rangle|$; compare with Fig. 4.13. The peaks starting near $q = 0$ and $q = \pi$ can again be attributed to $2k_F^-$ and $2k_F^+$ scattering processes. The peaks near $q = \pi/2$ are associated with scattering with wave vector $q = k_F^+ - k_F^-$.

Also evident in Fig. 4.14 are regular patterns as a function of t'. There are regular step-like structures in $|\langle S_q^z \rangle|$ as a function of t'. At the steps, there are interruptions in density, also marked by the appearance of peaks at additional scattering vectors. These effects are due to commensurability between the available low-lying scattering wave vectors, which change with t' and U, and the system size. In other words, when the appropriate wavelength of the excitation is commensurate with the system size, there is a shift and mirroring of the strongly weighted q points. This corresponds to a qualitatively more commensurate behavior of $\langle S_i^z \rangle$, as viewed in real space. These effects are also closely related to the irregular finite-size scaling of the spin gap, as seen in Fig. 4.10 for larger values of t'. Note that weaker, but analogous effects are also present in the charge density $|\langle N_q \rangle|$, Fig. 4.13.
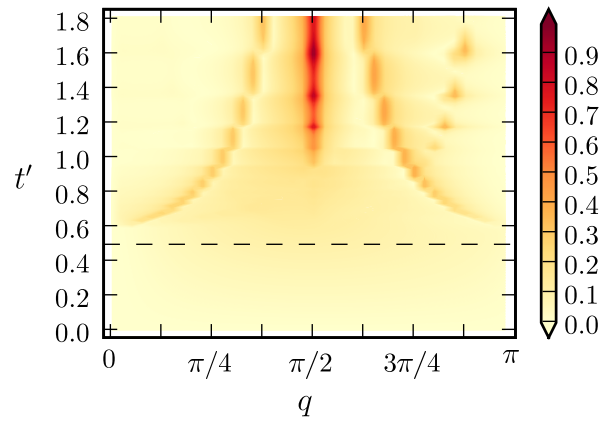
104

Figure 4.13: Density plot of the Fourier transform of the charge distribution $|\langle N_q \rangle|$ as a function of t' (vertical axis) for $U = 3$ on an $L = 80$ lattice.
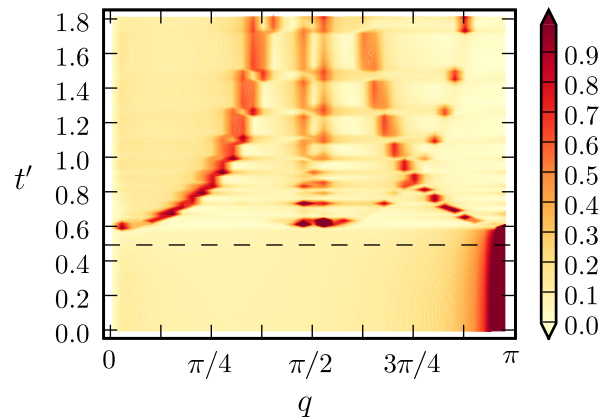

Figure 4.14: Density plot of the Fourier transform of the spin distribution $|\langle S_q^z \rangle|$ in the $S^z = 1$ state with lowest energy for $U = 3$ on an $L = 80$ lattice.

4.3.2 Charge and spin densities in the two-chain regime

We examine the behavior of the $t - t' - U$ chain for large next-nearest hopping ($t' \gg t$), a limit which corresponds to two chains coupled with a weak zigzag hopping. In particular, we numerically investigate the transition from a two-chain (four-Fermi-point) metallic regime at weak U to the strong-coupling regime, for which the effective model is two spin-$S = 1/2$ Heisenberg chains coupled with a frustrating zigzag interaction at $U \gg t' \gg t$, i.e., $J' \gg J$.
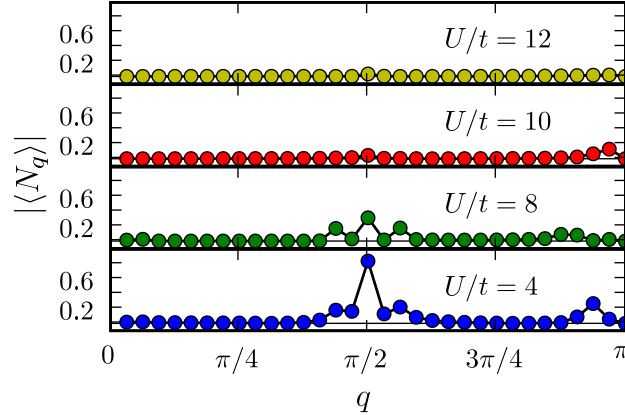
Figure 4.15: Fourier transform of the charge distribution $|\langle N_q \rangle|$ in the ground state of the $t - t' - U$ chain with $L = 64$, $t' = 3t$ and $U/t = 4, 8, 10, 20$.

In Fig. 4.15, we show the Fourier transform $\langle N_q \rangle$ of the charge distribution in the ground state of the $t - t' - U$ chain at $U = 4, 8, 10, 12$ for $t' = 3t$. In the metallic phase ($U/t = 4$ and $U/t = 8$), the strongest peak is at $q = \pi/2$, which corresponds to alternating charge density along each chain. In addition, there are side peaks which are due to weak alternations between the chains, as well as an incommensurate peak near $q = \pi$ due to asymmetric end effects on the two different chains, which shifts towards smaller q and becomes weaker as U is increased. As U/t is increased to 10, the amplitude of the charge fluctuations between the chains is strongly suppressed, as seen in the near disappearance of the peak at $q = \pi/2$. This indicates the transition to the insulating phase. The peak near $q = \pi$ now moves towards larger q, but becomes yet weaker with U. Deeper into the insulating phase, at $U/t = 12$, the Fourier transform of the charge density is almost featureless, corresponding to a real-space charge density which is smooth and equal between the chains.

In Fig. 4.16, we show the Fourier transform of the spin density distribution $\langle S_q^z \rangle$ in the $S_{\text{total}}^z = 1$ state for $t' = 3t$ and $U/t = 4, 8, 10, 20$. As can be seen, the weak incommensurate peaks on either side of $q = \pi/2$ present for $U/t = 4$ and 8 become

sharper and move towards $q = \pi/2$ as U is increased. These large-U excitations correspond to two-spinon excitations, as seen in the single Heisenberg chain, [372] in each chain. This behavior, also seen in the frustrated Heisenberg chain at large J'/J, indicates that the system behaves as two weakly coupled $S = 1/2$ Heisenberg chains at large U.
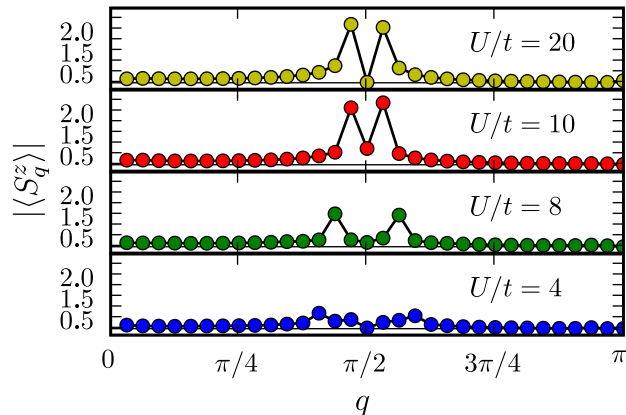
Figure 4.16: Fourier transform of the spin distribution $|\langle S_i^z \rangle|$ in the $S_{\text{total}}^z = 1$ state of the $t - t' - U$ chain with $L = 64$, $t' = 3t$ and $U/t = 4, 8, 10, 20$.

4.4 Discussion and related work

We have carried out a combined analytical and numerical analysis of the insulator-metal transition in the half-filled one-dimensional $t - t' - U$ model. Using the weak-coupling bosonization approach, we have shown that the gross features of the transition from an insulator to metal as a function of next-nearest-neighbor hopping t' can be described within the standard theory of commensurate-incommensurate transitions. We have derived an explicit expression for the critical line $t_c'(U)$ separating the metallic phase from the spin-gapped insulator. We have checked our conjecture by DMRG simulations.

Since I become involved in this project at a second stage, I point out my contributions. First, starting from the theory proposed, I suggested and implemented a better way to present the results. In particular, I characterized the charge and spin inhomogeneities through their Fourier transformations. Second, it was illustrative to connect the opening of the hole pocket with the commensurate-incommensurate transition. Therefore, I carried out several simulations to calculate momentum distribution, $n(k)$. In the next chapter, we discuss further investigations of the commensurate-incommensurate transitions via the von Neumann entropy.

5 Homogeneous-Inhomogeneous phase transition

Recently, the use of concepts of quantum information theory, such as the von Neumann entropy and other measures of entanglement between parts of a quantum system, has gained popularity in statistical physics and solid state physics. In particular, it has been shown that because these quantities exhibit discontinuities or extrema at transition points [373], they can be used to detect and locate quantum phase transitions that occur as the coupling constants are varied. This method has been used to study quantum phase transitions in low-dimensonal spin [225, 374–381] and fermionic [288, 382–386] problems.

In this chapter, we describe a new procedure which can be used to obtain additional information from the von Neumann entropy. We will show how to determine the wave vector characterizing the new phase when the system goes from a uniform to a spatially inhomogeneous phase. Similarly, if the system has soft modes, the method can extract their wave vector. Moreover, this method is well-suited for studying cases when no true phase transition takes place, but the decay of the correlation function changes character. Thus, this method provides a powerful new tool to determine the ground-state phase diagram of interacting quantum systems.

5.1 The entropy profile

The method we propose is based on the study of the length-dependence of the von Neumann entropy of a finite segment of a one-dimensional quantum system. It is known that this quantity behaves fundamentally differently for critical and noncritical systems [185, 267, 268]. The entropy of a subsystem of length l (in units of the lattice constant a) in a finite system of length N saturates at a finite value when the system is noncritical,

$$s(\ell) \sim \begin{cases} \ln \ell & \text{if} \quad \ell < \xi \\ \ln \xi & \text{if} \quad \ell > \xi \end{cases} ,$$

i.e., when the spectrum is gapped, while it increases logarithmically for critical, gapless systems. An analytic expression has been derived [186, 387] for models

that map to a conformal field theory [182]:

$$s(\ell) = \frac{c}{6} \ln \left[\frac{2N}{\pi} \sin \left(\frac{\pi\ell}{N} \right) \right] + g \,, \tag{5.1}$$

and this form has been shown to be satisfied by critical spin models. Here c is the central charge and g is a constant shift due to the open boundary which depends on the ground-state degeneracy. An additional alternating term, which decays as a power law, appears near the boundary [388].

In order to analyze the oscillatory nature of the finite subsystem entropy $s(\ell)$, it is useful to consider its Fourier transform

$$\tilde{s}(q) = \frac{1}{N} \sum_{l=0}^{N} e^{-iq\ell} s(\ell) \,, \tag{5.2}$$

with $s(0) = s(N) = 0$ where $q = 2\pi n/N$ and $n = -N/2, \ldots, N/2$. Since $s(\ell)$ satisfies the relation $s(\ell) = s(N - \ell)$, its Fourier components are all real and symmetric, $\tilde{s}(q) = \tilde{s}(-q)$; therefore, only the $0 \le q \le \pi$ region will be shown.

As usual in the DMRG approach, we consider open chains. The numerical calculations were performed using the dynamic block-state selection (DBSS) approach [244]. The threshold value of the quantum information loss χ was set to 10^{-8} for the spin models and to 10^{-4} for the fermionic model, and the upper cutoff on the number of block states was set to $M_{\mathrm{max}} = 1500$.

The length dependence of the von Neumann entropy of a subsystem can, in fact, display a much richer structure than discussed until now. Oscillations may appear; if so, they can be conveniently analyzed through the Fourier spectrum of $s(l)$ to detect phases with particular dimerization. The method is especially appropriate when the density-matrix renormalization-group (DMRG) algorithm [46,47] is used because the density matrix of blocks of different lengths are generated in the course of the procedure so that the von Neumann entropy can be easily calculated; see Ch.2.

5.2 Frustrated spin $1/2$ Heisenberg chain

The Hamiltonian of the spin 1/2 Heisenberg model with nearest-neighbor and next-nearest-neighbor spin exchange,

$$H = \sum_{i=1}^{L} \left(JS_i \cdot S_{i+1} + J'S_i \cdot S_{i+2} \right) \,,$$

is the simplest extension of Heisenberg model [42,389]. The $J' = 0$ case corresponds to the AFM or FM spin-1/2 Heisenberg model for $J > 0$ and $J < 0$ respectively. In

the past, the model has been extensively studied analytically [318,363,365,390–393] and numerically [364, 366, 394–396] and, except for the ferromagnetic case [397], where some issues still have to be addressed, the phase diagram is well established [398].

5.2.1 Classical limit

In the limit of classical vectors $(S \rightarrow \infty)$, the elementary unit of the lattice is a frustrated triangle with bonds J, J, and J', and the ground state can be parameterized by a spiral wave $\overline{S}_j = S\left[\cos(j\kappa), \sin(j\kappa), 0\right]$. The phase diagram is obtained by minimizing the energy density

$$E(\kappa) = S^2\left[J\left(\cos\kappa - 1\right) + J'\left(\cos 2\kappa - 1\right)\right]$$

with respect to κ; see Fig. 5.1. In the case of $J > 0$, the phase diagram is divided

(a)   (b)
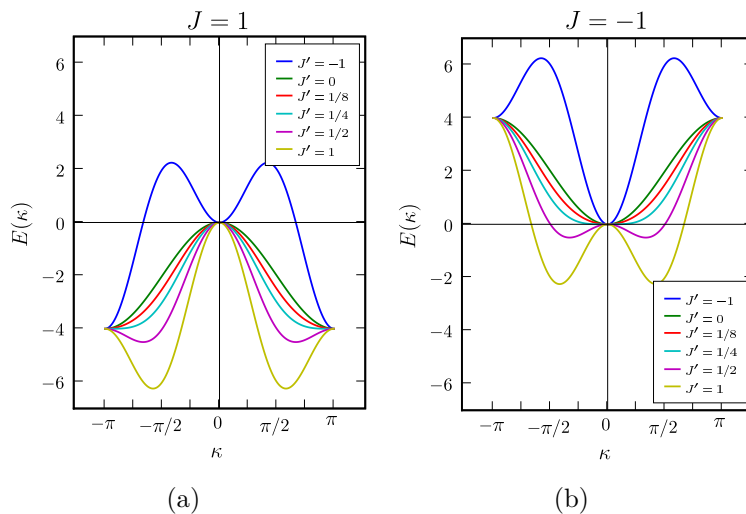
Figure 5.1: The energy dispersion in the classical limit, with (a) showing the $J > 0$ case and (b) the $J < 0$ case.

into two regions: $J'/J \geq 1/4$, and $J'/J < 1/4$. The first region corresponds to a spiral wave, where the pitch angle $\kappa = \pm\arccos\left(J'/4J\right)$; the other region is a Neél phase with fixed $\kappa = \pm\pi$. For $J < 0$, we also obtain two regions: a spiral wave phase for $J'/|J| \geq 1/4$ with $\kappa = \pm\arccos\left(J'/4|J|\right)$ and a ferromagnetic phase for $J'/|J| < 1/4$ with $\kappa = 0$.

The classical problem can be extended to take into account quantum fluctuations. The resulting model, the non-linear σ-model (NLσM), with the inclusion of the correct topological terms, correctly describes the physics of the frustrated Heisenberg chain [399–401].

5.2.2 The phase diagram

For $J' > 0$, the problem can be easily treated via bosonization [39, 45, 124]. After expressing the Hamiltonian in term of spinless fermions via the Jordan-Wigner transformation [125], the energy dispersion of the fermions reduces to

$$\varepsilon(k) = J\cos(k) + J'\cos(2k) - \mu\left(J + J'\right).$$

The effective model is a sine-Gordon model and the difference of the coupling constants $J - J'$ fixes the energy scale. We have only two cases. In the first case J' is smaller than some critical value J_H, and the cosine term flows to zero. Thus, the J' term has essentially no effect. In the second case, with $J' > J_H$, and the cosine term becomes massive and the theory gapped. The transition point, J_H, is fixed by the vanishing of the cosine term [39], and its value $J_H \approx 0.241$ can only be determined numerically [364–366, 402].
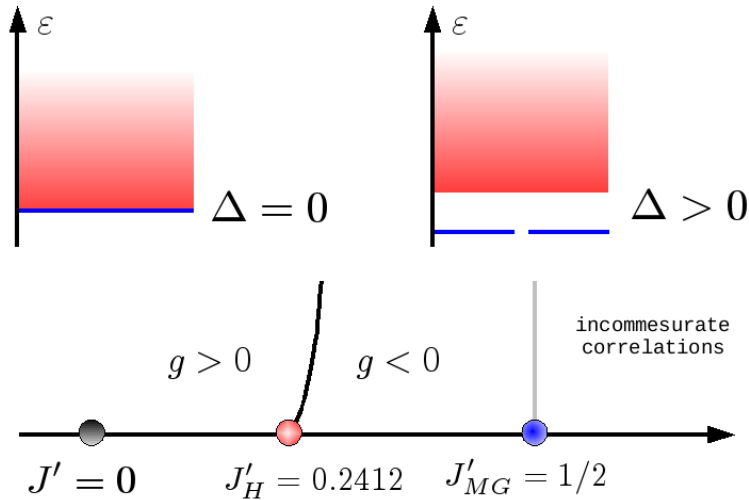
Figure 5.2: Phase diagram of the (quantum) AFM frustrated spin $1/2$ Heisenberg chain. The gap opens exponentially for $0 < J' - J'_H << 1$ and stays finite at larger values.

A sketch of the phase diagram for antiferromagnetic J is given in Fig. 5.2: for $0 < J' < J'_c$, we have a spin gapless AFM phase [318, 363] corresponding to a $c = 1$ $SU(2)_{k=1}$ WZW CFT [99, 403]. The transition point, located at J'_c, is slightly shifted with respect the classical result, $1/4$, and determines the boundary of this phase. For $J' > J'_c$, the system is gapped and dimerized. The dimerization is

confirmed by the existence of the (exact solvable) Majumdar-Ghosh (MG) point [404, 405] for $J'/J = 1/2$. Starting from the MG point, the correlation functions are characterized by incommensurate wave vectors, and this region extends to infinitely large values of J' [394]. In addition, the model represents an evident test of the Lieb-Schulz-Mattis-Affleck theorem [406–410]; in fact, it exhibits in detail the mechanism of transition through the Z_2 translation symmetry breaking (SB). As follows from the Lieb-Schulz-Mattis-Affleck theorem, a system of fermions (spin-1/2) in the thermodynamic limit has only two possibilities: to be gapless with a unique ground state and a continuum of excitations, or to be gapped with a degenerate (dimer) ground state separated from the continuous spectrum of excitations by the energy gap.

For the FM case, $J < 0$, the ground state is multi-fold degenerate and the quadratic energy dispersion, $\varepsilon \sim \omega^2$, prevents the use of bosonization. The excitation spectrum shows an instability at $J'/J = -1/4$ due to a spin flip between the state with $S^z = SL - 1$ and $S^z = SL$

$$E(\omega) = 2S\left[J\left(\cos\omega - 1\right) + J'\left(\cos 2\omega - 1\right)\right].$$

The curvature of the spectrum changes near $\omega = 0$, and the ground state is $(L+2)$-fold degenerate [397, 398]. Thus, for $J'/J < 1/4$, the ground state is in an $SU(2)$ ferromagnetic phase. On the other hand, for $J'/J > 1/4$, the system is believed to be gapless with an incommensurate pitch angle $0 < \omega < \pi/2$ [366].

Finally, we want to remark that the classical limit fails to give any hint of dimerization for $J > 0$, $J' > J'_c$; the dimer order observed in the AFM case is a purely quantum phenomena.

5.2.3 Majumdar-Ghosh point

The MG ground state wave function is a perfect dimer, i.e., the spins form singlet dimer pairs but are otherwise uncorrelated. Introducing the notation for the singlet pair

$$[i, j] = \frac{1}{\sqrt{2}}\left(|\uparrow_i\downarrow_j\rangle - |\downarrow_i\uparrow_j\rangle\right)$$

and defining (under PBC)

$$\begin{aligned}
\Phi_1(L) &= [1, 2][3, 4]\ldots[L-1, L] & (5.3)\\
\Phi_2(L) &= [2, 3][4, 5]\ldots[L, 1], & (5.4)
\end{aligned}$$

it can be shown that Φ_1 and Φ_2 are both eigenstates of the Hamiltonian with energy

$$E^{MG}(L) = -\frac{3}{8}JL.$$

This energy can be proven to be the ground state energy. Note that the matrix element $\langle \Phi_1 | \Phi_2 \rangle$ vanishes as

$$\langle \Phi_1 | \Phi_2 \rangle = (-1)^{-L/2} 2^{1-L/2} \, ,$$

so that the two states become orthogonal in the thermodynamic limit. The translation operator through one lattice constant, $T^{(1)}$, maps the two states to each other: $T^{(1)} \Phi_{1(2)} = \Phi_{2(1)}$. The symmetric and antisymmetric linear combinations of the two correspond to $\sqrt{2} \Phi^{\pm} = \Phi_1 \pm \Phi_2$, which have momentum wave vector $k = 0$ and $k = \pi$, respectively; hence, Φ^+ and Φ^- are orthogonal. Therefore, the system is characterized by a dimerized ground state with an energy gap, exponentially decaying correlation functions, and long-range dimer order in the thermodynamic limit, as predict by the Lieb-Schutz-Mattis-Affleck theorem. In fact, the two-spin correlation function, $S(i, j) = \langle \hat{S}_i^z \hat{S}_j^z \rangle$, becomes

$$S^{MG}(i, j) = \frac{1}{4} \delta_{i,j} + \frac{1}{8} \delta_{|i-j|,1}$$

and the structure function is then

$$\tilde{S}(q) = \frac{1}{4} \left(1 - \cos q \right) \, ,$$

with a peak at $q = \pi$; see Fig. 5.3. The correlation length is fixed at $\xi_{MG} = 2 / \ln 2$.
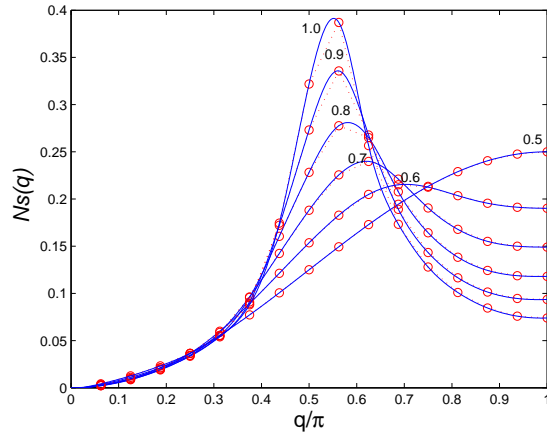

Figure 5.3: Spin structure function obtained using the DMRG. For $J'/J = 1/2$, the structure factor is exactly known to be $S(q) = \frac{1}{4}(1 - \cos q)$. After Legeza [411].

For open boundary conditions, Φ_1 and Φ_2 do not have the same energy the $[L, 1]$ bond is not present in Φ_2; thus, the energy difference is $\delta E = 3J/8$, equivalent

to surface corrections of order $1/L$. As a result, the ground state for a finite chain is not a perfect mix of the two, $\frac{1}{2}(\Phi_1 \pm \Phi_2)$, but Φ_1 is dominant. This leads to an alternating oscillation on the entropy profile that goes to zero in the thermodynamic limit. The MG model can be generalized to spin ladders or higher values of the local spin, and, using the argument of Shastry and Sutherland [412], it follows that a sufficient condition for the ground state to consist of a product of singlets on all vertical bonds is given by [413]

$$ J'/J = r \leq \begin{cases} 1/2, & \text{for} \quad S = 1/2 \\ 1/[2(S+1)] & \text{for} \quad S \geq 1 \end{cases} $$

for $S = 1/2$ spins. All excited states are strictly localized and may be identified as effective $S = 1$ spin objects. The connection between spin-1/2 ladders and spin-one chains can therefore be made using a composite spin model technique [414] or matrix product states [415].

The frustrated spin-1/2 Heisenberg chain develops incommensurate correlations for $J'/J > 0.5$ [394]. This behavior can be seen in the movement of the peak in the spin structure; see Fig. 5.3. We have found that the entropies of blocks of length $N/2$ and $N/2 + 1$, although substantially different in value due to the dimerization, both display a minimum as a function of J'/J at the Majumdar-Ghosh point [404,405], as can be seen in Fig. 5.4. On the other hand, the single-site entropy does not show any particular change when this occurs. Thus, the transition
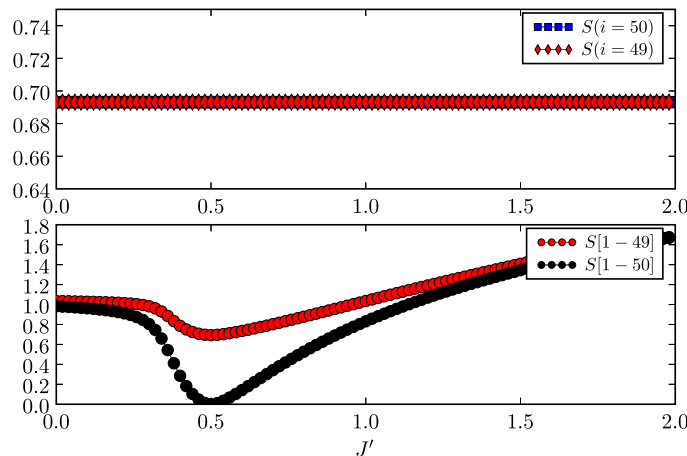
Figure 5.4: Site entropy (top) and block entropy (bottom) of the frustrated spin-1/2 Heisenberg chain of $L = 200$ sites.

from commensurate (dimerized) to incommensurate correlations is marked by the

extremum of the block entropy. However, the C-IC transition is not a *phase transition*, because the system never becomes critical. At the MG point, the wave function is highly symmetric and can be *compressed* to a few states [244] because the chain is made up of unentangled dimers.

5.2.4 Entropy analysis of the C-IC transition

In the incommensurate phase, a new peak that moves from $q = 0$ towards $q = \pi/2$ appears in the Fourier spectrum; see Fig. 5.5. When we examine the behavior of the block entropy of the lowest-lying triplet excited state, we observe two oppositely moving peaks in $\tilde{s}(q)$. One appears exactly where the peak was found
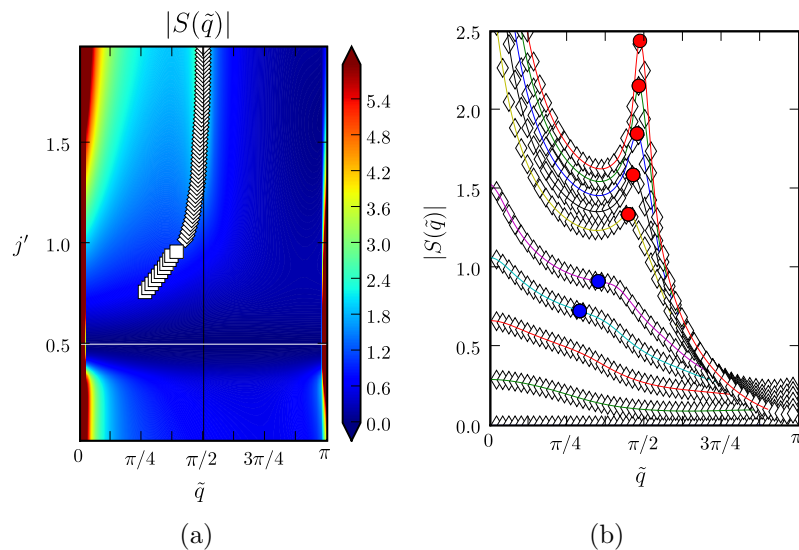
Figure 5.5: Fourier transform of the entropy profile as a function of J' and q; see Fig.(a) The diamonds are maxima and the squares are inflection points. Fig.(b) shows the Fourier transform for different value of J', where the red points are maxima and the blue points are inflection points. The system size is $L = 200$.

for the ground state, q^*, while the other occurs at $\pi - q^*$. By also calculating $S(q)$, we have found again that, to within the error of our calculation, this second peak is located at the same (J'/J-dependent) wave vector at which $S(q)$ has its maximum [366].

5.3 Bilinear-biquadratic spin one chain

The most general form for a spin-rotationally invariant two-spin coupling for a spin of magnitude S is [42]

$$\mathcal{H}_{ij} = J_1 \hat{S}_i \cdot \hat{S}_j + J_2 \left(\hat{S}_i \cdot \hat{S}_j \right)^2 + \ldots + J_{2S} \left(\hat{S}_i \cdot \hat{S}_j \right)^{2S} + \text{const}.$$

Thus, in a spin-1/2 chain, all the higher-order terms can be absorbed into a renormalized coupling J_1' (and a constant), and the physics is essentially described by the standard Heisenberg Hamiltonian. In contrast, for the $S = 1$ case, the biquadratic term cannot be expressed as any bilinear combination, and it has to be explicitly included. The resulting bilinear-biquadratic Hamiltonian is

$$\mathcal{H} = \sum_i \left[\cos\theta \left(\hat{S}_i \cdot \hat{S}_{i+1} \right) + \sin\theta \left(\hat{S}_i \cdot \hat{S}_{i+1} \right)^2 \right], \tag{5.5}$$

where the angle θ is the only relevant parameter; and the ratio of the couplings J_1 and J_2 can be expressed in terms of the cosine and the sine of θ. There are indications that strong biquadratic exchange is present in the quasi-one-dimensional compound LiVGe_2O_6 [416].

5.3.1 The AKLT point

We can rewrite the previous Hamiltonian into a different form by taking into account that the combination of two neighboring $S = 1$ spins, $\hat{S}_i$ and $\hat{S}_{i+1}$, gives rise to total spins $S_{i,i+1} = 0, 1$ and 2. The operators that project onto the three different spin subspaces are [389]

$$
\begin{aligned}
\hat{P}^0_{i,i+1} &= -\frac{1}{3} + \frac{1}{3} \left(\hat{S}_i \cdot \hat{S}_{i+1} \right)^2, \\
\hat{P}^1_{i,i+1} &= 1 - \frac{1}{2} \left(\hat{S}_i \cdot \hat{S}_{i+1} \right) - \frac{1}{2} \left(\hat{S}_i \cdot \hat{S}_{i+1} \right)^2, \\
\hat{P}^2_{i,i+1} &= \frac{1}{3} + \frac{1}{2} \left(\hat{S}_i \cdot \hat{S}_{i+1} \right) + \frac{1}{6} \left(\hat{S}_i \cdot \hat{S}_{i+1} \right)^2.
\end{aligned}
$$

We can form any possible isotropic interaction by taking a linear combination of these operators; i.e., $H = \sum_i \sum_{S=0,1,2} a_S \hat{P}^S_{i,i+1}$.

As a special case, we consider only those states for which every pair is in the $S_{i,i+1} = 2$ state [417]. Thus, the Hamiltonian may be written as

$$H = J \sum_i \left(2\hat{P}^2_{i,i+1} - \frac{2}{3} \right),$$

Figure 5.6: Phase diagram of the bilinear-biquadratic spin-one chain, represented as a polar diagram in θ.

or, in terms of spin operators, as

$$H = J \sum_i \left[\hat{S}_i \cdot \hat{S}_{i+1} + \frac{1}{3} \left(\hat{S}_i \cdot \hat{S}_{i+1} \right)^2 \right] .$$

Therefore, a state without any pair of neighbors in the $S_{i,i+1} = 2$ sector has energy $E_0 = -2/3NJ$. A such state can be obtained as follows. First, we represent each spin-one operator, $\hat{S}_i$, as the composition of two spin-1/2 operators, $\hat{\sigma}_i$ and $\hat{\tau}_i$, allowing only the symmetric combination. Then, we form singlet states between site i and $i + 1$ using one of the $1/2$-spins at each site. Finally, we notice that the action of the projection operator $\hat{P}^2$ on these states is null, and a linear combination of these states is the ground state of our Hamiltonian. Since the state consists of singlets between nearest neighbors, such models are called *valence bond solids* (VBS). The model is gapped, and the correlation length and correlation functions are

$$\xi_{\text{AKLT}} = 1/\ln 3 , \qquad \langle \hat{S}_i \hat{S}_j \rangle = (-1)^{i-j} \, 4e^{-|i-j|/\xi_{\text{AKLT}}} ,$$

respectively [418].

5.3.2 The phase diagram

The model has been studied extensively, and it shows a rather rich phase diagram. The point with $\tan \theta = 1/3$ is the AKLT point where the ground state wave function is exactly known. The points $\theta = \pi$ and $\theta = 0$ correspond to the

Heisenberg ferro- and antiferromagnet, respectively. It is firmly established that the Haldane phase with a finite spectral gap occupies the interval $-\pi/4 < \theta < \pi/4$, and the ferromagnetic state is stable for $\pi/2 < \theta < 5\pi/4$, while $\theta = 5\pi/4$ is an SU(3)-symmetric point with highly degenerate ground state [419].

An exact solution [420–422] is available for the Uimi-Lai-Sutherland (ULS) point $\theta = \pi/4$ which has SU(3) symmetry. The ULS point was shown [423] to mark the KT transition from the massive Haldane phase into a massless phase occupying the interval $\pi/4 < \theta < \pi/2$ between the Haldane and the ferromagnetic phase; this is supported by numerical studies [424].

The properties of the remaining region between the Haldane and the ferromagnetic phases are more controversial. The other Haldane phase boundary $\theta = -\pi/4$ corresponds to the exactly solvable Takhtajan-Babujian (TB) model [425, 426]; the transition at $\theta = -\pi/4$ is of the Ising type and the ground state at $\theta < -\pi/4$ is spontaneously dimerized with a finite gap to the lowest excitations [424, 427–433]. The dimerized phase extends at least up to and past the point $\theta = -\pi/2$, which has a twofold degenerate ground state and a finite gap [434–438].

There are suggestions, based on renormalization group arguments, that the region with $\theta \in [5\pi/4, \theta_c]$, where $5\pi/4 < \theta_c < 3\pi/2$, is a disordered nematic phase [439, 440]. Early numerical studies [441] apparently ruled out this possibility [442, 443]. However, more recent numerical results [444, 445] show that the existence of this region cannot be ruled out completely, and it might exist in a very narrow region.

5.3.3 Entropy analysis

The various phases and corresponding QPTs are reflected in the behavior of the site and block entropies, Fig. 5.7. The jump in the entropy at $\theta = \pi/2$ indicates a first-order transition. At $\theta = -3\pi/4$, there is only a cusp in the block entropy, but a jump in the single-entropy s indicates that this transition is first order [288]. The cusps at $\theta = -\pi/4$ and $\pi/4$ indicate second-order transitions, and the bifurcation of the entropy curves for $\ell = N/2$ and $\ell = N/2+1$ indicates that there is a spatially inhomogeneous dimerized phase between $-3\pi/4 < \theta < -\pi/4$.

Note that the entropy has a minimum at $\theta = \arctan 1/3 \simeq 0.1024\pi$, which is at the valence-bond-solid (VBS) point [417], but that it remains a continuous curve. The extremum of the entropy indicates a qualitative change in the wave function and can also signal a phase transition even if it remains a continuous curve. Such behavior has also been found in the $1/n$-filled SU(n) $n = 2, 3, 4, 5$ Hubbard model at $U = 0$, where an infinite-order (KT-like) phase transition takes place [383, 384, 446]. Since there is no sharply defined transition in the entropy, however, additional methods must be used to classify the ground state properties on either side of an extremum. One possibility is an analysis of the entropy profile
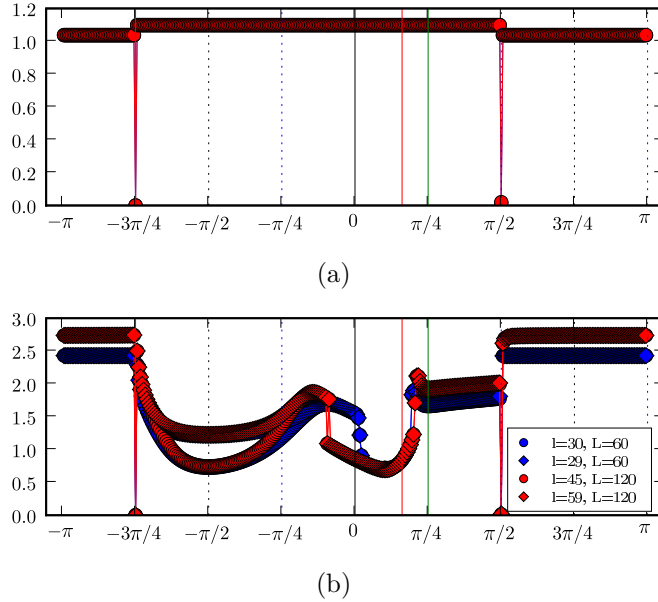
(a)

(b)

Figure 5.7: (a) Site entropy and (b) block entropy as a function of θ. The two first-order phase transitions are easily observed in the site entropy. The other transition points are seen in the block entropy. The signature of an inhomogeneous (dimerized) phase is already noticeable, between $\theta = -3\pi/4$ and $-\pi/4$, and also between $\theta = \pi/4$ and $\pi/2$.

$s(\ell)$ as the subsystem size ℓ is changed from $\ell = 0$ to N for fixed model parameters; see below.

We will first consider QPTs of the spin-one bilinear-biquadratic model [424, 441, 447] that occur at the exactly solvable Takhtajan-Babujian (TB) [425, 426] and Uimin-Lai-Sutherland (ULS) [420–422] points, corresponding to $\theta = -\pi/4$ and $\pi/4$, respectively.

As shown in Fig. 5.8, a periodic oscillation is superimposed onto a curve that is described by the analytic form given by Eq. 5.1 in both cases. At the TB point, the period of oscillation is two lattice sites, while at the ULS point it is three lattice sites. When the length l is taken to be a multiple of two for the TB point or a multiple of three for the ULS, the entropy $s(l)$ can be well-fitted using Eq. 5.1 with c approaching the known values, $c = 3/2$ [428] and $c = 2$ [423], respectively, in the limit of large N.

Except for the large positive $\tilde{s}(q = 0)$ component that grows with increasing chain length, the other components are all negative. They are shown for the two cases discussed above in Fig. 5.9. As can be seen, apart from the $q = 0$ point, the Fourier spectrum exhibits (negative) peaks at $q = \pi$ and $q = 2\pi/3$,
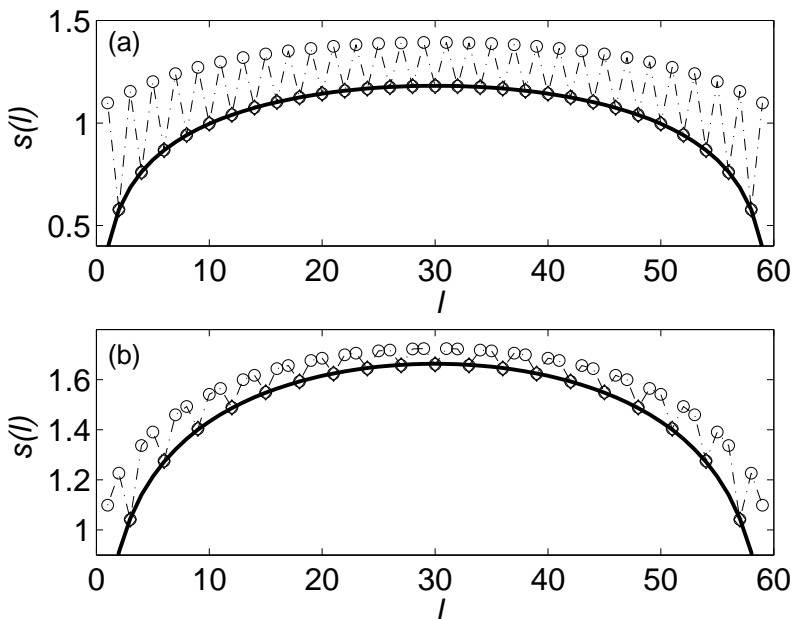
Figure 5.8: Length dependence of the von Neumann entropy of segments of length l of a finite chain with $N = 60$ sites for (a) the Takhtajan-Babujian and (b) the Uimin-Lai-Sutherland models. The solid lines are our fit using Eq. (5.1), taking every second and third data point in (a) and (b), respectively.

respectively. This is related to the fact that the TB model has two soft modes, at $q = 0$ and π, while the ULS model has three, at $q = 0$ and $\pm 2\pi/3$. Although finite-size extrapolation shows that these components vanish in the $N \to \infty$ limit, these peaks in the Fourier spectrum are nevertheless indications that the decay of correlation functions is not simply algebraic in these critical models, but that the decaying function is multiplied by an oscillatory factor. When the same calculation is performed for θ in the range $-3\pi/4 < \theta < -\pi/4$, where the system is gapped and dimerized, the peak at $q = \pi$ remains finite as $N \to \infty$. On the other hand, in the whole interval $\pi/4 \leq \theta < \pi/2$, where the system is gapless and the excitation spectrum is similar to that at the ULS point, the entropies for block sizes that are multiples of three can be well-fitted with the form given in Eq. 5.1 with $c = 2$, and for finite chains, a peak appears in $\tilde{s}(q)$ at $q = 2\pi/3$, in agreement with Refs. [424,441,447] and [423]. Thus, peaks in the Fourier spectrum of the length-dependent block entropy can provide useful information about the excitation spectrum and the wave vector of soft modes, even when they scale to zero in the thermodynamic limit.
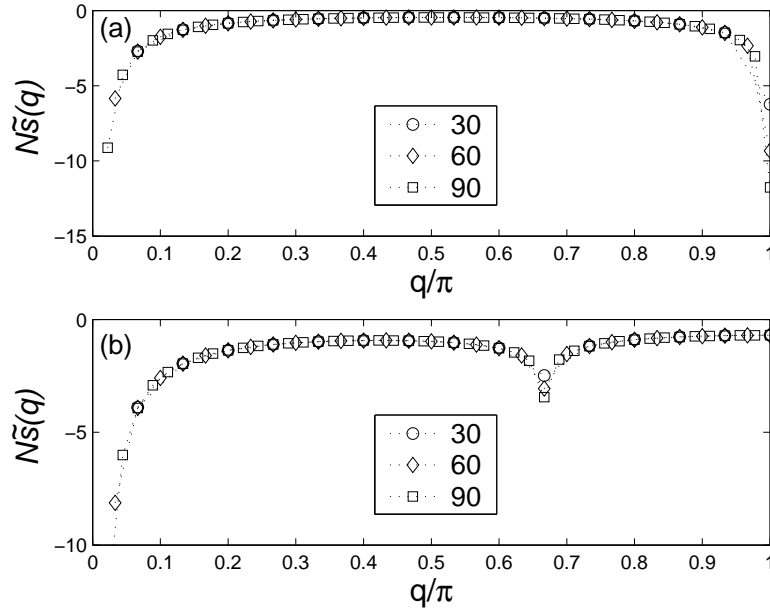
Figure 5.9: Fourier spectrum $\tilde{s}(q)$ (scaled by the system size N) of the length-dependent von Neumann entropy of finite chains of length $N = 30, 60$ and 90 for (a) the Takhtajan-Babujian and (b) the Uimin-Lai-Sutherland models.

We can also demonstrate this procedure near the AKLT point [417], corresponding to $\theta_{\mathrm{AKLT}} = \arctan 1/3 \simeq 0.1024\pi$. It is known [448] that this point is a disorder point, where incommensurate oscillations appear in the decaying correlation function; however, the shift of the minimum of the static structure factor appears only at a larger $\theta_{\mathrm{L}} = 0.138\pi$, the so-called Lifshitz point. In earlier work [288], some of us showed that $s(N/2)$ has an extremum as a function of θ at θ_{AKLT}. Here we show that this extremum is the indication that, in fact, θ_{AKLT} is a dividing point which separates regions with a different behavior of $s(l)$ and $\tilde{s}(q)$.

At and below the AKLT point, i.e., for $-\pi/4 < \theta \leq \theta_{\mathrm{AKLT}}$, $s(l)$ increases with l for small l, saturates due to the Haldane gap [449], and then goes down to zero again as l approaches N. The Fourier spectrum $\tilde{s}(q)$ is a smooth function of q (except for the $q = 0$ component). The transformed entropy $\tilde{s}(q)$ at the AKLT point, depicted in Fig. 5.10, illustrates this behavior. For θ slightly larger than θ_{AKLT}, however, we find that $s(l)$ does not increase to the saturation value purely monotonically. Instead, an incommensurate oscillation is superimposed. For somewhat larger θ values, $\theta > 0.13\pi$, this oscillation persists in the saturated region, i.e., for blocks much longer than the correlation length. This leads to a new (negative) peak in $\tilde{s}(q)$ which moves from small q towards $q = 2\pi/3$ as

the ULS point is approached, and gets larger and narrower, as can be seen in Fig. 5.10. This θ value is slightly smaller than, but close to, the Lifshitz point. It is also interesting to examine the behavior of the block entropy in the lowest-
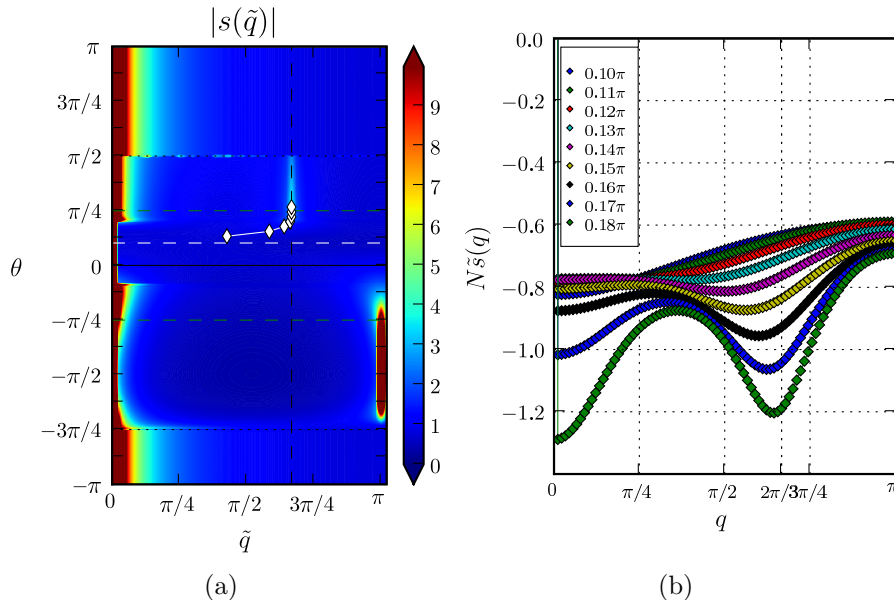

(a)

(b)

Figure 5.10: Fourier transform of the entropy profile as a function of θ and q. In (a), the white line delineates the AKLT point and the white points indicate incommensurate peaks seen explicitly in (b). The system size is $L = 120$.

lying excited state. Since, according to the AKLT picture [417], there are effective spin-1/2 degrees of freedom at the end of the open chain. In the limit of a long chain, the ground state is four-fold degenerate. Therefore, the first interesting excitation is the quintet, which corresponds to the Haldane gap [450–452]. In fact, the triplet behaves in a similar fashion as the ground state, where the system is gapped, the entropy profile saturates to a constant value for sub-systems bigger than the correlation length. For $\theta \to \pi/4$, the system approaches the ULS critical point. As we can see in Fig. 5.11, since only the larger sub-system can include a growing correlation length, the constant central part of the entropy profile becomes narrower and narrower. When $\xi > L$, the finite system behaves pseudo-critically and, since there are OBC, the oscillations of the entropy profile are related to the wave vector pinned to the edges.

The situation is different for the quintet. The entropy profile for a gapped system is basically a Gaussian centered in the middle of the chain. An oscillating term is superimposed on the Gaussian curve once the incommensurability appears. This
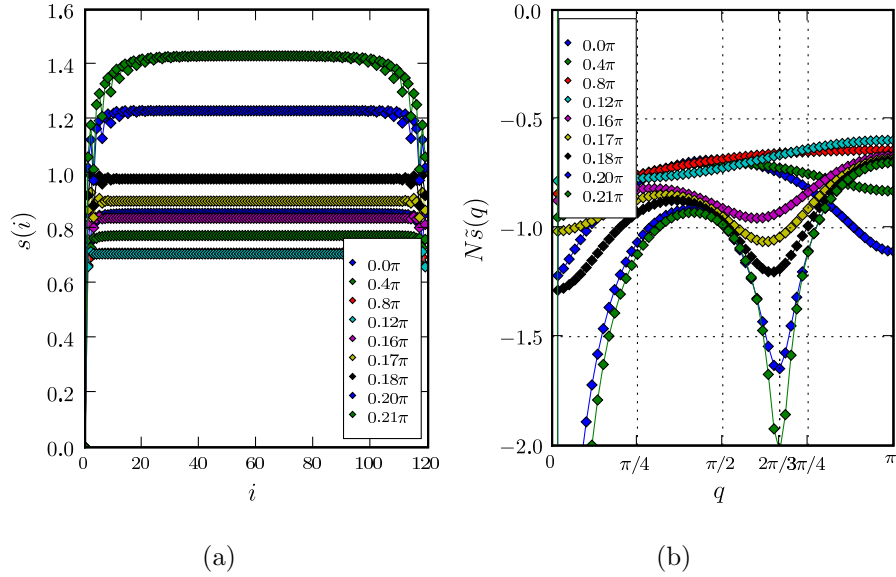
Figure 5.11: (a) Entropy profile and its Fourier transform. (b) same as Fig. 5.10 (b) but showing the $S^z_{\mathrm{Tot}} = 1$ triplet excited state.

translates to a moving (negative) peak in the Fourier transform corresponding to the incommensurate wave vector. However, when we move close the ULS critical point, the character of criticality becomes more relevant. This is seen in the Fourier-transformed representation, $\tilde{s}(q)$, in Fig. 5.12 for several θ values. The appearance of the new peaks are even more pronounced, and data for $\theta < \theta_{\mathrm{L}}$ confirm that this approach can probe the incommensurate phase much closer to the transition point than is possible using only the static structure factor $S(q)$. Although the new peak(s) in $\tilde{s}(q)$ in the incommensurate phase move in an opposite sense to those in $S(q)$ (see Ref. [394]), i.e., the peak approaches $2\pi/3$ from zero and not from π, they can be easily related to each other. By also calculating $S(q)$, we have found, to within the error of our calculation, that the location, q^*, of the peak in $\tilde{s}(q)$ is related to the wave vector q at which $S(q)$ has its maximum by $q = \pi - q^*/2$.

5.4 The $t - t' - U$ Hubbard model

In the previous section, we have demotrated the usefulness of studying the entropy profile for models where the quantum critical points are known. We now turn to

(a)   (b)
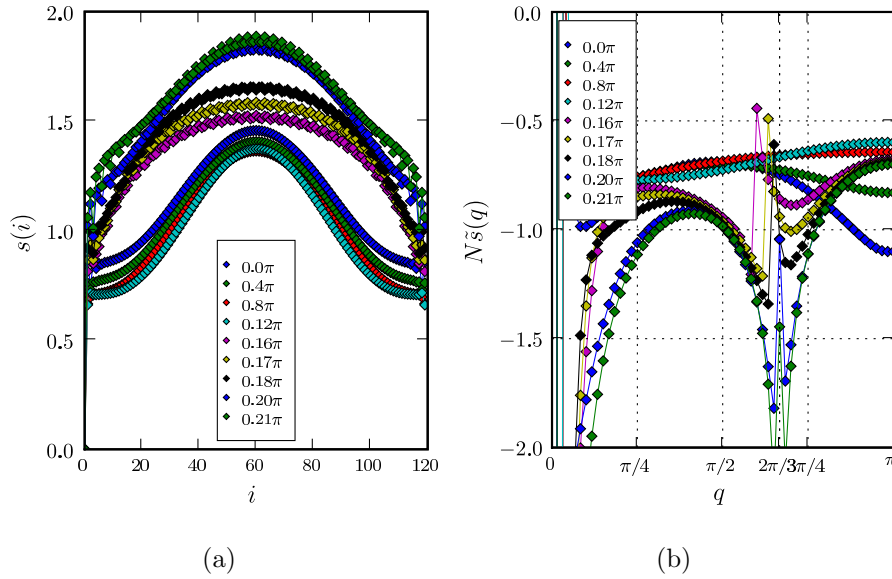
Figure 5.12: Same as Fig. 5.11, but for the $S^z_{\rm Tot} = 2$ quintet excited state.

the commensurate-incommensurate transition in the 1D $t - t' - U$ Hubbard model

$$
\begin{aligned}
\mathcal{H} = {} & t \sum_{i\sigma} \left(c^{\dagger}_{i\sigma} c_{i+1\sigma} + c^{\dagger}_{i+1\sigma} c_{i\sigma} \right) \\
& + t' \sum_{i\sigma} \left(c^{\dagger}_{i\sigma} c_{i+2\sigma} + c^{\dagger}_{i+2\sigma} c_{i\sigma} \right) + U \sum_{i} n_{i\uparrow} n_{i\downarrow} \, ,
\end{aligned}
\tag{5.6}
$$

which has been investigated in the previous chapter and recently in Ref. [453]. For the half-filled case (and setting $t = 1$), the competition between t' and the Coulomb energy U will determine whether the system is an insulator ($t' < t'_{\rm c}$) or a metal ($t' > t'_{\rm c}$). For finite U values, this transition is preceded by the opening of a spin gap at $t'_{\rm s} < t'_{\rm c}$. Between $t'_{\rm s}$ and $t'_{\rm c}$, the wave vector becomes incommensurate for $t' > t'_{\rm IC}$. Thus, the commensurate-incommensurate transition is independent of the metal-insulator transition; see Ch.4 and Ref. [453].

As expected for a commensurate-incommensurate transition, we find that the entropy of blocks of length $N/2$ display an extremum as a function of t'. For very large U values, where the model is equivalent to the frustrated spin-1/2 Heisenberg chain, the extremum occurs at $t'_{\rm IC} \simeq 1/\sqrt{2}$, which maps to the Majumdar-Ghosh point. The block entropy is shown in Fig. 5.14 (a) for $U = 3$, a value chosen so that our results can be directly compared to those of the previous chapter. Compare Fig. 4.7 and Fig. 5.14 (b), for example. This shows that the transition point can accurately be detected and located on system sizes that are typically a factor of two to four smaller than those needed with the standard methods used in Ref. [453].
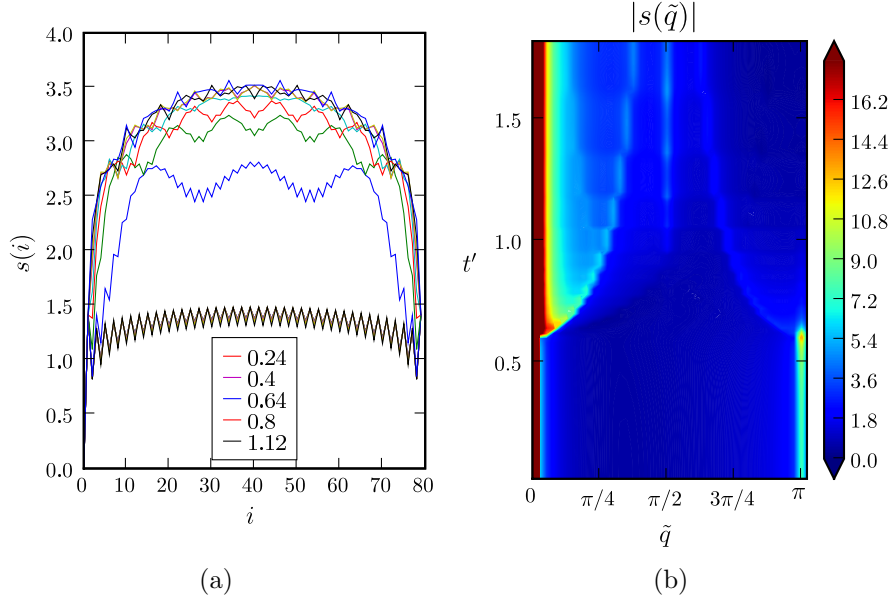
Figure 5.13: (a) Block entropy profile for different values of t' and (b) its Fourier transformation. The system size is $L = 80$.

For $t' > 0.6$, an incommensurate oscillation in $s(l)$ becomes apparent, as well as in its Fourier-transformed representation, $\tilde{s}(q)$. When $\tilde{s}(q)$ is analyzed, it is found that a new peak appears in the spectrum and again moves from small q towards $q = \pi/2$ with the amplitude of $\tilde{s}(\pi)$ decreasing with increasing t'. Therefore, the commensurate-incommensurate phase boundary can be easily determined by finding the extrema of $s(N/2)$ as a function of t' for various U values. This phase boundary is depicted in Fig. 5.14(b).

5.5 Discussion

In conclusion, we have shown that the length dependence of the block entropy and its Fourier spectrum, determined for finite systems, can be used to characterize phases in which the correlation function has an oscillatory character. This method also provides significant information about some features of the excitation spectrum and allows one to identify soft modes in critical models. In addition, an extremum in the block entropy as a function of the relevant model parameter, which, in general, signals the appearance of or change in a symmetry in the wave function, can also correspond to disorder points. In this case, however, the entropy curve does not show anomalous behavior because this is not a phase transition in the conventional sense. When the decaying correlation function has an incommen-
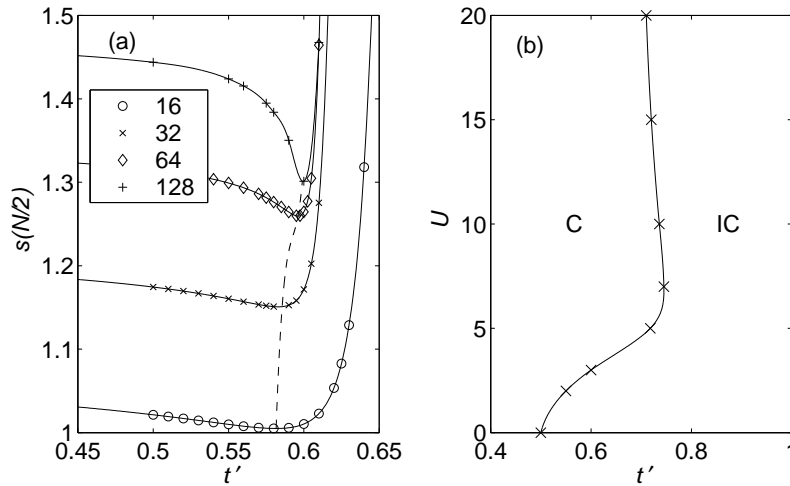
Figure 5.14: (a) Entropy of blocks of length $N/2$ as a function of t' for the 1D $t - t' - U$ Hubbard model for $U = 3$ and various chain lengths. The dashed line is a spline through the minima. (b) Phase boundary of commensurate-incommensurate transition in the t'-U plane obtained from a finite-size extrapolation of the minima in (a). The line is a spline through the indicated points.

surate oscillation, a new peak appears close to $q = 0$ in the Fourier spectrum and moves towards a commensurate wave vector as the control parameter is adjusted. In the entropy of the spin-excited states, another peak can appear at the wave vector of the peak in the static structure factor, in addition to a peak at the same position as in the ground-state entropy.

Conclusion

In this thesis, we have explored the properties of quantum phase transitions in quasi one-dimensional systems using the DMRG, quantum information theory, and quantum field theory. We have applied these techniques to the band-insulator to Mott-insulator transition that occurs in the charge-transfer complexes, to the Mott metal-insulator transition influenced by a commensurate-incommensurate phase transition, and to different types of homogeneous-inhomogeneous transitions. Our main findings are contained in chapters 3, 4 and 5.

In chapter 3, we have investigated the nature of the band-insulator to Mott-insulator transition. We have found that the presence of a spontaneously dimerized phase between these two very different insulators is a quite generic feature. While such a scenario was already proposed a few years ago using arguments from bosonization and field theory, existing numerical results did not provide a complete and unambiguous picture of the details of the transition. Using the effective model, we have been able to calculate the critical exponents of the quantum phase transition using the DMRG and finite-size scaling analysis. This work supplies a clear answer to this issue. Using an effective model that contains only the degrees of freedom relevant to the transition rather than the original model has made it possible to determine the critical properties with greater precision and to understand the relevant energy scale. Note that the truncation and mapping scheme is fairly general and can potentially be applied to other models.

In chapter 4, we have studied the Mott metal-insulator transition in the $t - t'$ Hubbard model. First, we have derived an expression for the critical line separating the metallic phase from the spin-gapped insulator. We have also used the DMRG to perform a comprehensive calculation of the relevant quantities. In particular, we have calculated the gap, the density, and the momentum-space distributions in the spin and charge sectors. These results provide new insights into the Mott metal-insulator transition. In particular, the numerical results support the suggestion that the standard theory of the commensurate-incommensurate transition is the relevant effective theory to describe the Mott metal-insulator transition in the $t - t'$ Hubbard model.

In chapter 5, we have used the length-dependence of the block entropy to characterize inhomogeneous phases. In particular, we have concentrated on the quantum homogeneous-inhomogeneous transition. We have been able to identify the dimerized and the trimerized phases by examining the behavior of the peaks of the

Fourier transform of the entropy profile. Finally, we have applied the method to a model which has not previously been investigated with quantum information entropy, the $t - t'$ Hubbard model.

Our results contribute to the understanding of quantum phase transitions in one-dimensional strongly correlated systems and indicate new directions for further investigation. We have used different methods to investigate quantum phase transitions and extract information from the simulation. First, we have used finite-size scaling of charge gaps, spin gaps, order parameters and relative susceptibility to extract the critical properties, i.e., critical exponents. Second, we have used measures of quantum information based on the von Neumann entropy to find critical points and to extract the central charge. Although the two methods yield different quantities in detail, both the exponents and the central charge can be used to classify the universality class of the critical behavior. The two methods have different advantages and limitations. The finite-size scaling analysis works for any kind of transition and can be applied to both critical and non-critical phases. However, such simulations become very expensive in critical regions because physical quantities must be calculated in both ground and excited states. In addition, there are models in which the fluctuations in the finite-size scaling are so strong that the behavior in the thermodynamic limit cannot determined. On the other hand, quantum information quantities are ground state measures that are generated as a natural by-product of the DMRG procedure. However, a full characterization of the critical properties is possible only under the condition that the effective theory is conformally invariant. For many situations, the two methods can be used in combination: preliminary simulations can use anomalies in the entropy to indicate the presence of transition points or inhomogeneous phases. A careful finite-size analysis can then be used to characterize the transition completely.

Due to the rapid progress that has occurred in the use of the quantum information theory in strongly correlated systems recently, there are many possibilities for further research in the direction of this thesis. Therefore, we would like to conclude by giving a short outlook. In particular, it would be interesting to extend the DMRG algorithm by making direct use of matrix product or tensor product states. There have been a number of different proposals for such algorithms [306, 454–459] but it is not yet clear which ones are most effective for different problems. These states have the potential to perform better than the DMRG in high dimensional lattices. However, the entropy area law (see chapter 2) may provide an essential limitation to the scaling of the computational effort with dimension. Algorithms based on tensor product states can at least potentially reach this limit. Algorithms based on matrix product states can also include the effects of finite temperature or treat full time evolution [460, 461].

Another fundamental problem that we have encountered in this thesis is how

to better approach the thermodynamic limit for systems with strong finite-size fluctuations. In particular, it would be useful to be able to test the convergence of a physical quantity to the thermodynamic value by varying the boundary conditions or including an infinite bath. This would avoid the need to carry out careful finite-size scaling to such large system sizes, which is computationally quite costly.

There are also many interesting physical questions yet to be addressed. In order to describe materials more realistically, more general models than the ones studied here are often necessary. Some additional elements of the actual band structure of a material, such as more realistic dispersion or multiple bands can be included. In one dimension, it is often important to go beyond the on-site Coulomb interaction considered in this thesis; the long-range part can be important, especially in non-metallic phases. Another important element to take into account are phonons, which lead to an additional interaction for the electrons and can significantly influence the behavior of the system. In particular, instabilities to lattice distortion are especially important in one dimension. While adding such contributions makes models more realistic, it complicates the simulations and increases their computational difficulty. However, improvements in the algorithms and in computer capacity as well as a growing understanding of the simpler models, make such extensions both necessary and possible. Finally, it should be mentioned that recent experimental developments in nanoscopic systems have opened up new classes of systems to study. Examples include quantum dots, spintronic devices, and arrays of Josephson junctions as well as cold atoms on optical lattices.

Conclusion

132

Acknowledgments

My adventure started many years ago and during the time I spent in Italy, Switzerland, Germany and Hungary, I had the pleasure to meet and to work with extraordinary people. I would like to acknowledge them all. Thanks!

I am in particular grateful to Prof. Dr. Reinhard Noack for his unconditional support during the last years. I would like to thank Prof. George Japaridze, Dr. Örs Legeza, Dr. Gábor Fáth, Prof. Jeno Sólyom, Prof. Florian Gebhard and Prof. Dionys Baeriswyl for having such a fruitful collaboration. I would like to mention Prof. Cris Hamer for providing me valuable information. I would like to express my gratitude to Dr. E. Ercolessi, Prof. Dr. P. Pieri, Prof. G. Morandi, Prof. Dr. F. Ortolani, Dr. C. Del Boschi, Dr. M. Roncaglia for the initial support.

Special thanks to Alessandro Tricoli and Lorenzo Frassinetti my friends for been always present despite the long distance. I would like to thank Lisa Bartoli. I wish to thank Bruce Normand, Marc Görbig, Andrea Capocci, Lara Benfatto, Holger Benthien, Joerg Rissler, Joerg Bueneman, Anja Grage, Salvatore Manmana and, in particular my friends Vladimir Juricic, Vladimir Gritsev, Giancarlo Mosetti and Fabio Mariotti. Special thanks to Paolo Laureti and Satoshi Ejima for being very good friends. Thanks, Merci, Gracias, Danke, Grazie a Claudia Hurtado. I would also like to thank Frau von-den-Bergen and Marina Koch who helped me. I acknowledge the International Research Training Group *Electron-Electron Interactions in Solids* (Marburg–Budapest) for my fellowship and giving me the opportunity to meet professionals in the field. There are a lot of people, who indirectly contributed to this thesis filling my life with happiness and pleasure. Without the help and support of the people around me, this thesis would not have been completed. Thanks!

Last, but not least, I would like to thank my Father, my Mother and my Sister for their love, which became stronger and stronger over the time and the distance.

Conclusion

Bibliography

[1] Anderson, P. W. *Science* **177**, 393 (1972).

[2] Laughlin, R. B. and Pines, D. *Proc. Nat. Acad. Sci.* **97**, 28 (2000).

[3] Chaikin, P. M. and Lubensky, T. C. *Principles of condensed matter physics.* Cambridge University Press, (1995).

[4] Ashcroft, N. W. and Mermin, N. D. *Solid state physics.* Brooks Cole, (1976).

[5] Phillips, P. *Advanced solid state physics.* Westview, (2003).

[6] Born, M. and Oppenheimer, J. R. *Ann. d. Physik* **84**, 457 (1927).

[7] Hoenberg, P. and Kohn, W. *Phys. Rev. B* **136**, 864 (1964).

[8] Parr, R. G. and Yang, W. *Density Functional Theory of Atoms and Molecules.* Oxford University Press, (1963).

[9] Kohn, W. *Rev. Mod. Phys.* **71**, 1253 (1999).

[10] Tremplay, A. M. S., Bourbonnais, C., and Sénéchal, D. cond-mat/0005111, (2000).

[11] Kopietz, P., Meden, V., and Schönhammer, K. *Phys. Rev. Lett.* **74**, 2997 (1995).

[12] Kopietz, P., Meden, V., and Schönhammer, K. *Phys. Rev. B* **56**, 7232 (1997).

[13] Biermann, S., Georges, A., Lichtenstein, A., and Giamarchi, T. *Phys. Rev. Lett.* **87**, 276405 (2001).

[14] Coleman, P. *Physica B* **378**, 1160 (2006).

[15] Dagotto, E. *Science* **309**, 257 (2005).

[16] Fulde, P., Thalmeier, P., and Zwicknagl, G. cond-mat/0607165, (2006).

[17] von Löhneysen, H. *Physica B* **378**, 1170 (2006).

Bibliography

[18] Dowlind, J. P. and Milburn, G. J. *Phil. Trans. R. Soc. Lond. A* **361**, 1655 (2003).

[19] Saito, G. and Yoshida, Y. *Bull. Chem. Soc. Jpn.* **80**, 1 (2007).

[20] Jérome, D. and Schultz, H. J. *Adv. in Phys.* **31**, 299 (1982).

[21] Heeger, A. J., Kivelson, S., Schrieffer, J. R., and Su, W. P. *Rev. Mod. Phys.* **60**, 781 (1988).

[22] Torrance, J. B., Vazquez, J. E., Mayerle, J. J., and Lee, V. Y. *Phys. Rev. Lett.* **46**, 253 (1981).

[23] von Helmolt, R., Wecker, J., Holzapfel, B., Schultz, L., and Samwer, K. *Phys. Rev. Lett.* **71**, 2331 (1993).

[24] Ramirez, A. P. *J. Phys. C: Solid State Phys.* **9**, 8171 (1997).

[25] Bednorz, J. G. and Müller, K. A. *Zeitschrift für Physik B Condensed Matter* **64**, 189 (1986).

[26] Chakravarty, S. *Science* **319**, 735 (2008).

[27] Lee, P. A., Nagaosa, N., and Wen, X.-G. *Rev. Mod. Phys.* **78**, 17 (2006).

[28] Wolf, S. A., Awschalom, D. D., Buhrman, R. A., Daughton, J. M., von Molnár, S., Roukes, M. L., Chtchelkanova, A. Y., and Treger, D. M. *Science* **294**, 1488 (2001).

[29] Feynman, R., Allen, R. W., Hey, T., and Hey, A. J. G. *Feynman Lectures on Computation.* Perseus publishing, (2001).

[30] Burkard, G. cond-mat/0409626, (2004).

[31] Fradkin, E. *Field theories of condensed matter systems.* Addison Wesley, (1991).

[32] Auerbach, A. *Interacting electrons and quantum magnetism.* Springer-Verlag, (1994).

[33] Fulde, P. *Electron correlations in molecules and solids.* Springer, (1995).

[34] Schulz, H. J., Cuniberti, G., and Pieri, P. cond-mat/9807366, (1998).

[35] Schofield, A. J. *Contemp. Phys.* **40**, 95 (1999).

[36] Bose, I. cond-mat/0107399, (2001).

[37] Varma, C. M., Nussinov, Z., and van Saarloos, W. *Phys. Rep.* **361**, 267 (2002).

[38] Voit, J. *Rep. Prog. Phys.* **58**, 977 (1995). cond-mat/9510014.

[39] Giamarchi, T. *Quantum Physics in One Dimension*. Cambridge University Press, (2004).

[40] Essler, F. H. L., Frahm, H., Göhmann, F., Klümper, A., and Korepin, V. E. *The One-Dimensional Hubbard Model*. Cambridge University Press, (2005).

[41] Gebhard, F. *The Mott Metal–Insulator Transition*. Springer, (1997).

[42] Fazekas, P. *Lecture Notes on Electron Correlation and Magnetism*. World Scientific, (1999).

[43] White, R. M. *Quantum Theory of Magnetism*. Springer, (2006).

[44] Lhuillier, C. cond-mat/0502464, (2005).

[45] Tsvelik, A. M. *Quantum Field Theory in Condensed Matter Physics*. Cambridge University Press, (2003).

[46] White, S. R. *Phys. Rev. Lett.* **69**, 2863 (1992).

[47] White, S. R. *Phys. Rev. B* **48**, 10345 (1993).

[48] Sachdev, S. *Quantum Phase Transition*. Cambridge University Press, (2001).

[49] Galindo, A. and Martin-Delgado, M. A. *Rev. Mod. Phys.* **74**, 347 (2002).

[50] Landau, L. D. *Collected papers of L. D. Landau*. Gordon and Breach, (1965).

[51] Landau, L. D. and Lifshitz, L. M. *Statistical physics, part one*. Pergamon Press, (1980).

[52] Goldenfeld, N. *Renormalization group in critical phenomena*. Addison Wesley, (1994).

[53] Cardy, J. *Scaling and renormalization in statistical physics*. Cambridge University Press, (1996).

[54] Yeomans, J. M. *Statistical mechanics of phase transitions*. Oxford University Press, (1992).

[55] Onsager, L. *Phys. Rev.* **65**, 117 (1944).

Bibliography

[56] Ising, E. *Z. Physik* **31**, 235 (1925).

[57] Yang, C. N. *Phys. Rev.* **85**, 808 (1952).

[58] Fisher, M. E. *Rep. Prog. Phys.* **30**, 615 (1967).

[59] Kadonoff, L. P., Götze, W., Hamblen, D., Hecht, R., Lewis, E. A. S., Palci-auskas, V. V., Rayl, M., Swift, J., Apsens, D., and Kane, J. *Rev. Mod. Phys.* **39**, 395 (1967).

[60] de Gennes, P. G. *Scaling concepts in polymer physics.* Cornell University Press, (1979).

[61] Wilson, K. G. and Kogut, J. *Phys. Rep.* **12**, 77 (1974).

[62] Fisher, M. E. *Rev. Mod. Phys.* **70**, 653 (1998).

[63] Zinn-Justin, J. *Quantum field theory and critical phenomena.* Oxford University Press, (1996).

[64] Amit, D. J. *Field theory, the renormalization group and critical phenomena.* McGraw-Hill, (1984).

[65] Hohenberg, P. C. and Halperin, B. I. *Rev. Mod. Phys.* **49**, 435 (1977).

[66] Vojta, M. *Rep. Prog. Phys.* **66**, 2069 (2003).

[67] Pelissetto, A. and Vicari, E. *Phys. Rep.* **368**, 549 (2002).

[68] Belitz, D., Kirkpatrik, T. R., and Vojta, T. *Rev. Mod. Phys.* **77**, 579 (2005).

[69] Senthil, T., Vishwanath, A., Balents, L., Sachdev, S., and Fisher, M. P. A. *Science* **303**, 1490 (2004).

[70] Stewart, G. R. *Rev. Mod. Phys.* **73**, 797 (2001).

[71] Vojta, M. *Phil. Mag.* **86**, 1807 (2006).

[72] Barber, M. N. volume 8 of *Phase Transition and Critical Phenomena*, chapter 2. (1983).

[73] Ballentine, C. A., Fink, R. L., Araya-Pochet, J., and Erskine, J. L. *Phys. Rev. B* **41**, 2631 (1990).

[74] Lederman, D., Ramos, C. A., Jaccarino, V., and Cardy, J. L. *Phys. Rev. B* **48**, 8365 (1993).

[75] Elmers, H. J., Hauschild, J., Höche, H., Gradmann, U., Bethge, H., Heuer, D., and Köhler, U. *Phys. Rev. Lett.* **73**, 898 (1994).

[76] Ambrose, T. and Chien, C. L. *Phys. Rev. Lett.* **76**, 1743 (1996).

[77] Mehta, S. and Gasparini, F. M. *Phys. Rev. Lett.* **78**, 2596 (1997).

[78] Lipa, J. A., Swanson, D. R., Nissen, J. A., Geng, Z. K., Williamson, P. R., Stricker, D. A., Chui, T. C. P., Israelsson, U. E., and Larson, M. *Phys. Rev. Lett.* **84**, 4894 (2000).

[79] Koma, T. and Tasaki, H. *J. Stat. Phys.* **76**, 745 (1994).

[80] Kogut, J. B. *Rev. Mod. Phys.* **51**, 659 (1979).

[81] Glaus, U. and Schneider, T. *Phys. Rev. B* **30**, 215 (1984).

[82] Sorensen, E. S. and Affleck, I. *Phys. Rev. B* **49**, 15771 (1994).

[83] White, S. R., Affleck, I., and Scalapino, D. J. *Phys. Rev. B* **65**, 165122 (2002).

[84] Hamer, C. J. and Barber, M. N. *J. Phys. A: Math. Gen.* **13**, L169 (1980).

[85] Hamer, C. J. and Barber, M. N. *J. Phys. A: Math. Gen.* **14**, 259 (1981).

[86] den Nijs, M. and Rommelse, K. *Phys. Rev. B* **40**, 4709 (1989).

[87] Misguich, G., Serban, D., and Pasquier, V. *Phys. Rev. Lett.* **89**, 137202 (2002).

[88] Furukawa, S., Misguich, G., and Oshikawa, M. *Phys. Rev. Lett.* **96**, 047211 (2006).

[89] Kitaev, A. and Preskill, J. *Phys. Rev. Lett.* **96**, 110404 (2006).

[90] Levin, M. and Wen, X.-G. *Phys. Rev. Lett.* **96**, 110405 (2006).

[91] Kosterlitz, J. M. and Thouless, D. *J. Phys. C: Solid State Phys.* **6**, 1181 (1973).

[92] Kosterlitz, J. M. *J. Phys. C: Solid State Phys.* **7**, 1046 (1974).

[93] Kenna, R. and Irving, A. C. *Nucl. Phys. B* **485**, 583 (1997).

[94] Berche, B. *J. Phys. A: Math. Gen.* **36**, 585 (2003).

Bibliography

[95] Baxter, R. J. *Exactly solved models in statistical mechanics.* Accademic Press, (1982).

[96] Korepin, V. E., Bogoliubov, N. M., and Izergin, A. G. *Quantum inverse scattering method and correlation functions.* Cambridge University Press, (1993).

[97] Schulz, H. J. cond-mat/9503150, (1995).

[98] Di Francesco, P., Mathieu, P., and Sénéchal, D. *Conformal field theory.* Springer-Verlag, (1997).

[99] Affleck, I., Gepner, D., Schultz, H. J., and Ziman, T. *J. Phys. A: Math. Gen.* **22**, 511 (1989).

[100] Henkel, M. *Conformal Invariance and Critical Phenomena.* Springer, (1999).

[101] Kolomeisky, E. B. and Straley, J. P. *Rev. Mod. Phys.* **68**, 175 (1996).

[102] Abrikosov, A. A., Gorkov, L. P., and Dzyaloshinskii, I. E. *Methods of Quantum Field Theory in Statistical Mechanics.* Dover, (1963).

[103] Nozíres, P. *Interacting Fermi Systems.* Westview Press, (1964).

[104] Negele, J. F. and Orland, H. *Quantum Many-Particle Systems.* Westview Press, (1988).

[105] Hewson, A. C. *Adv. Phys.* **43**, 543 (1994).

[106] Froehlich, J., Studer, U. M., and Thiran, E. cond-mat/9508062, (1995).

[107] Froehlich, J., Chen, T., and Seifert, M. cond-mat/9508063, (1995).

[108] Luttinger. *J. Mat. Phys.* **4**, 1154 (1963).

[109] Sólyom, J. *Adv. Phys.* **28**, 201 (1979).

[110] Haldane, F. D. M. *J. Phys. C: Solid State Phys.* **12**, 4791 (1979).

[111] Haldane, F. D. M. *J. Phys. C: Solid State Phys.* **14**, 2585 (1981).

[112] Haldane, F. D. M. *Phys. Rev. Lett.* **45**, 1358 (1980).

[113] Haldane, F. D. M. *Phys. Rev. Lett.* **47**(25), 1840 (1981).

[114] Haldane, F. D. M. *J. Phys. C: Solid State Phys.* **14**, 2585 (1981).

[115] Haldane, F. D. M. *Phys. Lett. A* **81**, 153 (1981).

[116] Dzyaloshinskii, I. E. and Larkin, A. I. *Zh. Eksp. Teor. Fiz.* **65**, 411 (1973).

[117] Everts, H. U. and Schulz, H. *Solid State Commun.* **15**, 1413 (1974).

[118] Metzner, W. and Di Castro, C. *Phys. Rev. B* **47**, 16107 (1993).

[119] Metzner, W., Castellani, C., and Di Castro, C. *Adv. Phys.* **47**, 317 (1998).

[120] Rezayi, E. H., Sak, J., and Talukdar, S. *Phys. Rev. B* **19**, 4757 (1979).

[121] Tomonaga, S. *Progress in Theoretical Physics* **5**, 544 (1950).

[122] Matthis, D. C. and Lieb, E. H. *J. Mat. Phys.* **6**, 304 (1965).

[123] Luther, A. and Peschel, I. *Phys. Rev. B* **9**, 2911 (1974).

[124] Gogolin, A. O., Nersesyan, A. A., and Tsvelik, A. M. *Bosonization and Strongly Correlated Systems*. Cambridge University Press, (1998).

[125] Jordan, P. and Wigner, E. *Z. Phys.* **47**, 631 (1928).

[126] Polychronakos, A. P. cond-mat/9902157, (1999).

[127] Batista, C. D. and Ortiz, G. *Phys. Rev. Lett.* **86**, 1082 (2001).

[128] Batista, C. D. and Ortiz, G. *Adv. in Phys.* **53**, 1 (2004).

[129] Bourbonnais, C. and Caron, L. G. *Int. J. Mod. Phys. B* **5**, 1033 (1991).

[130] Shankar, R. *Rev. Mod. Phys.* **66**, 129 (1994).

[131] Salmhofer, M. *Comm. Math. Phys.* **194**, 249 (1998).

[132] Salmhofer, M. and Honerkamp, C. *Prog. Theor. Phys.* **105**, 1 (2001).

[133] Schultz, H. J. *Phys. Rev. Lett.* **64**, 2831 (1990).

[134] Schultz, H. J. *Int. J. Mod. Phys. B* **5**, 57 (1991).

[135] Giamarchi, T. *Phys. Rev. B* **44**, 2905 (1991).

[136] Sólyom, J. *J. Low Temp. Phys.* **12**, 547 (1973).

[137] Menyhard, N. and Sólyom, J. *J. Low Temp. Phys.* **12**, 529 (1973).

[138] Sólyom, J. and Zawadowski, A. *J. Phys.* **4**, 80 (1974).

Bibliography

[139] Eggert, S. cond-mat/0708.0003, (2007).

[140] Sénéchal, D. cond-mat/9908262, (1999).

[141] Luther, A. and Emery, V. J. *Phys. Rev. Lett.* **33**, 589 (1974).

[142] Voit, J. *J. Phys. C: Solid State Phys.* **8**, 779 (1996).

[143] Emery, V. J., Luther, A., and Peschel, I. *Phys. Rev. B* **13**, 1272 (1976).

[144] Schulz, H. J. cond-mat/9412036, (1994).

[145] Ogata, M. and Shiba, H. *Phys. Rev. B* **41**, 2326 (1990).

[146] Pruschke, T. and Shiba, H. *Phys. Rev. B* **44**, 205 (1991).

[147] Ejima, S., Gebhard, F., and Nishimoto, S. *Europhys. Lett.* **70**, 492 (2005).

[148] Sandvik, A. W., Balents, L., and Campbell, D. K. *Phys. Rev. Lett.* **92**, 236401 (2004).

[149] Ejima, S. and Nishimoto, S. *Phys. Rev. Lett.* **99**, 216403 (2007).

[150] von Delft, J. and Schoeller, H. *Annalen Phys.* 7 **7**, 225 (1998).

[151] Rao, S. and Sen, D. cond-mat/0005492, (2000).

[152] Houghton, A., Kwon, H. J., and Marston, J. B. *Adv. Phys.* **49**, 141 (2000).

[153] Miranda, E. *Brazilian Journal of Physics* **33**, 3 (2003).

[154] Fabrizio, M. *Phys. Rev. B* **48**, 15838 (1993).

[155] Schultz, H. J. *Phys. Rev. B* **53**, 2959 (1996).

[156] Luther, A. *Phys. Rev. B* **19**, 320 (1979).

[157] Haldane, F. D. M. *Helv. phys. Acta* **65**, 152 (1994).

[158] Kopietz, P. and Schönhammer, K. *Z. Phys. B* **100**, 561 (1996).

[159] Kopietz, P., Hermisson, J., and Schönhammer, K. *Phys. Rev. B* **52**, 11877 (1995).

[160] Kopietz, P. *Bosonization of interacting fermions in arbitrary dimensions.* Springer-Verlag, (1997).

[161] Kolomeisky, E. B. and Straley, J. P. *Phys. Rev. Lett.* **74**, 4891 (1995).

[162] Abanov, A. G. In *Applications of Random Matrices in Physics.* Springer, (2006).

[163] Turing, A. M. *Philosophical transactions of the Royal Society of London Series B, Biological sciences* **B 237**, 37 (1952).

[164] Landau, L. D. *Sov. J. Phys. USSR* **5**, 71 (1941).

[165] Driscoll, T. A. and Trefethen, L. N. *Schwarz-Christoffel Mapping.* Cambridge University Press, (2002).

[166] Cartan, H. *Elementary Theory of Analytic Functions of One or Several Complex Variables.* Dover Publications, (1995).

[167] Belavin, A. A., Polyakov, A. M., and Zamolodchikov, A. B. *Nucl. Phys. B* **241**, 333 (1984).

[168] Affleck, I. *Acta Phys.Polon. B* **26**, 1869 (1995).

[169] Cardy, J. L. Les Houches'88 lectures, (1989).

[170] Ginsparg, P. hep-th/9108028, (1989).

[171] Saleur, H. cond-mat/9812110, (1998).

[172] Bernard, D. hep-ph/9509137, (1995).

[173] Efthimiou, C. J. and Spector, D. A. hep-th/0003190, (2000).

[174] Itzykson, C. and Drouffe, J. M. *Statistical field theory, vol. 2.* Cambridge University Press, (1989).

[175] Ryder, L. H. *Quantum Field Theory.* Cambridge University Press, (1985).

[176] Peskin, M. E. and Schroeder, D. V. *An Introduction to Quantum Field Theory.* HarperCollins Publishers, (1995).

[177] Itzykson, C. and Zuber, J.-B. *Quantum Field Theory.* Dover Publications, (2006).

[178] Cardy, J. *J. Phys. A: Math. Gen.* **17**, L385 (1984).

[179] Kac, M. *American Mathematical Monthly* **73**, 1 (1966).

[180] Casimir, H. B. G. *Koninkl. Ned. Akad. Wetenschap. Proc* **51**, 793 (1948).

[181] Bousso, R. *Rev. Mod. Phys.* **74**, 825 (2002).

Bibliography

[182] Holzhey, C., Larsen, F., and Wilczek, F. *Nucl. Phys. B* **424**, 443 (1994).

[183] Fiola, T. M., Preskill, J., Strominger, A., and Trivedi, S. P. *Phys. Rev. D* **50**, 3987 (1994).

[184] Srednicki, M. *Phys. Rev. Lett.* **71**, 666 (1993).

[185] Korepin, V. E. *Phys. Rev. Lett.* **92**, 096402 (2004).

[186] Calabrese, P. and Cardy, J. *J. Stat. Mech.: Theor. Exp.* **2004**, P06002 (2004).

[187] Casini, H. and Huerta, M. *J. Stat. Mech.: Theor. Exp.* **2005**, P12012 (2005).

[188] Tsallis, C. *J. Stat. Phys.* **52**, 479 (1988).

[189] Ryu, S. and Takayanagi, T. *Journal of High Energy Physics* **2006**, 045 (2006).

[190] Bonner, Jill C. and Fisher, M. E. *Phys. Rev.* **135**(3A), A640 (1964).

[191] Pang, T. *An introduction to computational physics.* Cambridge University Press, (1997).

[192] Thijssen, J. M. *Computational Physics.* Cambridge University Press, (1999).

[193] Dagotto, E. *Rev. Mod. Phys.* **66**, 763 (1994).

[194] Osborne, T. and Nielsen, M. *Quantum Information Processing* **1**, 45 (2002).

[195] Borrill, J. and Gleiser, M. *Nucl. Phys. B* **483**, 416 (1997).

[196] Srikanth, R. *Quant. Inf. Processing* **2**, 153 (2003).

[197] Ha, Z. N. C. *Quantum Many-Body Systems in One Dimension.* World Scientific, (1996).

[198] Karbach, M. and Muller, G. *Computers in Physics* **11**, 36 (1997). cond-mat/9809162.

[199] Karbach, M., Hu, K., and Muller, G. *Computers in Physics* **12**, 565 (1998). cond-mat/9809163.

[200] Karbach, M., Hu, K., and Muller, G. cond-mat/0008018, (2000).

[201] Xiang. *Phys. Rev. B* **53**, R10445 (1996).

144

[202] Nishimoto, S., Jeckelmann, E., Gebhard, F., and Noack, R. M. *Phys. Rev. B* **65**, 165114 (2002).

[203] Lin, H. Q. and Gubernatis, J. E. *Comput. Phys.* **7**, 400 (1993).

[204] Lanczos, C. *J. Res. Nat. Bur. Stand.* **45**, 255 (1950).

[205] Golub, G. H. and Loan, C. F. V. *Matrix Computations*. The Johns Hopkins University Press, (1996).

[206] Anderson, E., Bai, Z., Bischof, C., Blackford, S., Demmel, J., Dongarra, J., Croz, J. D., Greenbaum, A., Hammarling, S., McKenney, A., and Sorensen, D. *LAPACK Users' Guide*. SIAM, (1999).

[207] Press, W. H., Flannery, B. P., Teukolsky, S. A., and Vetterling, W. T. *Numerical Recipes in C++, The art of scientific Computing*. Cambridge University Press, (1999).

[208] Galassi, M., Davies, J., Theiler, J., Gough, B., Jungman, G., Booth, M., and Rossi, F. *GNU Scientific Library Reference Manual*. Network Theory Ltd, (2006).

[209] Paige, C. C. *J. Inst. Math. Appl.* **10**, 373 (1972).

[210] Paige, C. C. *J. Inst. Math. Appl.* **18**, 341 (1976).

[211] Paige, C. C. *Lin. Algebra. Appl.* **34**, 235 (1980).

[212] Cullum, J. K. and Willoughby, R. A. *Lanczos Algorithms for Large Symmetric Eigenvalue Computations*. Cambridge University Press, (1985).

[213] Jeckelmann, E. *Phys. Rev. B* **66**, 045114 (2002).

[214] Jaklic, J. and Prelovsek, P. *Adv. in Phys.* **49**, 1 (2000).

[215] Weisse, A., Wellein, G., Alvermann, A., and Fehske, H. *RMP* **78**, 275 (2006).

[216] Davidson, E. R. *J. Comp. Phys.* **17**, 87 (1975).

[217] Crouzeix, M. B., Philippe, B., and Sadkane, M. *SIAM J. Sci. Comput.* **15**, 62 (1994).

[218] Preskill, J. *Journal of Modern Optics* **47**, 127 (2000).

[219] Rajagopal, A. K. and Rendell, R. W. *Europhys. Lett.* **36**, 221 (2005).

[220] Bruß, D. *Journal of Mathematical Physics* **43**, 4237 (2002).

Bibliography

[221] Życzkowski, K. and Bengtsson, I. *Annals of Physics* **295**, 115 (2002).

[222] Collins, D. and Popescu, S. *Phys. Rev. A* **65**, 032321 (2002).

[223] Jordan, T. F. *Phys. Rev. A* **71**, 034101 (2005).

[224] Ghosh, S., Rosenbaum, T. F., Aeppli, G., and Coppersmith, S. N. *Nature* **425**, 48 (2003).

[225] Osterloh, A., Amico, L., Falci, G., and Fazio, R. *Nature* **416**, 608 (2002).

[226] Bennett, C. H., Bernstein, H. J., Popescu, S., and Schumacher, B. *Phys. Rev. A* **53**, 2046 (1996).

[227] Horodecki, M., Horodecki, P., and Horodecki, R. *Phys. Rev. Lett.* **80**, 5239 (1998).

[228] Vidal, G. and Werner, R. F. *Phys. Rev. A* **65**, 032314 (2002).

[229] Horodecki, M., Horodecki, P., and Horodecki, R. *Physics Lett. A* **223**, 1 (1996).

[230] Peres, A. *Phys. Rev. Lett.* **77**, 1413 (1996).

[231] Amico, L., Fazio, R., Osterloh, A., and Vedral, V. quant-ph/0703044, (2007).

[232] von Neumann, J. *The Mathematical Foundations of Quantum Mechanics.* Princeton University Press, (1932).

[233] Fano, U. *Rev. Mod. Phys.* **29**(1), 74 (1957).

[234] Landau, L. D. and Lifshitz, L. M. *Quantum Mechanics: Non-Relativistic Theory.* Pergamon Press, (1958).

[235] Feynman, R. P. *Statistical mechanics.* Addison-Wesley, (1972).

[236] Preskill, J. Lecture notes on quantum computation, (1998).

[237] Wehrl, A. *Rev. Mod. Phys.* **50**, 221 (1978).

[238] Shannon, C. E. *Bell System Technical Journal* **27**, 379 (1948).

[239] Shannon, C. E. *Bell System Technical Journal* **27**, 623 (1948).

[240] Huang, K. *Statistical mechanics.* Wiley, (1987).

[241] Morandi, G., Ercolessi, E., and Napoli, F. *Statistical mechanics.* World Scientific, (2001).

[242] Toda, M., Kubo, R., and Saito, N. *Statistical Physics I: Equilibrium Statistical Mechanics.* Springer, (2004).

[243] Vidal, J. *Phys. Rev. Lett.* **91**, 147902 (2003).

[244] Legeza, Ö. and Sólyom, J. *Phys. Rev. B* **70**, 205118 (2004).

[245] Eisert, J. and Cramer, M. *Phys. Rev. A* **72**, 042112 (2005).

[246] Peschel, I. and Zhao, J. *J. Stat. Mech.: Theor. Exp.* **11**, P11002 (2005).

[247] Vedral, V. *Rev. Mod. Phys.* **74**, 197 (2002).

[248] Lieb, E. H. *The Stability of Matter: From Atoms to Stars: Selecta of Elliot H. Lieb.* Springer, (2005).

[249] Ruelle, D. *Statistical Mechanics.* World Scientific, (1969).

[250] Araki, H. and Lieb, E. H. *Commun. Math. Phys.* **18**, 160 (1970).

[251] Fano, G., Ortolani, F., and Ziosi, L. *J. Chem. Phys.* **108**, 9246 (1998).

[252] White, S. R. and Martin, R. L. *J. Chem. Phys.* **110**, 4127 (1999).

[253] Bendazzoli, G. L., Evangelisti, S., Fano, G., Ortolani, F., and Ziosi, L. *J. Chem. Phys.* **110**, 1277 (1999).

[254] Daul, S., Chiofini, I., Daul, C., Daul, S. R., and White, S. R. *Int. J. Quantum Chem.* **79**, 331 (2000).

[255] Mitrushenkov, A. O., Fano, G., Ortolani, F., Linguerri, R., and Palmieri, P. *J. Chem. Phys.* **115**, 6815 (2001).

[256] Chan, G. K. and Head-Gordon, M. *J. Chem. Phys.* **116**, 4462 (2002).

[257] Mitrushenkov, A. O., Linguerri, R., Palmieri, P., and Fano, G. *J. Chem. Phys.* **119**, 4148 (2003).

[258] Legeza, Ö., Röder, J., and Hess, B. *Phys. Rev. B* **67**, 125114 (2003).

[259] Legeza, Ö., Röder, J., and Hess, B. *Mol. Phys.* **101**, 2019 (2003).

[260] Legeza, Ö. and Sólyom, J. *Phys. Rev. B* **68**, 195116 (2003).

Bibliography

[261] Rissler, J., Noack, R. M., and White, S. R. *J. Chem. Phys.* **323**, 519 (2006).

[262] Petz, D. *Linear Algebra and its Applications* **244**, 81 (1996).

[263] Ozawa, M. *Physics Letters A* **268**, 158 (2000).

[264] Verstraete, F., Dehaene, J., and De Moor, B. *Journal of Modern Optics* **49**, 1277 (2002).

[265] Bertlmann, R. A., Durstberger, K., Hiesmayr, B. C., and Krammer, P. *Phys. Rev. A* **72**, 052331 (2005).

[266] Holevo, A. S. *Probl. Inf. Transm. (USSR)* **177**, 9 (1973).

[267] Vidal, G., Latorre, J., Rico, E., and Kitaev, A. *Phys. Rev. Lett.* **90**, 227902 (2003).

[268] Latorre, J., Rico, E., and Vidal, G. *Quant. Inf. and Comp.* **4**, 48 (2004).

[269] Wilson, K. G. *Rev. Mod. Phys.* **47**(4), 773 Oct (1975).

[270] Krishna-murthy, H. R., Wilkins, J. W., and Wilson, K. G. *Phys. Rev. B* **21**, 1003 (1980).

[271] Costi, T. In *Density-Matrix Renormalization,* Peschel, I., Wang, X., Kaulke, M., and Hallberg, K., editors. Springer, (1990).

[272] Anderson, P. W. *Phys. Rev.* **124**(1), 41 Oct (1961).

[273] Anderson, P. W. *J. Phys. C: Solid State Phys.* **3**, 2436 (1970).

[274] Affleck, I. *Nucl. Phys. B* **336**, 517 (1990).

[275] Affleck, I. and Ludwig, A. W. W. *Phys. Rev. Lett.* **68**(7), 1046 Feb (1992).

[276] von Delft, J., Zaránd, G., and Fabrizio, M. *Phys. Rev. Lett.* **81**(1), 196 Jul (1998).

[277] Georges, A., Kotliar, G., Krauth, W., and Rozenberg, M. J. *Rev. Mod. Phys.* **68**(1), 13 Jan (1996).

[278] White, S. R. In *Density-Matrix Renormalization,* Peschel, I., Wang, X., Kaulke, M., and Hallberg, K., editors. Springer, (1990).

[279] White, S. R. and Noack, R. M. *Phys. Rev. Lett.* **68**(24), 3487 (1992).

[280] Golub, G. and Kahan, W. *SIAM, J. Numer. Anal. 2* , 205 (1965).

[281] Golub, G. and Reinsch, C. *Numer. Math.* **14**, 403 (1970).

[282] Latorre, J. I. quant-ph/0510031, (2005).

[283] Schmidt, E. *Math. Ann.* **63**, 433 (1907).

[284] Wang, X. and Zanardi, P. *Phys. Lett. A* **301**, 1 (2002).

[285] Peschel, I. *J. Phys. A: Math. Gen.* **36**, L205 (2003).

[286] Gu, S.-J., Tian, G.-S., and Lin, H.-Q. *Phys. Rev. A* **71**, 052322 (2005).

[287] Molina, R. A. and Schmitteckert, P. *Phys. Rev. B* **75**, 235104 (2007).

[288] Legeza, Ö. and Sólyom, J. *Phys. Rev. Lett.* **96**, 116401 (2006).

[289] Andersson, M., Boman, M., and Östlund, S. *Phys. Rev. B* **59**, 10493 (1999).

[290] Tsai, S.-W. and Marston, J. B. *Phys. Rev. B* **62**(9), 5546 (2000).

[291] Boschi, C. D. E. and Ortolani, F. *Eur. Phys. J. B* **41**, 503 (2004).

[292] Lepetit, M.-B. and Pastor, G. M. *Phys. Rev. B* **58**, 12691 (1998).

[293] Bursill, R. J. *Phys. Rev. B* **60**, 1643 (1999).

[294] Martín-Delgado, M. A. and Rodriguez-Laguna, J. and Sierra, G. *Phys. Rev. B* **65**, 155116 (2002).

[295] Carteret, H. A., Higuchi, A., and Sudbery, A. *J. Mat. Phys.* **41**, 7932–7939 (2000).

[296] White, S. R. *Phys. Rev. B* **72**, 180403 (2005).

[297] Lindblad, G. *Comm. Math. Phys.* **48**, 119 (1976).

[298] Östlund, S. and Rommer, S. *Phys. Rev. Lett.* **75**, 3537 (1995).

[299] Schumacher, B. *Phys. Rev. A* **51**, 2738 (1995).

[300] Jozsa, R. *J. Mod. Opt.* **41**, 2315 (1994).

[301] Fuchs, C. A. and Caves, C. M. *Phys. Rev. Lett.* **73**, 3047 (1994).

[302] Jaeger, G. *Quantum Information, An Overview.* Springer, (2007).

[303] Stroustrup, B. *The C++ Programming Language.* Addison-Wesley Professional, (2000).

Bibliography

[304] Noack, R. M. and White, S. R. In *Density-Matrix Renormalization,* Peschel, I., Wang, X., Kaulke, M., and Hallberg, K., editors. Springer, (1990).

[305] Cohen-Tannoudji, C., Diu, B., and Laloe, F. *Quantum Mechanics, vol 1 and 2.* Wiley-Interscience, (2006).

[306] Schollwöck, U. *Rev. Mod. Phys.* **77**, 259 (2005).

[307] Shibata, N. and Hotta, C. cond-mat/0503476, (2005).

[308] Hubbard, J. and Torrance, J. B. *Phys. Rev. Lett.* **47**, 1750 (1981).

[309] Ishihara, S., Egami, T., and Tachiki, M. *Phys. Rev. B* **49**, 8944 (1994).

[310] Nasu, K., Ping, H., and Mizouchi, H. *J. Phys. : Condens. Matter* **13**, R693 (2001).

[311] Horiuchi, S., Okimoto, Y., Kumai, R., and Tokura, Y. *Science* **299**, 229 (2003).

[312] Lieb, E. H. and Wu, F. Y. *Phys. Rev. Lett.* **20**, 1445 (1968).

[313] Ovchinnikov, A. A. *Sov. Phys. JETP* **30**, 1160 (1970).

[314] Nagaosa, N. and chi Takimoto, J. *J. Phys. Soc. Jpn.* **55**, 2735 (1986).

[315] MacDonald, A. H., Girvin, S. M., and Yoshioka, D. *Phys. Rev. B* **37**, 9753 (1988).

[316] Kampf, A., Sekania, M., Japaridze, G., and Brune, P. *J. Phys. : Condens. Matter* **15**, 5895 (2003).

[317] Kokashvili, P. and Japaridze, G. *J. Phys. C: Solid State Phys.* **16**, 5815 (2004).

[318] Haldane, F. D. M. *Phys. Rev. B* **25**, 4925 (1982).

[319] Manmana, S. R., Meden, V., Noack, R. M., and Schönhammer, K. *Phys. Rev. B* **70**, 155115 (2004).

[320] Torio, M. E., Aligia, A. A., and Ceccatto, H. A. *Phys. Rev. B* **64**, 121105 (2001).

[321] Fabrizio, M., Gogolin, A. O., and Nersesyan, A. A. *Phys. Rev. Lett.* **83**, 2014 (1999).

[322] Fabrizio, M., Gogolin, A. O., and Nersesyan, A. A. *Nucl. Phys. B* **580**, 647 (2000).

[323] Delfino, G. and Mussardo, G. *Nucl. Phys. B* **516**, 674 (1998).

[324] Legeza, Ö., Buchta, K., and Sólyom, J. *Phys. Rev. B* **73**(16), 165124 (2006).

[325] Gidopoulos, N., Sorella, S., and Tosatti, E. *Eur. Phys. J. B* **14**, 217 (2000).

[326] Wilkens, T. and Martin, R. M. *Phys. Rev. B* **63**, 235108 (2001).

[327] Lou, J., Qin, S., Xiang, T., Chen, C., Tian, G.-S., and Su, Z. *Phys. Rev. B* **68**, 045110 (2003).

[328] Otsuka, H. and Nakamura, M. *Phys. Rev. B* **71**, 155105 (2005).

[329] Aligia, A. A. and Batista, C. D. *Phys. Rev. B* **71**, 125110 (2005).

[330] Ovchinnikov, S. G. and Val'kov, V. V. *Hubbard Operators in the Theory of Strongly Correlated Electrons*. Imperial College Press, (2004).

[331] Haley, S. B. and Erdös, P. *Phys. Rev. B* **5**, 1106 (1972).

[332] Legeza, Ö. and Fáth, G. *Phys. Rev. B* **53**, 14349 (1996).

[333] Roomany, H. H. and Wyld, H. W. *Phys. Rev. D* **21**, 3341 (1980).

[334] Hamer, C. J. and Barber, M. N. *J. Phys. A: Math. Gen.* **14**, 241 (1981).

[335] Hamer, C. J. *J. Phys. A: Math. Gen.* **16**, 3085 (1983).

[336] Zhu, L., Garst, M., Rosch, A., and Si, Q. *Phys. Rev. Lett.* **91**, 066404 (2003).

[337] Hellman, H. *Einfuhrung in die Quantenchemie*. Detiche, (1937).

[338] Feynman, R. P. *Phys. Rev.* **56**, 340 (1939).

[339] Slater, J. C. *Solid-state and molecular theory: a scientific biography*. John Wiley and Sons, (1975).

[340] Cardy, J. *Phys. Rev. B* **26**, 6311 (1982).

[341] Horovitz, B. and Sólyom, J. *Phys. Rev. B* **35**, 7081 (1987).

[342] Batista, C. D. and Aligia, A. A. *Phys. Rev. Lett.* **92**, 246405 (2004).

[343] Mott, N. F. *Metal-Insulator Transitions*. CRC, (1990).

Bibliography

[344] Imada, M., Fujimori, A., and Tokura, Y. *Rev. Mod. Phys.* **70**, 1039 (1998).

[345] Dzierzawa, M., Baeriswyl, D., and Martelo, L. M. *Helv. Phys. Acta* **70**, 124 (1997).

[346] Fabrizio, M. *Phys. Rev. B* **54**, 10054 (1996).

[347] Kuroki, K., Arita, R., and Aoki, H. *J. Phys. Soc. Japan* **66**, 3371 (1997).

[348] Arita, R., Kuroki, K., Aoki, H., and Fabrizio, M. *Phys. Rev. B* **57**, 10324 (1998).

[349] Daul, S. and Noack, R. M. *Phys. Rev. B* **58**, 2635 (1998).

[350] Daul, S. and Noack, R. M. *Phys. Rev. B* **61**, 1646 (2000).

[351] Torio, M. E., Aligia, A. A., and Ceccatto, H. A. *Phys. Rev. B* **67**, 165102 (2003).

[352] Aebischer, C., Baeriswyl, D., and Noack, R. M. *Phys. Rev. Lett.* **86**, 468 (2001).

[353] Louis, K., Alvarez, J. V., and Gros, C. *Phys. Rev. B* **64**, 113106 (2001).

[354] Louis, K., Alvarez, J. V., and Gros, C. *Phys. Rev. B* **65**, E249903 (2002).

[355] Hamacher, K., Gros, C., and Wenzel, W. *Phys. Rev. Lett.* **88**, 217203 (2002).

[356] Gros, C., Hamacher, K., and Wenzel, W. *Europhys. Lett.* **69**, 616 (2005).

[357] Capello, M., Becca, F., Fabrizio, M., Sorella, S., and Tosatti, E. *Phys. Rev. Lett.* **94**, 026406 (2005).

[358] Japaridze, G. I. and Nersesyan, A. A. *JETP Lett.* **27**, 334 (1978).

[359] Japaridze, G. I. and Nersesyan, A. A. *J. Low Temp. Phys.* **37**, 95 (1979).

[360] Pokrovsky, V. L. and Talapov, A. L. *Phys. Rev. Lett.* **42**, 65 (1979).

[361] Schulz, H. J. *Phys. Rev. B* **22**, 5274 (1980).

[362] Lin, H. Q. and Hirsch, J. E. *Phys. Rev. B* **35**, 3359 (1987).

[363] Haldane, F. D. M. *Phys. Rev. B* **26**, 5257 (1982).

[364] Okamoto, K. and Nomura, K. *Phys. Lett. A* **169**, 422 (1992).

[365] Eggert, S. *Phys. Rev. B* **54**, R9612 (1996).

[366] White, S. R. and Affleck, I. *Phys. Rev. B* **54**, 9862 (1996).

[367] Balents, L. and Fisher, M. P. A. *Phys. Rev. B* **53**, 12133 (1996).

[368] Japaridze, G. I., Nersesyan, A. A., and Wiegmann, P. B. *Nucl. Phys. B* **230**, 511 (1984).

[369] Aebischer, C. *Dielectric catastrophe at the Mott Transition.* PhD thesis, University of Fribourg, (2002).

[370] Fabrizio, M. and Gogolin, A. *Phys. Rev. B* **51**, 17827 (1995).

[371] Bedürftig, G., Brendel, B., Frahm, H., and Noack, R. *Phys. Rev. B* **58**, 10225 (1998).

[372] Sorensen, E., Affleck, I., Augier, D., and Poilblanc, D. *Phys. Rev. B* **58**, R14701 (1998).

[373] Wu, L.-A., Sarandy, M., and Lidar, D. *Phys. Rev. Lett.* **93**, 250404 (2004).

[374] Osborne, T. and Nielsen, M. *Phys. Rev. A* **66**, 32110 (2002).

[375] Syljuåsen, O. *Phys. Rev. A* **68**, R60301 (2003).

[376] Gu, S., Lin, H., and Li, Y. *Phys. Rev. A* **68**, 42330 (2003).

[377] Vidal, J., Palacios, G., and Mosseri, R. *Phys. Rev. A* **69**, 022107 (2004).

[378] Vidal, J., Mosseri, R., , and Dukelsky, J. *Phys. Rev. A* **69**, 054101 (2004).

[379] Roscilde, T., Verrucchi, P., Fubini, A., Haas, S., and Tognetti, V. *Phys. Rev. Lett.* **93**, 167203 (2004).

[380] Roscilde, T., Verrucchi, P., Fubini, A., Haas, S., and Tognetti, V. *Phys. Rev. Lett.* **94**, 147208 (2005).

[381] Yang, M.-F. *Phys. Rev. A* **71**, R30302 (2005).

[382] Zanardi, P. *Phys. Rev. A* **65**, 42101 (2002).

[383] Gu, S., Deng, S., Li, Y., and Lin, H. *Phys. Rev. Lett.* **93**, 86402 (2004).

[384] Larsson, D. and Johannesson, H. *Phys. Rev. Lett.* **95**, 196406 (2005).

[385] Larsson, D. and Johannesson, H. *Phys. Rev. A* **73**, 042320 (2006).

[386] Deng, S.-S., Gu, S.-J., and Lin, H.-Q. *Phys. Rev. B* **74**, 045103 (2006).

[387] Affleck, I. and Ludwig, A. W. W. *Phys. Rev. Lett.* **67**, 161 (1991).

[388] Laflorencie, N., Sørensen, E. S., Chang, M.-S., and Affleck, I. *Phys. Rev. Lett.* **96**, 100603 (2006).

[389] Sólyom, I. *Fundamentals of the physics of solids, vol. 1.* Springer, (2007).

[390] Namura, K. and Okamoto, K. *J. Phys. A: Math. Gen.* **27**, 5773 (1994).

[391] Allen, D. and Sénéchal, D. *Phys. Rev. B* **55**, 299 (1997).

[392] Chitra, R. and Giamarchi, T. *Phys. Rev. B* **55**, 5816 (1997).

[393] Nersesyan, A. A., Gogolin, A. O., and Essler, F. H. L. *Phys. Rev. Lett.* **81**, 910 (1998).

[394] Bursill, R., Gehring, G. A., Farnell, D. J. J., Parkinson, J. B., Xiang, T., and Zeng, C. *J. Phys. C: Solid State Phys.* **7**, 8605 (1995).

[395] Chitra, R., Pati, S., Krishnamurthy, H. R., Sen, D., and Ramasesha, R. *Phys. Rev. B* **52**, 6581 (1995).

[396] Aligia, A. A., Batista, C. D., and Essler, F. H. *Phys. Rev. B* **62**, 3259 (2000).

[397] Bader, H. P. and Schilling, R. *Phys. Rev. B* **19**, 3556 (1979).

[398] Lu, H. T., Wang, Y. J., Qin, S., and Xiang, T. *Phys. Rev. B* **74**, 134425 (2006).

[399] Haldane, F. D. M. *Phys. Rev. Lett.* **50**, 1153 (1983).

[400] Haldane, F. D. M. *Phys. Lett. A* **93**, 464 (1983).

[401] Dell'Aringa, S., Ercolessi, E., Morandi, G., Pieri, P., and Roncaglia, M. *Phys. Rev. Lett.* **78**, 2457 (1997).

[402] Castilla, G., Chakravarty, S., and Emery, V. J. *Phys. Rev. Lett.* **75**, 1823 (1995).

[403] Knizhnik, V. G. and Zamolodchikov, A. B. *Nucl. Phys. B* **247**, 83 (1984).

[404] Majumdar, C. K. and Ghosh, D. K. *J. Mat. Phys.* **10**, 1388 (1969).

[405] Majumdar, C. K. and Ghosh, D. K. *J. Mat. Phys.* **10**, 1399 (1969).

[406] Lieb, E., Schultz, T. D., and Mattis, D. C. *Ann. Phys.* **16**, 407 (1961).

[407] Kolb, M. *Phys. Rev. B* **31**, 7494 (1985).

[408] Affleck, I. and Lieb, E. H. *Lett. Math. Phys.* **12**, 57 (1986).

[409] Yamanaka, M., Oshikawa, M., and Affleck, I. *Phys. Rev. Lett.* **79**, 1110 (1997).

[410] Hastings, M. B. *Phys. Rev. B* **69**, 104431 (2004).

[411] Legeza, Ö. Private communication, (2006).

[412] Shastry, B. S. and Sutherland, B. *Physics B* **108**, 1069 (1981).

[413] Gelfand, M. P. *Phys. Rev. B* **43**, 8644 (1991).

[414] Legeza, Ö., Fáth, G., and Sólyom, J. *Phys. Rev. B* **55**, 291 (1997).

[415] Kolezhuk, A. K. and Mikeska, H. *Phys. Rev. B* **56**, 11380 (1997).

[416] Millet, P., Mila, F., Zhang, F. C., Mambrini, M., Van Oosten, A. B., Pashchenko, V. A., Sulpice, A., and Stepanov, A. *Phys. Rev. Lett.* **83**, 4176 (1999).

[417] Affleck, I., Kennedy, T., Lieb, E., and Tasaki, H. *Phys. Rev. Lett.* **59**, 799 (1987).

[418] Arovas, D. P., Auerbach, A., and Haldane, F. D. M. *Phys. Rev. Lett.* **60**, 531 (1988).

[419] Batista, C. D. and Ortiz, G. and Gubernatis, J. E. *Phys. Rev. B* **65**, 180402 (2002).

[420] Uimin, G. V. *Sov. Phys. JETP* **12**, 225 (1970).

[421] Lai, C. K. *J. Mat. Phys.* **15**, 1675 (1974).

[422] Sutherland, B. *Phys. Rev. B* **12**, 3795 (1975).

[423] Itoi, C. and Kato, M.-H. *Phys. Rev. B* **55**, 8295 (1997).

[424] Fáth, G. and Sólyom, J. *Phys. Rev. B* **47**, 872 (1993).

[425] Takhtajan, L. A. *Phys. Lett. A* **87**, 479 (1982).

[426] Babujian, H. M. *Phys. Lett. A* **90**, 479 (1982).

Bibliography

[427] Affleck, I. *Nucl. Phys. B* **265**, 4090 (1986).

[428] Affleck, I. and Haldane, F. D. M. *Phys. Rev. B* **36**, 5291 (1987).

[429] Blöte, H. W. J. and Capel, H. W. *Physica A* **139**, 387 (1986).

[430] Oitmaa, J., Parkinson, J. B., and Bonner, J. C. *J. Phys. C: Solid State Phys.* **19**, L595 (1986).

[431] Sólyom, J. *Phys. Rev. B* **36**, 8642 (1987).

[432] Singh, R. R. P. and Gelfand, M. P. *Phys. Rev. Lett.* **61**, 2133 (1988).

[433] Chang, K., Affleck, I., Hayden, G. W., and Soos, Z. G. *J. Phys. C: Solid State Phys.* **1**, 153 (1989).

[434] Parkinson, J. C. *J. Phys. C* **21**, 3793 (1988).

[435] Klümper, A. *Europhys. Lett.* **9**, 815 (1989).

[436] Klümper, A. *J. Phys. A: Math. Gen.* **23**, 809 (1990).

[437] Klümper, A. *Int. J. Mod. Phys. B* **4**, 871 (1990).

[438] Barber, M. N. and Batchelor, M. T. *Phys. Rev. B* **40**, 4621 (1989).

[439] Chubukov, A. V. *J. Phys. C: Solid State Phys.* **2**, 1593 (1990).

[440] Chubukov, A. V. *Phys. Rev. B* **43**, 3337 (1991).

[441] Fáth, G. and Sólyom, J. *Phys. Rev. B* **51**, 3620 (1995).

[442] Schadschneider, A. and Zittartz, J. *Annalen der Physik* **4**, 157 (1995).

[443] Katsumata, K. *J. Magn. Magn. Mater.* **140-144**, 1595 (1995).

[444] Buchta, K., Fáth, G., Legeza, Ö., and Sólyom, J. *Phys. Rev. B* **72**, 054433 (2005).

[445] Läuchli, A., Schmid, G., and Trebst, S. *Phys. Rev. B* **74**, 14426 (2006).

[446] Buchta, K., Szirmai, E., Legeza, Ö., and Sólyom, J. *Phys. Rev. B* **75**, 155108 (2007).

[447] Fáth, G. and Sólyom, J. *Phys. Rev. B* **44**, 11836 (1991).

[448] Schollwöck, U., Jolicoeur, T., and Garel, T. *Phys. Rev. B* **53**, 3304 (1996).

[449] Fan, H., Korepin, V., and Roychowdhury, V. *Phys. Rev. Lett.* **93**, 227203 (2004).

[450] Lin, H. Q. *Phys. Rev. B* **42**, 6561 (1990).

[451] White, S. R. and Huse, D. A. *Phys. Rev. B* **48**, 3844 (1993).

[452] Golinelli, O., Jolicœur, T., and Lacaze, R. *Phys. Rev. B* **50**, 3037 (1999).

[453] Japaridze, G., Noack, R., and Baeriswyl, D. cond-mat/0607054, (2006).

[454] Verstraete, F. and Cirac, J. I. cond-mat/0407066, (2004).

[455] Verstraete, F., Porras, D., and Cirac, J. I. *Phys. Rev. Lett.* **93**, 227205 (2004).

[456] Verstraete, F. and Cirac, J. I. *Phys. Rev. A* **70**, 060302 (2004).

[457] Pérez-García, D., Verstraete, F., Wolf, M. M., and Cirac, J. I. *Quantum Inf. Comput.* **7**, 401 (2006).

[458] Vidal, G. quant-ph/0610099, (2006).

[459] Vidal, G. *Phys. Rev. Lett.* **99**, 220405 (2007).

[460] Verstraete, F., García-Ripoll, J. J., and Cirac, J. I. *Phys. Rev. Lett.* **93**, 207204 (2004).

[461] García-Ripoll, J. J. *New Journal of Physics* **8**, 305 (2006).

Curriculum Vitae

Name	Leonildo Tincani
Citizenship	Italian
Date of Birth	October 12, 1976
Place of birth	Scandiano (RE), Italy

Studies

04/2007 - 05/2007	Visiting scientist at the KFKI of Budapest, Hungary Collaboration with Dr. Ö. Legeza and Prof. J. Sólyom
04/2006 - 07/2006	Visiting scientist at the KFKI of Budapest, Hungary Collaboration with Dr. Ö. Legeza and Prof. J. Sólyom
10/2004 - 04/2008	Ph.D. candidate and International Research Training Group fellow at the University of Marburg, Germany Supervisor: Prof. Dr. R. M. Noack
07/2004	Visiting scientist at *AG Vielteilchennumerik* group of the University of Marburg, Germany
09/2002 - 03/2004	Doctorant en physique at the University of Fribourg, Switzerland Supervisor: Prof. D. Baeriswyl
06/2002	Visiting scientist at the University of Fribourg, Switzerland
10/2001	Degree in Theoretical Physics with full marks: 110/110 *magna cum laude* Thesis: "Competition of order parameters in HTSC" Supervisors: Prof. Dr. P. Pieri and Dr. E. Ercolessi
1997-2000	Undergraduate student with fellowship, *Corso di laurea in Fisica* at the University of Bologna, Italy
1995-1997	Undergraduate student with fellowship, *Corso di laurea in Astronomia* at the University of Bologna, Italy
1995	High School Diploma degree in Nuclear Physics with marks 58/60, Modena, Italy
1990-1995	High School student at the I.T.I.S. of Modena, Italy